

Tesi di dottorato in Ingegneria Biomedica, di Tommaso Novellino,
discussa presso l'Università Campus Bio-Medico di Roma in data 10/03/2011.
La disseminazione e la riproduzione di questo documento sono consentite per scopi di didattica e ricerca,
a condizione che ne venga citata la fonte.



Università Campus Bio-Medico di Roma
Corso di dottorato di ricerca in
.....Ingegneria Biomedica.....
XXII ciclo anno 2007

Nanoengineering tools for biomedical applications: sustained drug-delivery and vascular biophysics

Tommaso Novellino

Coordinatoro Tutore
Prof. Giulio Iannello..... Prof. Saverio Cristina.....

Co-Tutore
Prof. Mauro Ferrari.....

10 Marzo 2011

James Cook

Table of Contents

1 Abstract.....	4
2 Nanochannel system for controlled drug release.....	7
2.1 Diffusion and nanochanneled devices	8
2.1.1 Diffusion: fickian versus linear	9
2.1.2 Nano-channeled devices: structure and experimental-set-up.....	12
2.1.3 Experimental methods common to Sections 2.2 and 2.3	15
2.1.4 Personal contribution	35
2.2 Release of drug from nanochanneled devices implanted in rats	36
2.2.1 Interferon	37
2.2.2 Experimental methods.....	40
2.2.2.1 <i>In lab</i> study	40
2.2.2.2 <i>In vivo</i> study	43
2.2.3 Main results and discussion.....	48
2.2.3.1 <i>In lab</i> study	48
2.2.3.2 <i>In vivo</i> study	54
2.2.4 Conclusions.....	64
2.2.5 Acknowledgements of Section 2.2	65
2.3 Release of probe from nanochanneled devices in laboratory condition.....	66
2.3.1 Experimental methods.....	67
2.3.2 Main results and discussion.....	70
2.3.3 Personal contribution	75
2.4 Acknowledgements	76
3 The endothelial barrier and cell cytoskeleton.....	77
3.1 Rationale of the study	77
3.2 Endothelial cells and cell cytoskeleton.....	79
3.2.1 Endothelial structure and functions	79
3.2.2 Cytoskeleton structure and functions	81
3.3 Atomic force microscopy and colloidal probe.....	84


2

3.3.1 Near-field and far-field microscopy	85
3.3.2 Scanning-tunnel and Atomic-force microscopy	89
3.3.3 AFM functioning, imaging topography and force measurement	92
3.3.3.1 AFM components.....	94
3.3.3.2 AFM measurement.....	99
3.3.3.3 AFM modalities	103
3.3.4 AFM applications.....	106
3.4 Influence of pro-inflammatory cytokine on cytoskeleton organization	109
3.4.1 Inflammation and surface adhesion molecules	110
3.4.2 Experimental methods.....	113
3.4.3 Main results and discussion.....	120
3.4.4 Conclusions.....	136
3.4.5 Acknowledgements of Section 3.4	138
3.5 Influence of internalized nanoparticles on cytoskeleton organization	139
3.5.1 Gold nanoparticles	139
3.5.2 Experimental methods.....	143
3.5.3 Main results and discussion.....	145
3.5.4 Conclusions.....	164
3.5.5 Acknowledgements of Section 3.5	165
4 Conclusions	166
5 References	168
6 Acknowledgements	192

Nanoengineering tools for biomedical applications: sustained drug-delivery and vascular biophysics

1 Abstract

Nanotechnology is a rapidly-expanding field dealing with the control, manipulation and understanding of matter at scale ranging approximately between 1 and 1000 nanometers [Ferrari 2005]. Nanomaterial is any object with a characteristic size falling within the above range, either naturally-occurring or man-made, presenting features that are uniquely related to its size. Nanotechnology has led to the development of a wide ensemble of structures and devices with relevant applications in a variety of fields including automotive, robotics, manufacturing, electronics, communication and medicine [Watson 2004, Lu *et al* 2007, Uskokovic 2007].

Nanomedicine represents the branch of nanotechnology with immediate application to the biomedical sciences and healthcare system [Kim *et al* 2010, Sahoo *et al* 2007, Jain 2010]. It permits to finely tune the interaction between a man-created device and a biological system, for applications such as imaging, drug delivery and thermal ablation. Particularly interesting are the *nanochannel systems* and *engineered nanoparticles*, because of their versatility and tunability. The nanochannel systems are micro-fabricated molecular sieves bearing nano-sized channels with adjustable geometry and can be used for drug delivery and discovery, clinical diagnostics, biomolecules separation and analysis, cell immunoisolation and analysis [Adiga *et al* 2009, Huh *et al* 2007]. The engineered nanoparticles are nano-sized particles with adjustable composing material, particle shape and size and surface conjugation and can be used for therapeutic, diagnostic and imaging purposes [Service 2010, Fadeel *et al* 2010].

This thesis presents two engineering tools falling in the realm of nanomedicine. The first tool is a nanochannel membrane for the long-term controlled release of drug molecules; the

second tool is the atomic force microscopy here used for mechano-biological cell characterization.

During the first year of my visiting scholarship in the Texas Medical Center, working in the laboratory of Dr. Mauro Ferrari, my research activity has focused on the *in-vivo* and *in-lab* analysis of drug and small molecules release through a nanochanneled system. After that, in the last one year of activity, I turned my attention to the mechano-biological characterization of endothelial cells exposed to different external stimuli, such as pro-inflammatory cytokines and gold nanoparticles. In this case, the cell properties have been assessed using several techniques, including conventional epifluorescent, confocal, darkfield and atomic force microscopy.

In the first project, the release of different molecules –drugs (interferon alpha, IFN- α) and a molecular probe (dextran)– was measured through a nano-channeled delivery system (nDS), obtained by photolithographic microfabrication. The IFN- α diffusion was studied both *in-vivo* (healthy rats) as well as *in-lab* (diffusion devices) condition; the IFN concentration was measured, in blood and in proper solvent respectively, by ELISA immunoassay. The *in-vivo* studies have shown a linear and sustained release, which would be of interest from the clinical point of view. The release of a fluorescent dextran, evaluated only *in-lab* condition and measured by spectrophotometer, demonstrated a constant release for about 60 days, thus confirming literature already demonstrating such diffusive behavior for similar nDS membranes with other molecules under certain conditions. This activity has led to a manuscript on the IFN diffusion that will be shortly submitted [De Rosa *et al* 2011].

In the second project, the mechano-biological response of endothelial cells to external stimuli was evaluated. Two different stimuli were considered: a well-established pro-inflammatory cytokine (TNF- α); and two differently-sized spherical gold nano-particles (30 and 100 nm diameters). Upon stimulation, the mechanical properties such as cell stiffness and adhesion, cytoskeletal organization; and biological properties, such as cell inflammation and viability were assessed by atomic force microscopy (AFM), confocal microscopy, epifluorescent microscopy, darkfield microscopy, ELISA immunoassay, viability and proliferation testing. In particular, an AFM bearing a colloidal micrometric particle (colloidal probe) was used, which permits to probe the biomechanics of the cells with high sensitivity and specificity. Both external stimuli were shown to significantly affect cell response in terms of cell stiffness, adhesion and cytoskeletal organization. Stimulation with TNF- α led to cell stiffening, overall adhesion decreasing and actin cytoskeleton thickening; whereas

A handwritten signature in black ink, appearing to read "Tommaso Novellino".

Tesi di dottorato in Ingegneria Biomedica, di Tommaso Novellino,
discussa presso l'Università Campus Bio-Medico di Roma in data 10/03/2011.
La disseminazione e la riproduzione di questo documento sono consentite per scopi di didattica e ricerca,
a condizione che ne venga citata la fonte.

stimulation with gold nanoparticles led to an overall decrease in cell stiffness and increase in non-functional actin filaments formation. These findings would suggest a bio-active role for these nano-particles when internalized by endothelial cells in sufficient amount. This activity has led to two manuscripts: one, already published, focusing on the TNF- α stimulation [Lee *et al* 2011]; and one, in preparation, focusing on the gold nanoparticles stimulation [Novellino *et al* 201x].



A handwritten signature in black ink, appearing to read "Tommaso Novellino".

2 Nanochannel system for controlled drug release

Classical diffusion theory establishes that the movement of solute molecules in a non-homogeneous solution can be predicted, from a macroscopic point of view, by Fick's laws. The basic principle is that the flux vector is proportional to the concentration gradient. Fick's laws have been successfully applied to predict the diffusion kinetics of molecules through thin semi-permeable membranes.

Nevertheless, experiments have shown that, as the size of the membrane pores approaches the molecular hydrodynamic radius, unexpected effects, which cause substantial deviations from kinetics predicted by Fick's laws, can occur, as shown in [Martin *et al* 2005] for the case of silicon nano-porous membranes. In the latter, the membrane is made up of silicon and fabricated by photolithographic techniques; its pores are rectangular and nanometric in only one dimension (the other dimensions are in the μm range). The observable macroscopic effect consists of a prolonged linear release of several molecules (human recombinant interferon- α -2b, bovine serum albumin), which eventually switches to an exponential Fick's profile.

Tommaso Novellino,
7

2.1 Diffusion and nanochanneled devices

The molecular-diffusion dynamics in unconstrained cases has been studied thoroughly during the last two centuries, leading to the well-known Fick's diffusion laws and Stokes-Einstein equation.

More recently, a new impulse to the study of this topic has been provided by the necessity of understanding the behavior of solute particles in the presence of environmental constraints of size comparable to the molecular dimensions; for e.g., diffusion kinetics of biomolecules –such as bovine serum albumin, interferon, lysozyme– through micro-fabricated silicon membranes, having pores of nanometric size ($\approx 1\text{--}10 \text{ nm}$) in only one dimension (the other dimensions being in the μm range) have been experimentally studied and mathematically modeled [Cosentino *et al* 2005]. Their experimental results showed that the diffusion profiles, in some cases, deviated substantially from those predicted by Fick's laws; they proposed a new diffusion mathematical model, to reasonably explain that phenomenon and –at the same time–recover the classical diffusion laws in the unconstrained case.



A handwritten signature in black ink, appearing to read "Tommaso Novellino".

2.1.1 Diffusion: fickian versus linear

When there is a chemical-potential gradient in a single-phase fluid mixture, which implies that a concentration gradient is present in the fluid mixture, each chemical species will diffuse in the direction of decreasing concentration.

The mathematical formula which describes this phenomenon is known as *Fick's law*. Given a solute A in a solvent B , it represents a linear relationship between the mass (or molar) flux (with respect to the mass average velocity) of A in B , J_{AB} , and the gradient of the concentration of A in B , ∇c_{AB} [Saatdjian 2000]. For a binary mixture, Fick's first law is:

$$J_{AB} = -D_{AB}\nabla c_{AB} \quad (\text{Equation 2.1.1})$$

where D_{AB} is the diffusion coefficient of A in B ; the Einstein's relation expresses the D_{AB} of spherical Brownian particles A in solution as

$$D_{AB} = \frac{kT}{6\pi r\eta} \quad (\text{Equation 2.1.2})$$

where k is the Boltzmann constant, T is the temperature, r is the radius of the particles constituting A , η is the viscosity coefficient of B .

Free (un-constrained) diffusion

The classical theory applied to a reservoir–sink diffusion system as in [Cosentino *et al* 2005], neglecting the effect of the above-mentioned diffusion membrane, is subsequently described.

The considered system is composed of two diffusing chambers, a reservoir (where the solute is initially totally-concentrated) and a sink (which is initially constituted only by pure solvent without solute). A binary-mixture, consisting of a solvent –e.g. phosphate buffer saline (PBS)– and a certain solute, is placed in the diffusing system. The following hypotheses are assumed to hold:



Tommaso Novellino
9

- a) The experimental volume, V_T , containing a total mass of drug A , can be divided in two compartments of volume V_1 (the reservoir) and V_2 (the sink), with the respective initial mass concentrations $c_{A1}^0 = c_{A1}(0)$ and $c_{A2}^0 = c_{A2}(0)$, with $c_{A1}^0 > c_{A2}^0$;
- b) The concentration is homogeneous in each compartment, and the concentration variation is spatially defined in a thin boundary region of depth L ;
- c) Given a Cartesian reference-system (x, y, z) , the concentration gradient, ∇c_A , has null components along the y and z axes.

In order to calculate the mass flux of drug through a generic surface, of area S , assumed to be perpendicular to the diffusion path, **Equation 2.1.1** plus the hypotheses (b) and (c) can approximate the flux as

$$J_A(t) = D_{AB} \frac{c_{A1}(t) - c_{A2}(t)}{L} \quad (\text{Equation 2.1.3})$$

Elaborating **Equation 2.1.3** together with the mass-conservation principle yields to [Cosentino *et al* 2005]:

$$J_A(t) = (c_{A1}^0 - c_{A2}^0) \frac{D_{AB}}{L} e^{-\lambda_A t} \quad \text{where } \lambda_A = (D_{AB}S/V_1L)[1 + (V_1/V_2)] \quad (\text{Equation 2.1.4})$$

Therefore, in the free (fickian) diffusion case, the release profile is exponential.

In the next section, the mathematical description of the membrane effect will be introduced, in order to compare this case with the free-diffusion case.

Diffusion through nanochannels: constrained diffusion

The constrained diffusion model has been derived [Cosentino *et al* 2005] starting from the experimental results provided in [Martin *et al* 2005], which showed that the release-profile remained linear for a certain period and then it switched to the Fickian exponential trend: they hypothesized that the effect of the membrane can be modeled by means of a *saturation effect* on the mass flux. Indicating with \hat{J}_A , the mass flux now can be written as [Cosentino *et al* 2005]:

$$J_A(t) = \text{sat} \left[\frac{D_{AB}}{L} (c_{A1}(t) - c_{A2}(t)) \right]_{-\hat{J}_A}^{\hat{J}_A} \quad \text{where} \quad \text{sat}[x]_a^b = \begin{cases} b & \text{if } x > b \\ x & \text{if } x \in [a, b] \\ a & \text{if } x < a \end{cases} \quad (\text{Equation 2.1.5})$$

is the saturation function.

The hypothesis expressed in **Equation 2.1.5** intuitively comes from thinking of each nanochannel as a bottleneck: over a certain concentration level, the molecular flux through the channel will remain the

same regardless of the number of particles per unit volume in the reservoir compartment.

Moreover, this description coincides with the classical diffusion laws if the threshold-value is very large (which means unconstrained diffusion).

The experimentally-observed switch between the linear and exponential diffusion [Martin *et al* 2005] can be explained by the fact that, over time, the concentration decreases in the reservoir, eventually yielding the concentration gradient (and therefore the flux) to return below the threshold value.

2.1.2 Nano-channeled devices: structure and experimental-set-up

Devices micro-fabrication

Photolithographic silicon-fabrication techniques allow the production of large numbers of precisely designed devices with high reproducibility.

Microfabricated devices are widely used for energy production [Mitrovski *et al* 2006] as well as in medical applications [Chin *et al* 2007]. Lab-on-a-chip, micro- and nano-fluidic devices [Whitesides 2006], nanochannel membranes and filters can potentially be applied in clinical diagnostics [Srinivasan *et al* 2004], DNA and protein separation and analysis [Fu *et al* 2007], cell immuno-isolation [Desai *et al* 2000], drug delivery [LaVan *et al* 2003], drug discovery [Dittrich *et al* 2005], immuno-assays and cell analysis [Sato *et al* 2003]. All these applications take advantage of processing small volumes of fluids in accurate and specifically-tailored small structures [Beebe *et al* 2002].

Particularly, cell immuno-isolation, high-selectivity filtering, drug-delivery from implantable devices require superior precision of the device structure. More specifically, the micro- and nano-channel size in drug-delivery devices (*membranes*), as those in [Lesinski *et al* 2005] and those shown later in **Figure 2.1.1**, determines the drug release from the implanted reservoir [Amato *et al* 2006, Prich *et al* 2006, Stone *et al* 2004]; since any accidental structural defect may translate into ineffective medical treatment or adverse overdosing effects, the large-scale production of these devices requires rapid and agile selection methods, as the one presented in [Grattoni *et al* 2009], in order to assure the superior quality of the final products and their conformity to specific standards.

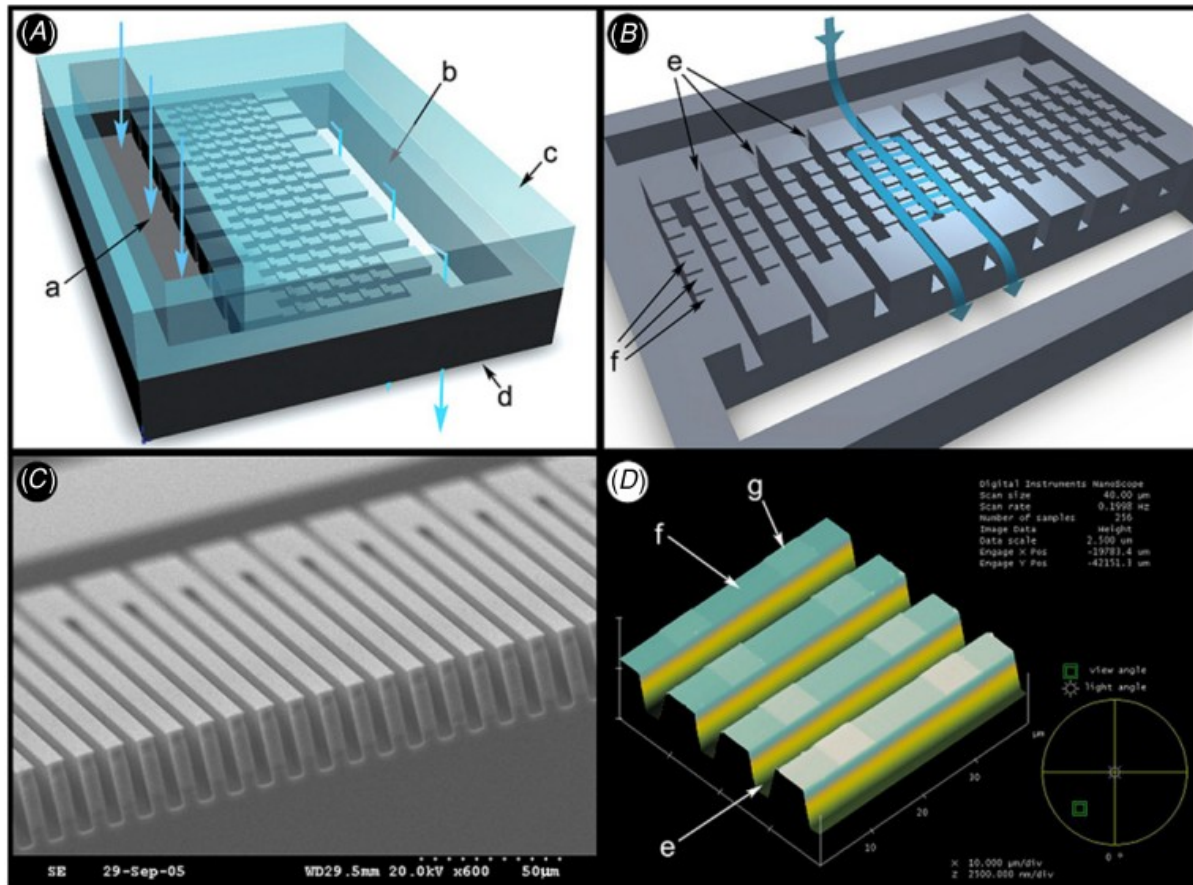


Figure 2.1.1 Schematics and images of a type of nDS membrane [Grattoni *et al* 2009].

- (A) 3D representation of the membrane;
- (B) inner structure of the device;
- (C) SEM image of the micro-channel cross section;
- (D) AFM image of a portion of the silicon substrate.

Legend: membrane inlet (a), outlet (b), Pyrex layer (c), silicon layer (d), microchannels (e), nanochannels (f), anchor points (g).

Figure 2.1.1 represents schematics and micrographs of an nDS membrane structure [Grattoni *et al* 2009], which consists of two sandwiched layers: a silicon structural layer and a Pyrex-glass cap. The silicon layer –which is bulk nano- and micro-machined– houses the mesh of micro- and nano-channels; the Pyrex layer –whose aim is having the unaccessible channels optically-inspectable— determines the top-surface of all the channels; the two layers are joined by anodic-bonding. The silicon wafer presents an inter-digitated finger geometry,

composed of parallel micro-channels connected to each other by a set of perpendicular nano-channels (**Figure 2.1.1B**). Fluids enter the membrane inlet (a, **Figure 2.1.1A**), flow horizontally into a set of micro-channels (e, **Figure 2.1.1B**), turn into the mesh of nano-channels (f, **Figure 2.1.1B**) and finally reach the outlet (b, **Figure 2.1.1A**) through another set of micro-channels.

Devices quality-control

Micro- and nano-fluidic devices are both commercially available and under development for a variety of applications, such as bio-molecular separation, drug-delivery, sensors, cell transplantation chips. Regulatory approval for the commercialization of these products requires the ability to fabricate large number of devices with high reproducibility and precision. For quality control and nano-features measurement of such devices, traditional microscopy and particle rejection characterization techniques, though extremely useful, are expensive and inadequate; instead, a fast and non-destructive device-selection method has been recently presented [Grattoni *et al* 2009], using convective nitrogen flow to detect structural defects in complex micro-/nano-channeled drug-delivery systems (nDSs), combining a predictive multi-scale theoretical mathematical model, which bridges the fluidics at micro- and nano-scales, with experimental analysis, consisting in gas flow through micro- and nano-channels of nDS devices, whose structure is inaccessible. This method presents advantages in terms of reducing both the operative cost and the testing time; its accuracy and reliability in detecting major and minor defects of various kinds was verified.

2.1.3 Experimental methods common to Sections 2.2 and 2.3

nDS structure/functioning

In the present study, nDS membranes as that pictured in **Figure 2.1.2** and internally-represented in **Figures 2.1.3÷5** were used; their structure and fabrication-process are described subsequently.

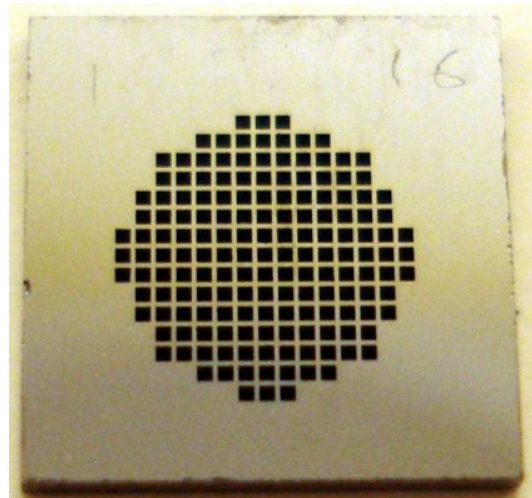


Figure 2.1.2 Photograph of one of the nDS membrane used.

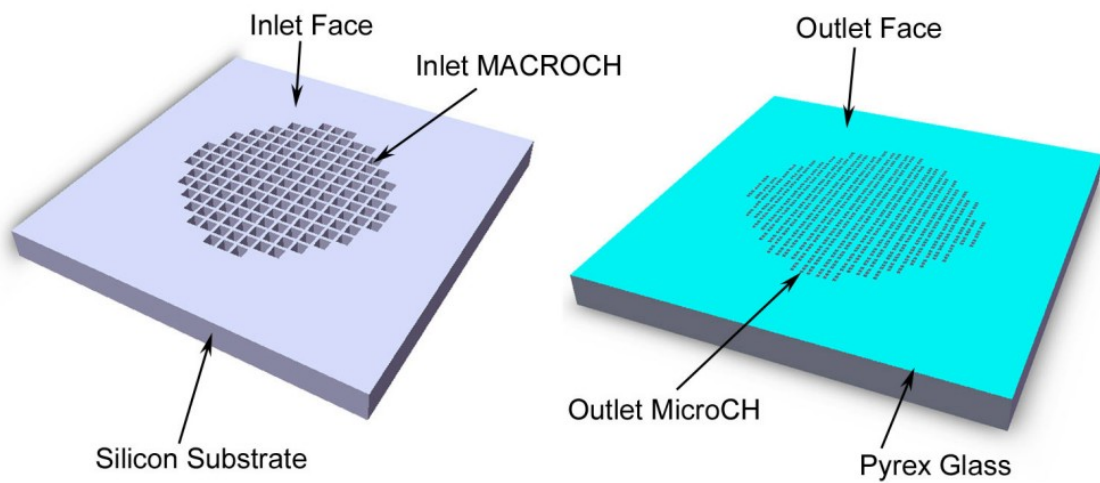


Figure 2.1.3 Schematic of used nDS membranes

Legend: 'MACROCH' macro-channel, 'MicroCH' micro-channel.

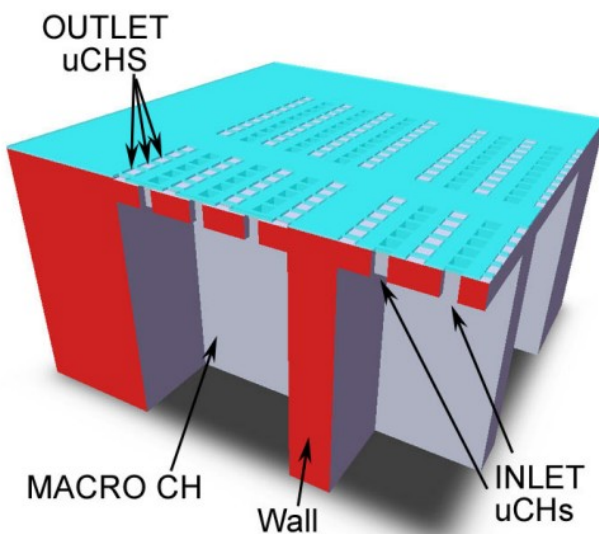


Figure 2.1.4 3D schematic of the nDS inner structure.

Legend: 'MACRO CH' macro-channel, 'uCH' micro-channel.

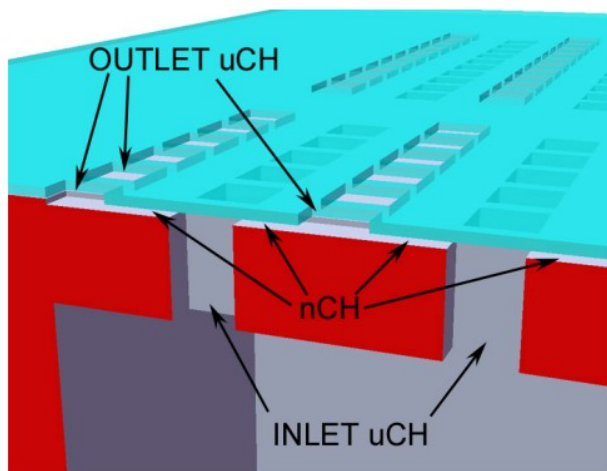


Figure 2.1.5 3D schematic of the nDS microstructure.

The nDS membrane depicted in **Figures 2.1.2÷5**, which has been used in all the experiments performed in the present thesis, consists –as its ancestor presented in **Figure 2.1.1**– of a silicon structural layer, which is bulk nano- and micro-machined. It houses a mesh of macro-, micro- and nano-channels.

The ‘diffusion path’ can be idealized as follows. The inlet face (**Figure 2.1.3**) is wet by the reservoir solution (solute to be diffused + solvent); the solute molecules diffuse through the inlet macro-channels (**Figures 2.1.3÷4**); after that, they diffuse through the inlet micro-channels (**Figures 2.1.4÷5**); after that, they diffuse through the nano-channels (**Figure 2.1.5**); after that, they diffuse through the outlet micro-channels (**Figures 2.1.5÷3**); eventually, they reach the outlet face (**Figure 2.1.3**), which was initially-wet by the sink solution (solvent only), but that over time starts containing solute. In order to re-establish the sink condition, the solution contained in the sink chamber is periodically substituted –with a pre-determined frequency– with fresh, new solvent.

The silicon substrate presents a mesh structure that grants the mechanical resistance to the membrane. The mesh is composed of 50 μm -thick walls which create a regular pattern of inlet macro-channels (190x190 μm). **Figure 2.1.3** shows a 3D schematic of the nDS membrane.

The macro-channels enter the bulk silicon with a depth of $470\mu\text{m}$, leaving a $30\mu\text{m}$ -thick solid silicon layer at their bottom. **Figure 2.1.4** shows a deeper 3D schematic of the membrane structure.

The inlet micro-channels are perpendicularly-etched through the silicon layer at the bottom of the macro-channels, presenting a length of $30\mu\text{m}$. The outlet micro-channels are etched into the Pyrex glass perpendicularly to the glass surface. The nanochannels, parallel to the silicon surface, are fabricated in the silicon substrate facing the Pyrex glass. **Figure 2.1.5** shows the micro-structure of the nDS.

As shown in **Figures 2.1.2÷3**, the surface of the nDS membrane is divided in square areas, corresponding in number, size, location to the inlet macro-channels. Each square presents 24 lines of inlet and outlet micro-channels connected by nano-channels. The lines are separated by supporting walls on which the Pyrex glass bond to the silicon substrate.

Figure 2.1.6 shows a picture of one square area.

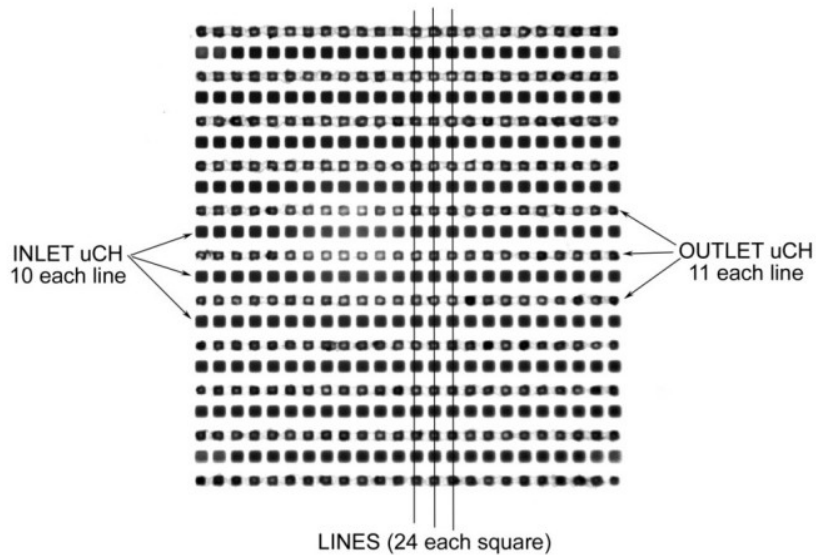


Figure 2.1.6 Optical micrograph of a square area (macro-channel).

The nanochannels –not visible because of the small color-contrast respect the anchor walls– connect the inlet and outlet microchannels in the drawn lines direction.

The nDS membranes can be fabricated with different nano-channel sizes, namely depth and length. **Tables 2.1.1** and **2.1.2** list the size and numbers for some of the possible nDS configurations, respectively.

MacroCH	IN microCH	nanoCH	OUT microCH
W	190 um	5 um	5 um
D	190 um	5 um	13, 20, 35 nm
L	470 um	30 um	1, 2, 3, 5 um

Table 2.1.1 *nDS nominal sizes.*

The nDS membranes are named with the following convention: nDS '**D x L**', where *D* represents the depth of the nanochannels (in nm), *L* represents the length of the nanochannels (in micron).

Legend: 'CH' channel.

	per line	per SQUARE	per nDS1
# MacroCHs - squares			161
# lines		24	3864
# inlets	10	240	38640
# outlets	11	264	42504
# nCHs	20	480	77280

Table 2.1.2 *nDS in numbers.*

Legend: 'CH' channel.

The nanometric dimension of the nanochannels is the height, which is obtained by using a sacrificial-oxide technique [Sinha *et al* 2005].



nDS devices microfabrication

The nDS membrane is composed of a silicon substrate and a thin Pyrex glass capping layer, which is anodically-bonded to the silicon substrate. The Pyrex glass creates the top surface of the nanochannels. The thickness of this sacrificial oxide determined the height of nanochannels, i.e. height of nanochannels = $0.46 \cdot \text{thickness of oxide}$.

More in details, the membranes were fabricated in an academic clean-room (Microelectronics Research Center, The University of Texas at Austin, TX, USA).

The major microfabrication steps –including silicon structural-wafer machining, glass-cap machining, anodic bonding– can be summarized as follows [Grattoni *et al* 2009].

First, the nano-channels were formed on the double-side polished silicon wafer, using a sacrificial-layer technique. A thermal oxide film was thermally-grown on the nano-channel area, and subsequently removed. The thickness of the oxide film (l) determined the height of nanochannels (H), by the oxide-consumption equation: $H = 0.46 \cdot l$.

Then, micro-channels as well as the inlet and outlet chambers were etched to the specified depth by using inductively-coupled plasma (ICP) deep silicon etching process (Oxford Plasmalab 100). The rectangular through-holes were then etched into the silicon wafer using 45% KOH solution at 80°C to create the membrane outlets. The silicon wafers were then checked with a Scanning Electron Microscopy (SEM – LEO 1530) to verify the pattern regularity. The roughness of the surface of the channels and the actual heights of the nanochannels of all nDS configurations were measured by atomic force microscopy (AFM – *Digital Instruments* Nanoscope IIIa).

The entry ports were processed in the glass cap using a dry etching process by an outside vendor (Sensor Prep Services Inc).

Finally, the glass and silicon structural layers were aligned and anodically-bonded.

At the end of the process, the nDSs were cleaned with Piranha solution (66%v/v H₂SO₄ in H₂O₂) for 12 hours at 120°C. The membranes were then soaked for 5 days in DI water, which was replaced every 12 hours. The water was then replaced by isopropanol for 3 days by performing several rinsing. Finally, the membranes were dried in oven at 100°C under vacuum for 12 hours.

nDS devices characterization and selection

Before performing any concentration-driven transport experiment, a nDS membrane devices selection was done, in order to remove possibly-defective ones. This selection consisted in a qualitative optical microscope evaluation followed by a quantitative pressure-driven gas test. The objective of this membrane characterization was the analysis of the fabrication process and the selection of membranes for subsequent passive diffusion testing.

nDS devices characterization and selection: optical microscopy

All nDS membranes were selected by using an optical microscope. All membranes presenting visible defects (micro-sized) were discarded.

More in detail, after having being microfabricated and cleaned, the nDS membranes were selected by using an upright optical microscope (*MTI Corporation XJM213*). Due to their peculiar structure, the nDS membrane can be observed with reflecting or transmitted light. However, if observed from the silicon side, a light effect in the macro-channels does not allow focusing on the inlet micro-channels, resulting in a blurry image; thus, the membranes were observed from the Pyrex side, making all channels visible. **Figure 2.1.7** shows two images of the same sample which were captured with transmitted and reflected light.

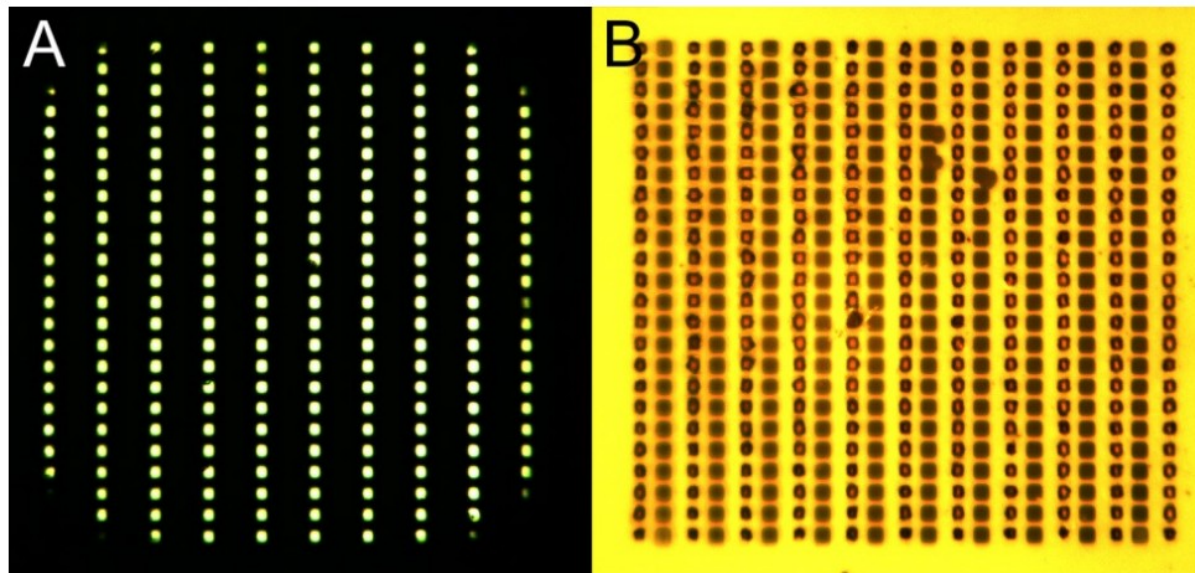


Figure 2.1.7 Observation of the nDS membrane with transmitted (**A**) and reflected (**B**) light.

The observation with transmitted light allows to quickly identifying major damages in the membrane structure, such as totally-through holes (**Figure 2.1.8**). It also allows evaluating the number of open inlet micro-channels (**Figure 2.1.9**).

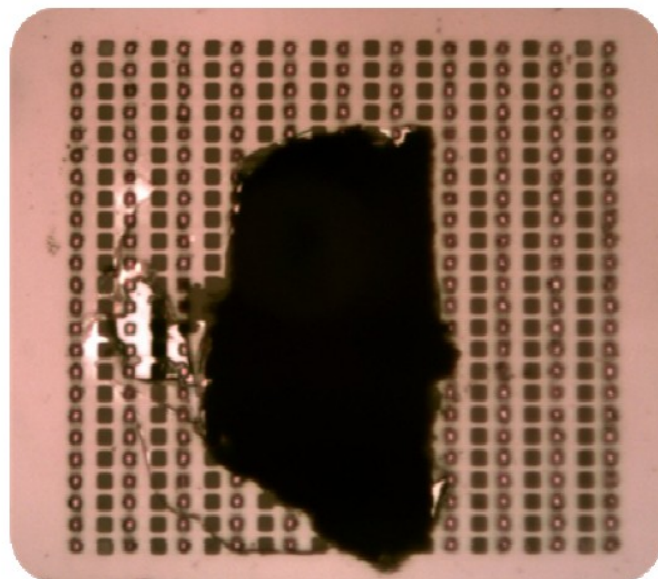


Figure 2.1.8 Through-hole.

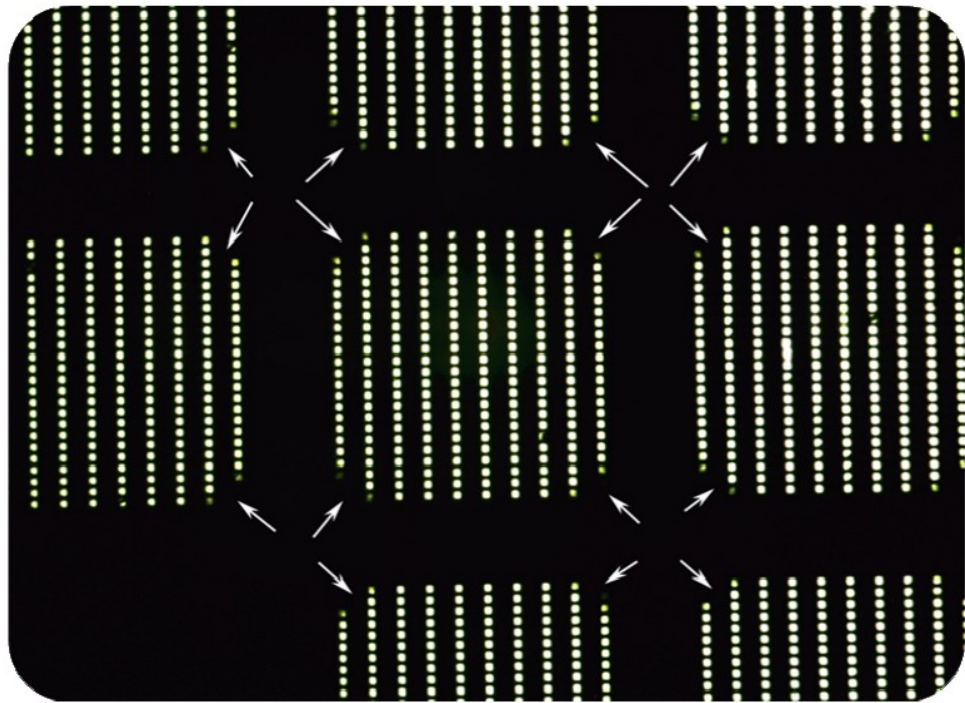


Figure 2.1.9 Unfinished inlet-microchannels.

The observation with reflected light is necessary to analyze the outlet micro-channels (Figure 2.1.10), the nano-channel pattern, the quality of the Pyrex glass (Figure 2.1.11).

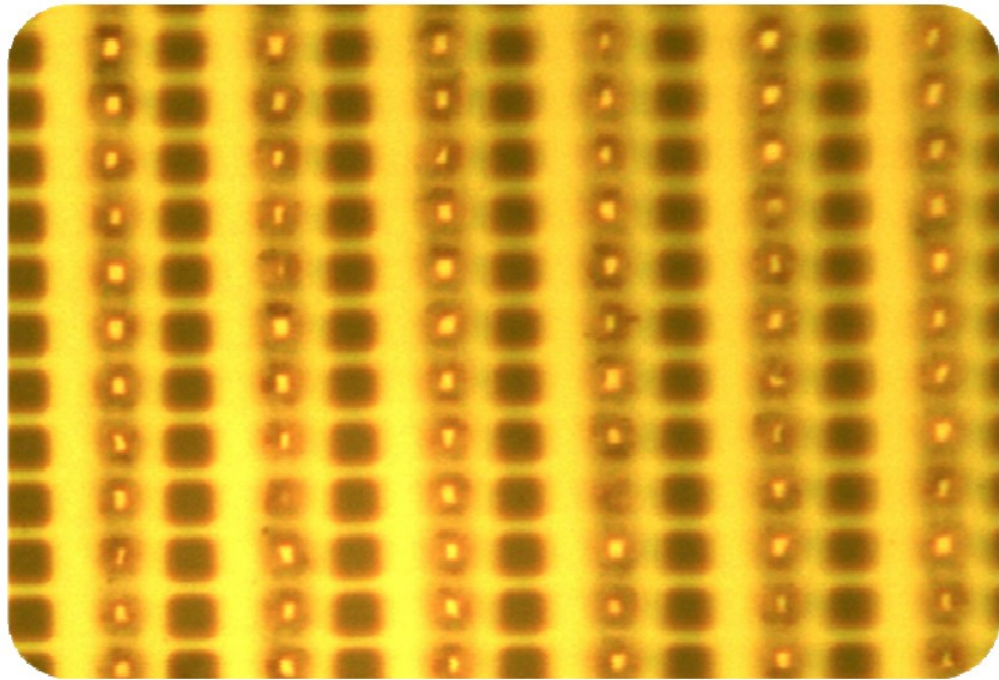


Figure 2.1.10 Irregular shape of the outlet-microchannels.

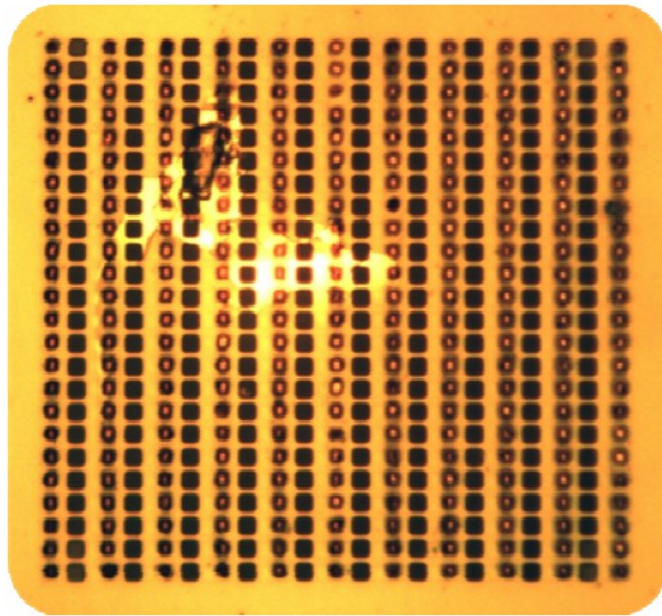


Figure 2.1.11 Broken Pyrex-glass.

Tommaso Novellino
24

Sometimes, macro-channels were also clogged (**Figure 2.1.12**).

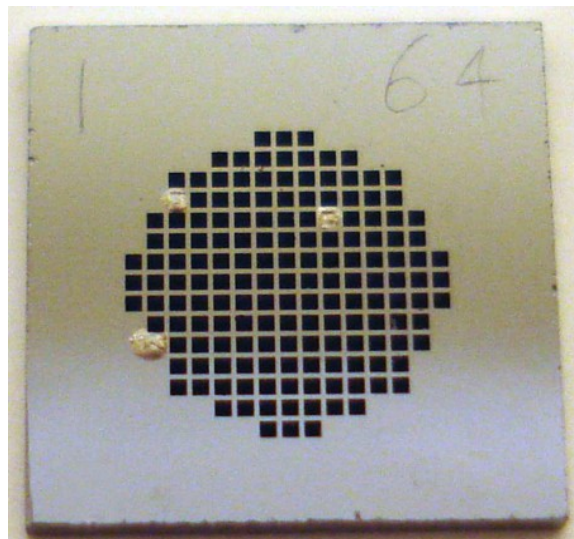


Figure 2.1.12 Clogged macrochannels.

For the purpose of selecting the devices for further passive diffusion testing, all membranes presenting unetched microchannels or remaining metallic masks were discarded.

nDS devices characterization and selection: gas testing

After optical observation, the gas-flow membrane characterization was performed, using a custom gas-testing system [Grattoni *et al* 2009], composed of (**Figure 2.1.13**):

- a high purity nitrogen tank (*Matheson Tri-Gas* Research Purity Grade 99.9999%),
- a dual stage pressure regulator (*Matheson Tri-Gas* 3120-580),
- a membrane holder,
- an electromagnetic clamping system,
- a pressure transducer (*Ashcroft* Full Scale 60 psi, accuracy 1%),
- a system of pipes and connections.

Particularly, the membrane holder (**Figure 2.1.13B,C**) was designed to assure perfect sealing, housing one nDS and a silicon-rubber custom seal (molded by *Apple Rubber*, Lancaster, NY, USA). It was made of a stainless steel SS316 machined disk and an electromagnet that clamps the membrane between two o-rings.

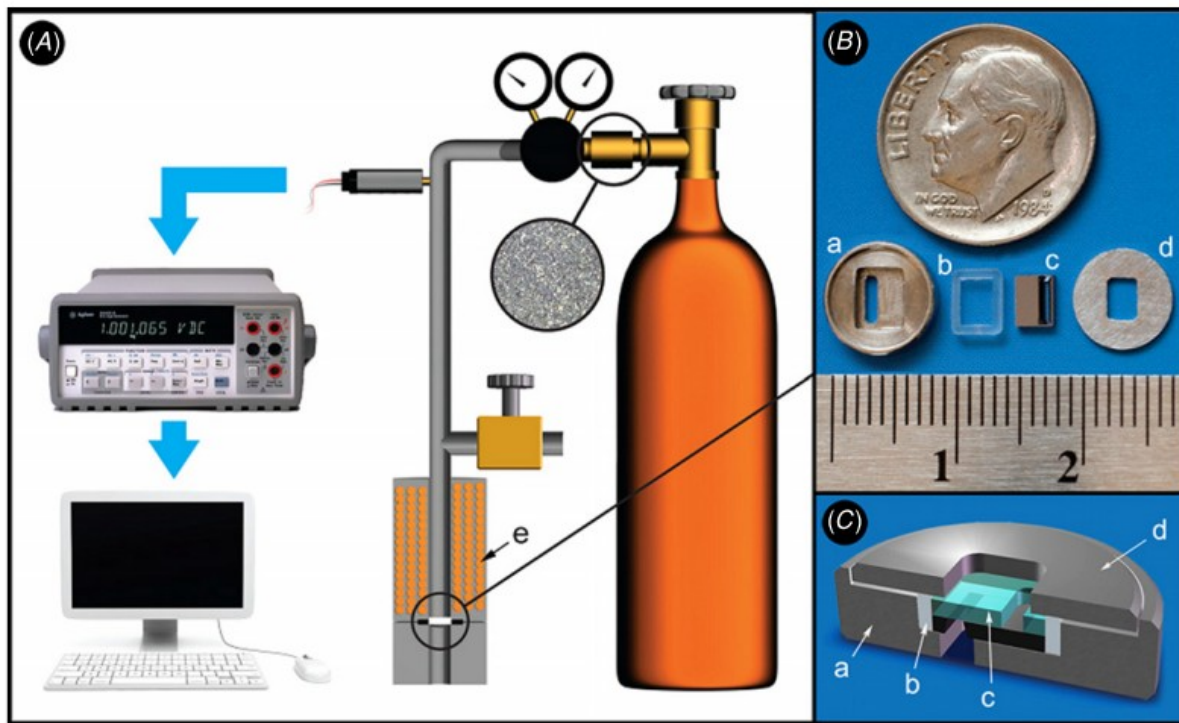


Figure 2.1.13 Schematic of the used gas-testing system [Grattoni *et al* 2009].

(A) The system is composed of: a high-purity nitrogen tank, a dual-stage pressure regulator with gas filter, a pressure transducer, an electromagnetic clamping system, a membrane holder, a system of pipes and valves and connections.

(B) and (C) show a zoom of the membrane and its clamping accessories, in parts and assembled (cross section), respectively.

Legend: membrane holder (a), silicon-rubber seal (b), nDS membrane (c), holder lid (d), electromagnetic clamping system (e).

A more detailed schematic of the gas testing system is given in **Figure 2.1.14**.

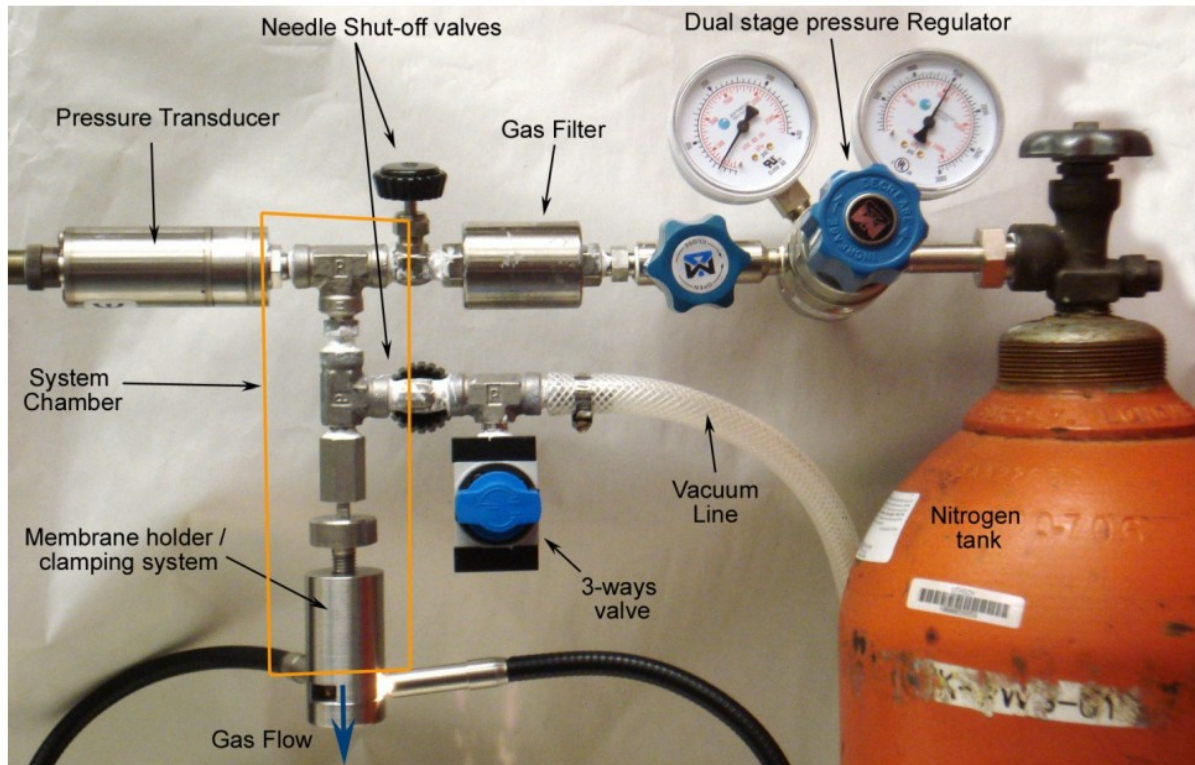


Figure 2.1.14 Gas-testing system details.

The membrane holder/clamping system is shown in **Figure 2.1.15**.

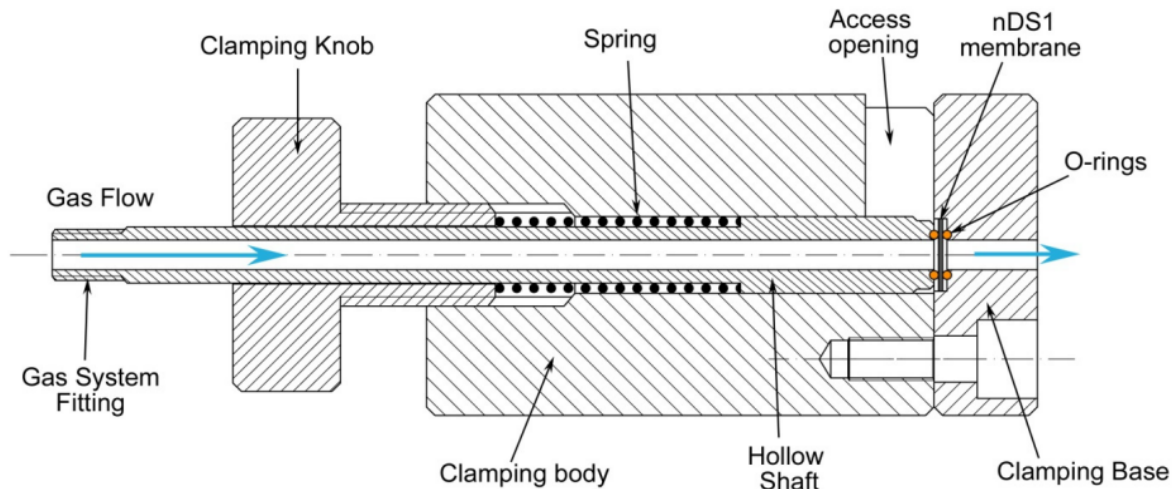


Figure 2.1.15 nDS membrane clamping system.

The membrane clamping system is composed of:

- a hollow shaft,
- a clamping body,
- a clamping base,
- a clamping knob,
- a spring,
- two precision O-rings (*Apple Rubber*, Lancaster, NY, USA).

The shaft can axially slide into a guiding hole machined into the clamping body. The clamping base houses a precision groove for an O-ring and for the nDS membrane. The shaft is pressed against the membrane through the clamping force operated by a spring, which compression can be tuned by adjusting the position of the clamping knob. By turning the knob to a specific position, the same clamping force can be applied on each nDS membrane during the gas testing: this minimizes the variability of the gas testing results.

The gas-test system, which showed negligible leakage and unrepeatability, was used as described in [Grattoni *et al* 2009].

Practically, in order to generate a pressure-driven nitrogen flow across the nDS structure, the experimental apparatus [Grattoni *et al* 2009] shown in **Figure 2.1.13** was used, which takes advantage of the sensitivity of the flow to structural and geometrical features and surface properties of the channels, in order to detect structural defects in nDS.

The following gas testing procedure has been used. First, a membrane was placed inside the grooves in the clamping base. The shaft was then pressed against the membrane by loading the spring through the clamping knob. The knob was always turned to a position corresponding to a clamping force of 30N. After the membrane was secured, the vacuum valve was opened briefly to remove any air from the system (absolute pressure 15.6kPa). Once the vacuum valve was closed, the filtered N₂ gas was allowed into the system until the hand-held multimeter read 1.134±0.005 V (corresponding to a pressure of about 0.31MPa). After the system had become saturated with N₂ gas, all valves were closed and the system was insulated from the gas tank at $t_0 = 0$ seconds. The system pressure drop due to the gas flow throughout the membrane was measured and the data were collected with a digital

multimeter (model 34410A, *Agilent Technologies*, Santa Clara, CA, USA) at 2 Hz for 300 seconds.

The membrane was clamped in its holder and the system was filled with nitrogen at the relative pressure of 0.31 MPa, by previously vacuuming the air entrapped (absolute pressure 15.6 kPa). The system was then insulated from the nitrogen tank at $t = 0$ seconds. The system pressure-drop due to the gas flow throughout the membrane was measured, and the data were collected with a digital multimeter (model 34410A, *Agilent Technologies*, Santa Clara, CA, USA) at 0.1 Hz for 700 seconds.

The pressure drop is well described by a single exponential decay, consistent with the solution to a one-dimensional transient problem [Roy *et al* 2003]. The collected pressure-data were thus fitted with an exponential function (correlation coefficient R_c always > 0.999). The interpolation was performed to resample each curve and in a time range of 660s starting from a relative pressure of $k = 0.31$ MPa. The cumulative amount of nitrogen $F(t_i)$ [g] released through time t_i was calculated through the relation:

$$F(t_i) = \frac{V_{\text{sys}} \text{MW}}{RT} (p(t_0) - p(t_i)) \quad (\text{Equation 2.1.6})$$

where V_{sys} is the testing system volume, $\text{MW} = 28.02$ g/mol is nitrogen molecular-weight, R is the ideal gas constant, T is the temperature of the gas in the reservoir (always $275 \text{ K} \pm 0.3 \%$), $p(t_0)$ is the starting pressure and $p(t_i)$ is the pressure at the i^{th} instant. Finally, the mass-flow rate [g/s] was calculated as the derivative of the cumulative amount over the time:

$$\dot{m}(t) = \frac{dF(t)}{dt} = \frac{V_{\text{sys}} \text{MW}}{RT} \beta k \times e^{-\beta t} = \text{const} \cdot \beta \cdot p(t) \quad (\text{Equation 2.1.7})$$

A statistical analysis was performed on the mass flow rate data obtained for each configuration. The mean and the 25th, 50th, 75th percentiles and the skewness –defined as the ratio between the third moment about the mean and the variance– were calculated. The mean of the data related to each configuration was verified to be significantly-different through one-way ANOVA test (*OriginLab Corp Origin Pro*) performed at a significance level of $\alpha = 0.005$.

A standard characteristic fluidic curve was determined for each nDS configuration. A linear dependence of the mass flow rate on the inlet–outlet pressure difference is observed in the considered pressure range 0.3÷0.15 MPa. The deviation of the data from an ideal normal distribution (skewness) can be caused by errors encountered during the fabrication process; systematic defects can be reproduced during the simultaneous processing of several devices on the same wafer, consequently the deviation of the device structure from its nominal design may be non-random.

nDS devices diffusion-test set-up

In order to perform the actual diffusion test in the so-called ‘*in-lab*’ condition (meaning in an abiological environment, as opposed to a biological environment as in the *in-vivo* situation), the nDS were assembled into a customly-assembled testing-device. The testing-device was composed by:

- two stainless steel SS316L bodies,
- two silicon rubber O-rings (*Apple Rubber*, Lancaster, NY, USA),
- two silicon rubber caps (*Mocap Inc*, St. Louis, MO),
- two SS316L screws and nuts.

Figure 2.1.16 shows the picture of one such testing-device, both its parts and its assembled version.

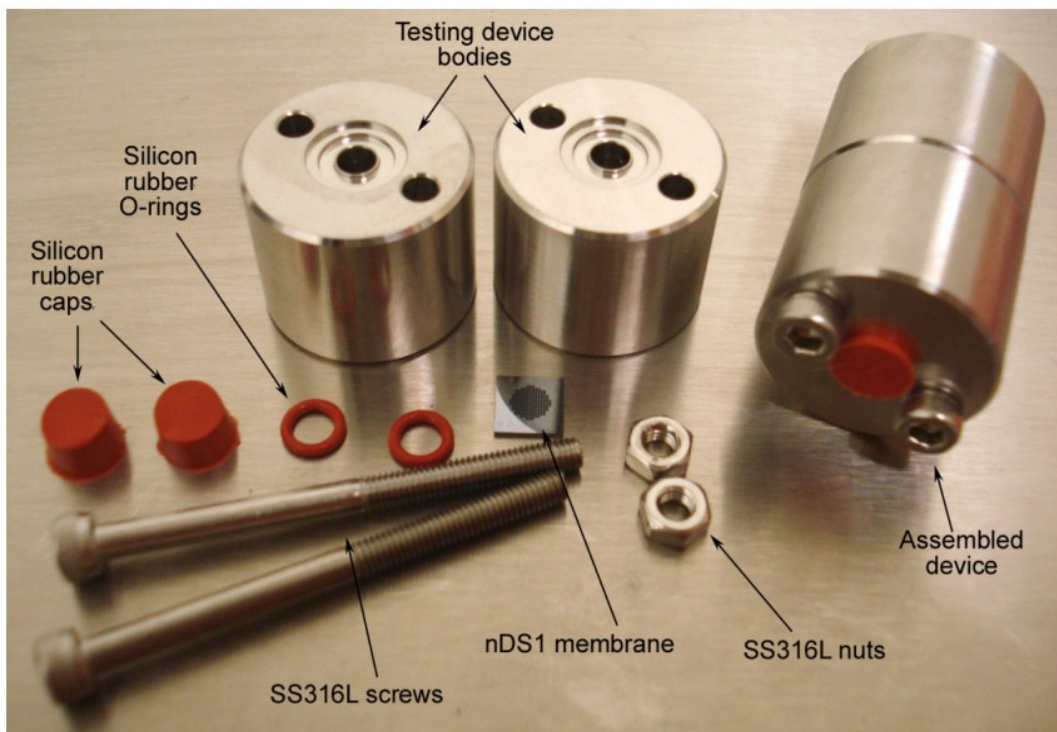


Figure 2.1.16 Testing-device, parts (**left**) and assembled (**right**), used in all the ‘in-lab’ experiments.

The testing-device bodies are hollow, designed to be the ‘reservoir’ (chamber containing the solution to be tested) and the ‘sink’ (chamber containing the solvent only). They present a groove which precisely fit the nDS membrane. A smaller inner groove is also machined to house the sealing O-rings. The nDS membrane is positioned in its groove on one device body. The membrane is then clamped in between the two bodies which are pressed together by tightening the screws. **Figure 2.1.17** shows the testing-device assembling.

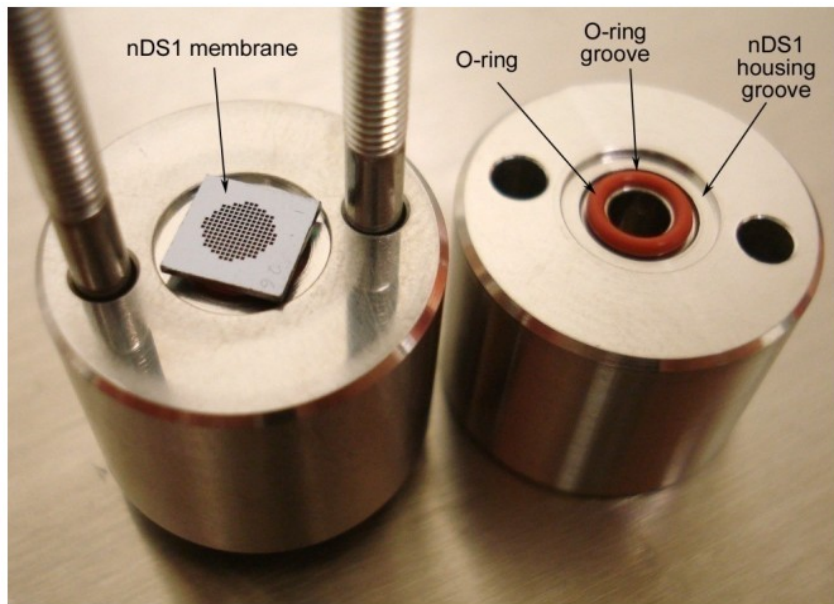


Figure 2.1.17 Testing-device assembling.

Evaporation test

In order to support the experimental analysis, a pre-evaluation consisting in an evaporation test of the testing-devices was performed. The amount of solvent evaporating form testing-devices was evaluated.

The solvent evaporation test was performed determining the daily evaporation of fluid from

two testing-devices, each clamping one solid silicon chip resembling the nDS membrane. The testing-device chambers were both filled with PBS (200 μ L in each chamber). The chambers were then capped. The devices were weighed on an electronic scale (*Metter Toledo XP56 DeltaRange Microbalance, resolution 10 μ g*). The measurement was performed in triplicates, and repeated every 24 hours.

Table 2.1.3 shows the results of the evaporation test, demonstrating that a negligible amount of fluid evaporated from each diffusion testing-device in each day.

		#1		#2	
Date	Day	AVG Weight	Std Dev	AVG Weight	Std Dev
17-Dec	1	76.8322g	0.0001g	76.5138g	5.7E-05g
18-Dec	2	76.8320g	0.0001g	76.5137g	0g
Avg. Evap. per day		0.2uL		0.1uL	

Table 2.1.3 *Evaporation-test results.*

nDS devices diffusion-test preparation

Before proceeding with the actual diffusion release test, the following chronological preparation procedure was performed:

1) Testing-device cleaning

The testing-devices parts (bodies, screws, o-rings, caps) were immersed in a bath of water and soap, and accurately cleaned. The devices were then rinsed multiple times and dried by compressed air. The parts were then autoclaved for 20min at 121°C.

2) Testing-device assembly

The O-rings were placed in the inner grooves of the device bodies. The screws were inserted in one of the bodies, in order to aid the alignment of the two bodies during the clamping procedure. The nDS membrane was placed on top of one O-ring in the housing groove (see **Figure 2.1.17**). The bodies were then clamped together and the screw fastened, guaranteeing the sealing of the two fluid chambers.

3) nDS-membrane wetting

After assembling the testing-device, ethanol was loaded into the fluid chamber facing the silicon side of the membrane and both chambers were plugged with the silicon rubber caps. Then, the nDS device was kept oriented such that the ethanol sat on top of the nDS, and the system was allowed to rest overnight.

Ethanol was then added in the other chamber to create the continuity of fluid between the two chambers through the membrane. The ethanol was carefully removed from both sides not allowing the channel area to dry, and de-ionized water (DI-H₂O) was promptly put into both chambers. The DI-H₂O was replaced 3 times. Then the chambers were plugged, and the system was allowed to rest for 6 hours.



Tesi di dottorato in Ingegneria Biomedica, di Tommaso Novellino,
discussa presso l'Università Campus Bio-Medico di Roma in data 10/03/2011.
La disseminazione e la riproduzione di questo documento sono consentite per scopi di didattica e ricerca,
a condizione che ne venga citata la fonte.

After the resting period, the DI-H₂O was replaced 3 more times with fresh DI-H₂O,
and the system was allowed to rest overnight again.


Tommaso Novellino
34

2.1.4 Personal contribution

My contribution to the project has been mainly related to the optical selection of the nDS chip in view of an accurate experimental analysis and the preparation, set-up of the diffusion testing.

2.2 Release of drug from nanochanneled devices implanted in rats

This study, an *in-vivo* and '*in-lab*' release study of human interferon alpha, was developed to possibly find a correlation between *in vivo* and the *in lab* nDS devices release data.

Human interferon-alpha-2b (IFN) was chosen as molecular probe due to its long *in vivo* half-life and its *in vivo* detectability with good sensitivity. *In vivo* (inside rats) and *in lab* (i.e. inside testing-devices) experiments were performed with nDS devices ('membranes') of the same configuration and batch.

In vivo capsules were produced by NMS company. They were loaded with IFN and implanted in healthy rats subcutaneously; then, the human IFN content in the rats blood was measured, and so the release of IFN from nDS membranes assessed; it was also compared to IFN directly administered via subcutaneous injection.

In lab testing-devices were those described in Section 2.2.2 (e.g. **Figure 2.1.16**).

2.2.1 Interferon

Interferon functions

Interferons (IFNs) are proteins –belonging to the large class of glyco-proteins known as cytokines– made and released by lymphocytes in response to the presence of pathogens – such as viruses, bacteria, parasites– or tumor cells. They allow communication between cells to trigger the protective defenses of the immune system that eradicate pathogens or tumors.

All interferons share several common effects; they are antiviral agents and can fight tumors. More in details, IFNs have a several functions:

- interfere with viral replication within host cells;
- activate immune cells, such as natural killer cells and macrophages;
- increase recognition of infection or tumor cells by up-regulating antigen presentation to T lymphocytes;
- increase the ability of uninfected host cells to resist new infection by virus.

Interferon types

About ten distinct IFNs have been identified in mammals; seven of these have been described for humans. They are typically divided among three IFN classes: Type I IFN, Type II IFN, and Type III IFN. IFNs belonging to all IFN classes are very important for fighting viral infections.

Based on the type of receptor through which they signal, human interferons have been classified into three major types:

- IFNs type I: they all bind to a specific cell surface receptor complex known as the IFN- α receptor (IFNAR); those present in humans are [Liu 2005]:
 - IFN- α
 - IFN- β
 - IFN- ω ;
- IFNs type II: bind to IFNGR; in humans, is IFN- γ ;
- IFNs type III: signal through a receptor complex consisting of IL10R2 (also called CRF2-4) and IFNLR1 (also called CRF2-12); type III classification is less universal than type I and type II [Vilcek 2003].

Interferon alpha

The interferon-alpha (IFN- α) proteins are naturally produced by leukocytes. They are mainly involved in innate immune response against viral infection. They come in 14 subtypes that are called: IFNA1, IFNA2, IFNA4, IFNA5, IFNA6, IFNA7, IFNA8, IFNA10, IFNA13, IFNA14, IFNA16, IFNA17, IFNA21.

IFN- α can also be made synthetically (e.g. recombinant [Nagata *et al* 1980]) and used as medication; medically-used IFN- α types are:

- Interferon alfa-2b (**Figure 2.2.1**): an anti-viral drug, marketed by *Schering-Plough* under the tradename *Intron-A*; used for a wide range of indications, including viral infections and cancers
 - approved around the world for the treatment of: chronic hepatitis C, chronic hepatitis B, hairy cell leukemia, chronic myelogenous leukemia, multiple myeloma, follicular lymphoma, carcinoid tumor, malignant melanoma;
- Pegylated interferon alfa-2a: the polyethylene glycol (PEG) protects the IFN molecule from proteolytic breakdown and increases its biological half-life;
- Pegylated interferon alfa-2b: developed by *Schering-Plough*, brand name is *Peg Intron*; is a treatment for hepatitis C (approved in 2001), and has also been shown to have optimistic effects in the treatment of malignant melanoma.

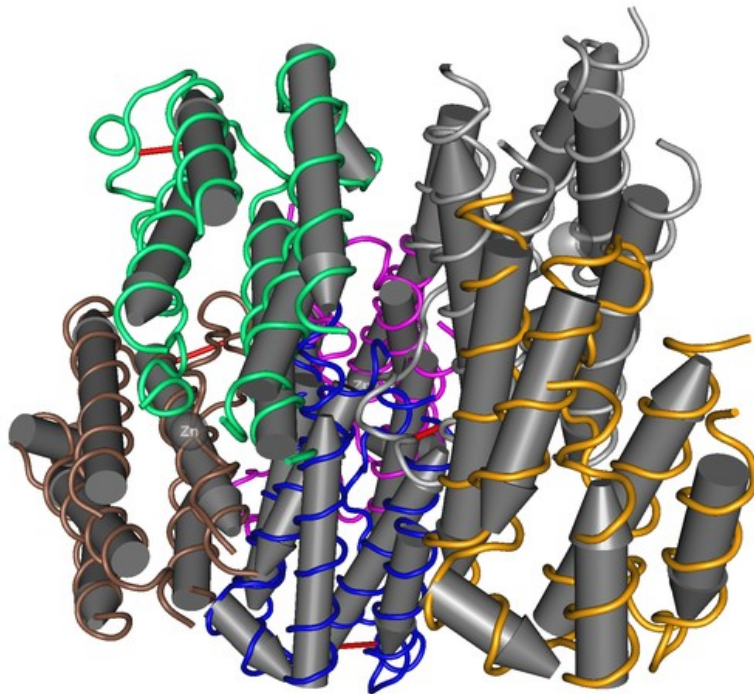


Figure 2.2.1 Molecular schematics of human interferon-alpha (recombinant human interferon- α -2b) [[Wikipedia](#)].

Human interferon-alpha-2b, for its wide medical use, was chosen and used in all the *in-vivo* and *in-lab* release experiments.

2.2.2 Experimental methods

Recombinant human interferon-alpha-2b was purchased from *Cell Sciences* (Canton, MA, USA).

Its concentration was detected by commercial sandwiched immuno-assay (ELISA, Enzyme-Linked ImmunoSorbent Assay, *Cell Sciences*) which was specific to human IFN but was not cross-reactive to IFN of rat species.

2.2.2.1 *In lab* study

Preliminary IFN stability test

In order to pre-emptively assess possible IFN *in vivo* degradation, two IFN stability test were performed at 37°C for over one month.

In the 1st test, 4 relatively-low concentrations (20, 17, 50, 42.5 µg/ml), similar to the one used in the *in lab* experiments, were evaluated for 35 days; in the 2nd test, 2 high-concentrations (1, 0.5 mg/ml), similar to the one used in the *in vivo* experiments, were measured for 32 days. In order to quantify the differences between actual concentrations and measured concentrations, standard curves were prepared with PBS (*GIBCO*) and ‘Diluent C’ (a component –whose aim is to dilute unknown-samples– taken from the used ELISA kit). Different dilutions of the prepared samples with Diluent C or PBS were measured with the ELISA kit to find the solvent and range of dilution improving precision and accuracy the most.

IFN release from nDS

nDS membranes of two geometrical/structural configurations were used – namely, 20x2 and 20x3 (i.e. nano-channel height = 20nm for both, nano-channel length = 2 and 3 µm respectively). 8 membranes were used for configuration 20x2; 11 membranes for configuration 20x3.

The nDS membranes, micro-fabricated at the above-mentioned Austin facility, were firstly selected by optical observation to detect holes and broken glasses presence; eventual

membrane holes were plugged with epoxy. They were then gas-tested and considered good if the pressure-range was $2.7 \div 3.05 \cdot 10^5$ Pa for configuration 20x2 and $2.45 \div 2.68 \cdot 10^5$ Pa for configuration 20x3. The membranes chosen for the actual release-experiment were then processed as follows.

Chosen membranes were assembled in cylindrical testing-devices as previously described. Then, they were wetted: first with ethanol, then with de-ionized water, finally with the test solvent (each step: 400 μ l, air-bubbles were checked and removed if present). More in detail, the wetting was performed as follows: the silicon sides of the membranes were wetted with ethanol, waiting 1h before capping with a silicon rubber; the Pyrex ones were then filled and capped; after waiting overnight, both sides were dried (not totally, to not dry the membrane) and filled with DI-water; after waiting 1h, DI-water was replaced, repeating this 5 times in total; finally, DI-water was dried (always leaving a veil of liquid) and the solvent used in the diffusion test (PBS for 20x2 and Diluent C for 20x3) was inserted, and replaced after 1h.

After wetting, the testing-devices were filled with the appropriate solutions as follows. Reservoir-chambers were filled with 300 μ l of 20 μ g/ml solution of IFN- α -2b (*Cell Sciences*), either dissolved in PBS for configuration 20x2 or in Diluent C for configuration 20x3. Sink-chambers, after being washed with the proper solvent (to remove eventual substance passed through the membrane during capping), were filled with 215 μ l of PBS (20x2) or Diluent C (20x3); a small stainless sphere was also added, to improve solution mixing.

The experiment (started on 2/10/2009 for configuration 20x2 and on 2/24/2009 for configuration 20x3) was performed at 4°C to hinder interferon degradation. ELISA measurement frequency was:

- during the 1st week, 1 measurement per day;
- during the 2nd week, 1 measurement every 2 days;
- then, twice per week.

The 20x2 experiment was stopped on 4/2/2009 after about 2 months (58 days); the 20x3 on 7/10/2009 after about 4 months (137 days).

In order to accelerate the evaluation of the diffusion of all the loaded IFN, reservoir solutions were diluted twice during the experiment, at day 72th and 102th, using a dilution-factor of 1:3 and 1:2, respectively. Each time, concentration (through ELISA) and volume

(through micro-pipette, estimated error $\pm 5\mu\text{l}$) of the reservoir solution were measured; the same has been done also after the end of the experiment.

Before sampling, testing-devices were put on a rotator to increase sample uniformity. A needle was used to decrease pressure, both when de-capping and when re-capping them. A certain amount ($200\mu\text{l}$ for 20×2 and $215\mu\text{l}$ for 20×3) of solution was taken from the sink chamber, and the same amount of fresh solvent (PBS for 20×2 and Diluent C for 20×3) was put back in it.

The IFN-concentration in the collected samples was measured with a specific ELISA Kit (*Cell Sciences CK2001*). The ELISA protocol permits to choose between two different modalities, which lead to two different standard-curve ranges: ‘extended’ ($5000\div 0\text{pg/ml}$) and ‘high-sensitivity’ ($500\div 0\text{pg/ml}$). For the *in lab* experiments, the first one was used, to reduce the dilutions required for the samples to fall within the standard-curve range.

ELISA micro-plates were read through a spectrophotometer; different spectrophotometer devices were used (*Bio-Tek, Tecan, Molecular Devices*), but their output data showed difference $<10\%$. Used spectrophotometer settings are reported in **Table 2.2.1**.

Modality	Absorbance
Type	End-point
Output	Optical density (OD)
Measurement wavelength	450nm
Reference wavelength	660nm

Table 2.2.1 *Spectrophotometer settings.*

Output data –optical densities (ODs)– were obtained measuring absorbance at 450nm. At each measurement, blank value (absorbance of pure Diluent C) was subtracted to all data and a new standard-curve was measured and used to convert *OD* in concentrations (*c*). Two fittings were used, which showed comparable results: a 4-parameter (*A, B, C, D*) fitting (**Equation 2.2.1**), reported in the ELISA protocol,

$$OD = D + \frac{A - D}{1 + \left(\frac{C}{D}\right)^B} \quad (\text{Equation 2.2.1})$$

and quadratic-polynomial fitting (**Equation 2.2.2**) with three parameters (A, B_1, B_2):

$$c = A + B_1 OD + B_2 (OD)^2 \quad (\text{Equation 2.2.2})$$

From the concentrations obtained from either **Equation 2.2.1** or **2.2.2**, the amount of IFN present in each well at each time (x_i) was calculated using the testing-device chamber volume; the cumulative release profile over time was simply obtained as follows:

$$x_{cum}(t_i) = x_1 + x_2 + \dots + x_i \quad (\text{Equation 2.2.3})$$

2.2.2.2 *In vivo* study

IFN titration in blood

Blood standard-curve was built by adding known IFN quantity to rat blood before serum separation, and measuring the IFN concentration in the serum. Diluent C was used as solvent.

Preliminary animal study

nDS release *in vivo* was performed using nDS membranes from the same fabrication wafer as the *in lab* release experiment; those membranes were housed in assembled bio-compatible implantable capsules, fabricated and processed by *NanoMedical System* (NMS – Austin, TX, USA) company. Those capsules can contain about a 1ml loading volume, are made of either titanium or polymeric (PEEK) material, and are cylindrically-shaped (**Figure 2.2.2**).

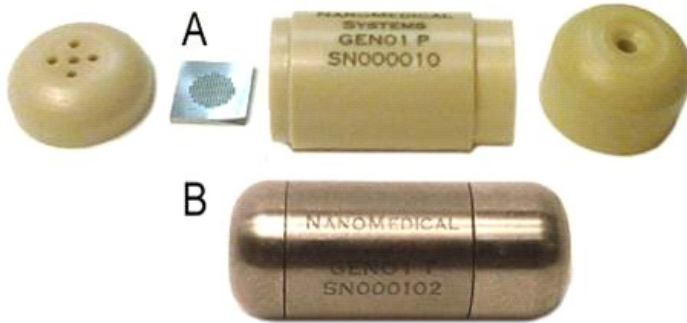


Figure 2.2.2 NMS-capsules in PEEK –disassembled– (**A**) and titanium –assembled– (**B**).

Capsules present a top-cap facing nDS membrane with 5 holes, and a bottom cap with only one hole to be loaded using a needle-syringe.

Experiment started on May 29th 2009 and lasted 31 days (until 6/30/2009).

12 healthy Sprague-Dawley female rats were used for the animal study and divided in 4 groups, as reported in **Table 2.2.2**.

Group ID	Treatment	Loading concentration	# Rats per group
1	<ul style="list-style-type: none"> • NO Capsule • NO IFN 	0	2
2	<ul style="list-style-type: none"> • Capsule with nDS 20x2 loaded with IFN 	1 mg/ml	3
3	<ul style="list-style-type: none"> • NO Capsule • IFN-α administered intravenously 	Different amounts every week	3
4	<ul style="list-style-type: none"> • Capsule with nDS 20x2 filled of vehicle (water) • NO IFN 	0	2

Table 2.2.2 Experimental set-up and rat grouping.

Tommaso Novellino
 44

Capsules were inserted into sub-scapular region using aseptic technique in anesthetized (isoflurane) animals, according to **Table 2.2.2**. Before implanting the capsules, rats were anesthetized and, after having shaved the area, a cut –big enough to let the capsule enter– was performed by knife in the sub-scapular region. Incision was then closed with 3÷4 metal stitches (staples).

Properties of the 5 capsules implanted in the rats are reported in **Table 2.2.3**.

Group #	Rat #	Material	loading solution
2	1	Ti	IFN solution
2	2	Ti	IFN solution
2	3	PEEK	IFN solution
4	1	PEEK	Millipore water
4	2	Ti	Millipore water

Table 2.2.3 Properties of each implanted capsule.

The capsules were fabricated, assembled and sealed by NMS; upon arrival, they were autoclaved as delivered. Before implant surgery, capsules were filled according to **Table 2.2.3** under biological hood and then left submerged in Millipore water under UV light inside the hood for 30min to increase the sterilization of their surfaces.

NMS capsules implanted in group 2 and group 4 were loaded with 0.9 mg/ml IFN (human IFN- α -2b, *Cell Sciences*) solution and vehicle only (Millipore water), respectively. The other two groups had no capsules: group 1 was a negative control (no IFN and no capsule), while rats belonging to group 3 were subcutaneously-injected with 200 μ l of IFN solution (in Millipore water) once a week.

For group 3, a different concentration was injected every week, according to **Table 2.2.4**. Injection was performed, through a 28G1/2 needle (13mm), in the sub-scapular region.

Draw/injection		IFN injected: mass (concentration)
Date	Day #	
5/29/2009	1	–
6/1/2009	4	5.7 µg (28.8µg/ml)
6/4/2009	7	–
6/11/2009	14	5 µg (25µg/ml)
6/15/2009	18	2.5 µg (12.5µg/ml)
6/18/2009	21	–
6/22/2009	25	1.25 µg (6.25µg/ml)
6/30/2009	33	1 µg (5µg/ml)

Table 2.2.4 Blood-drawing and IFN-injection schedule.

Table 2.2.4 shows the overall experimental plan, where groups 1÷4 were drawn blood on all the reported days, while group 3 only was injected IFN only in some of them.

Rat blood was drawn in order to measure its human IFN content. It was drawn from the venous plexus of the orbit 2 times per week according to **Table 2.2.4**. Each time, 500µl of blood from each rat were taken; for group 3, the blood drawing was performed 2h after IFN-injection.

IFN concentration was measured in serum using ELISA kit for *in vivo* samples (*Cell Science CK2003*) at the ‘high-sensitivity’ range (500÷12.5 pg/ml).

Experiment lasted 33 days (from 5/29/2009 to 6/30/2009). At the end of the experiment, the animals were sacrificed by carbon-dioxide asphyxiation. From the animals of group 2 and 4, the implanted capsules were explanted and visually-checked for eventual fibrous encapsulation. Several biopsies were also taken, both from the implantation region (wounded skin) and far from it (healthy skin). Harvested tissues were fixated in formalin and stained with Hematoxylin and Eosin (H&E) or Myeloperoxidase to perform histological analysis, particularly to quantify inflammation and immune response. Volume and concentration of solution contained in each capsule were measured.

In order to determine if the age of the rat was significant, 2 more rats one month older were also treated as group 1 and group 2, respectively. Moreover, 8 more of these older rats

Tesi di dottorato in Ingegneria Biomedica, di Tommaso Novellino,
discussa presso l'Università Campus Bio-Medico di Roma in data 10/03/2011.
La disseminazione e la riproduzione di questo documento sono consentite per scopi di didattica e ricerca,
a condizione che ne venga citata la fonte.

were also injected with different IFN dose once to better assess the correlation between injected dose and blood content.


Tommaso Novellino

2.2.3 Main results and discussion

2.2.3.1 *In lab* study

Preliminary IFN stability test

Standard curves prepared using PBS or Diluent C as solvent showed measured-concentrations lower than nominal-ones. Using Diluent C as solvent, smaller difference and better correlation between nominal and measured data was found. Both stability tests showed that IFN variability at 37°C for over a month is much lower than the difference between measured and nominal concentration.

The results of the low-concentration IFN stability test are shown in **Figure 2.2.3**. They present variation between all the measurements <30% and a good linear relationship ($R = 0.99$) between nominal and average measured concentrations.

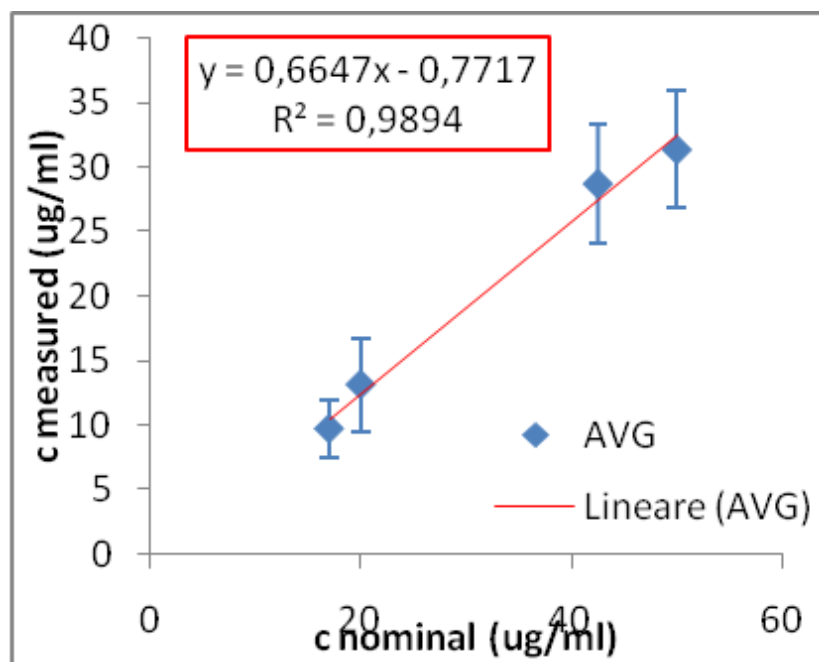
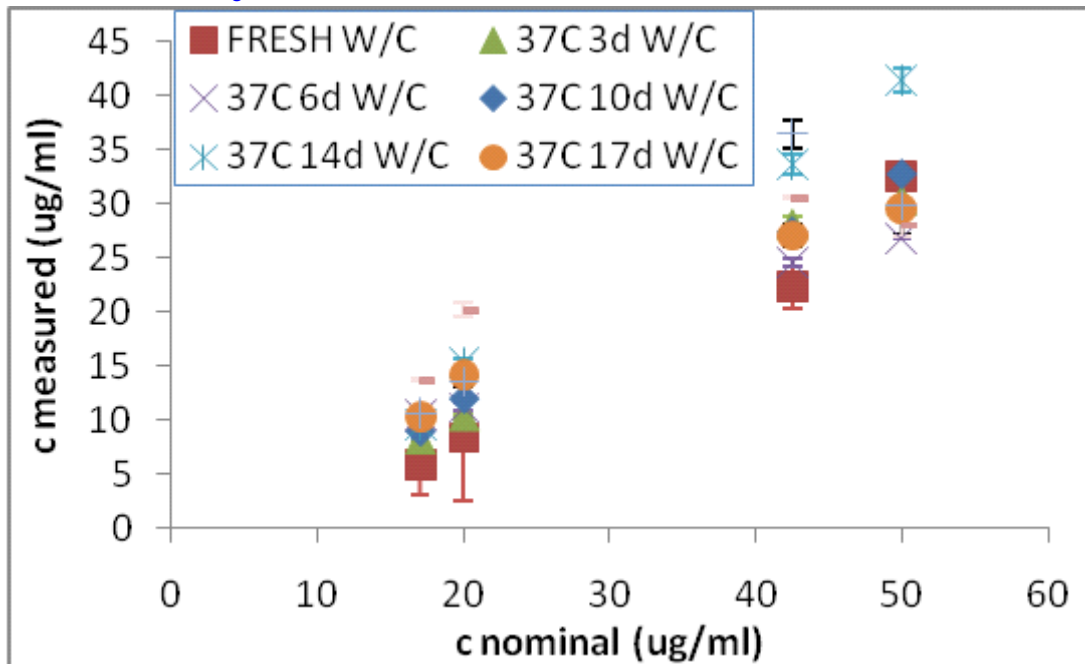


Figure 2.2.3 IFN stability-test results at low concentration.

The results of the high-concentration IFN stability test are presented in **Figure 2.2.4**, and their variability is <20%. As reported in the literature, IFN is more stable at higher concentration.

Tommaso Novellino
 49

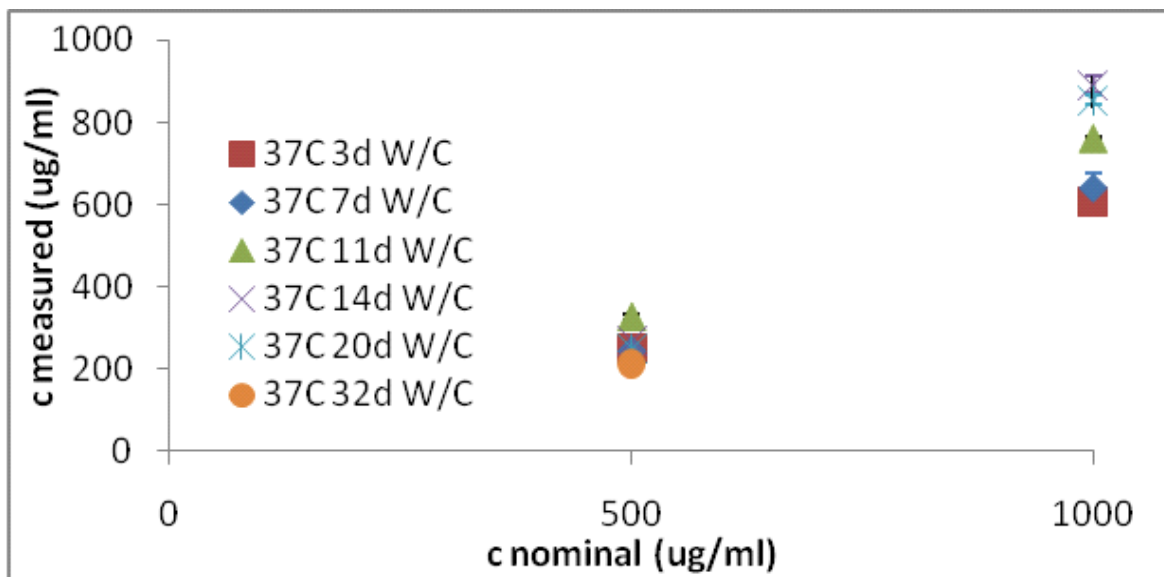


Figure 2.2.4 IFN stability-test results at high concentration.

According to these data, the reservoir solution is stable enough even at body temperature for the intended experiment duration (1 month).

IFN release from nDS configuration 20x2 (PBS solution)

Figure 2.2.5 shows cumulative releases of IFN from 20x2 nDS membranes.

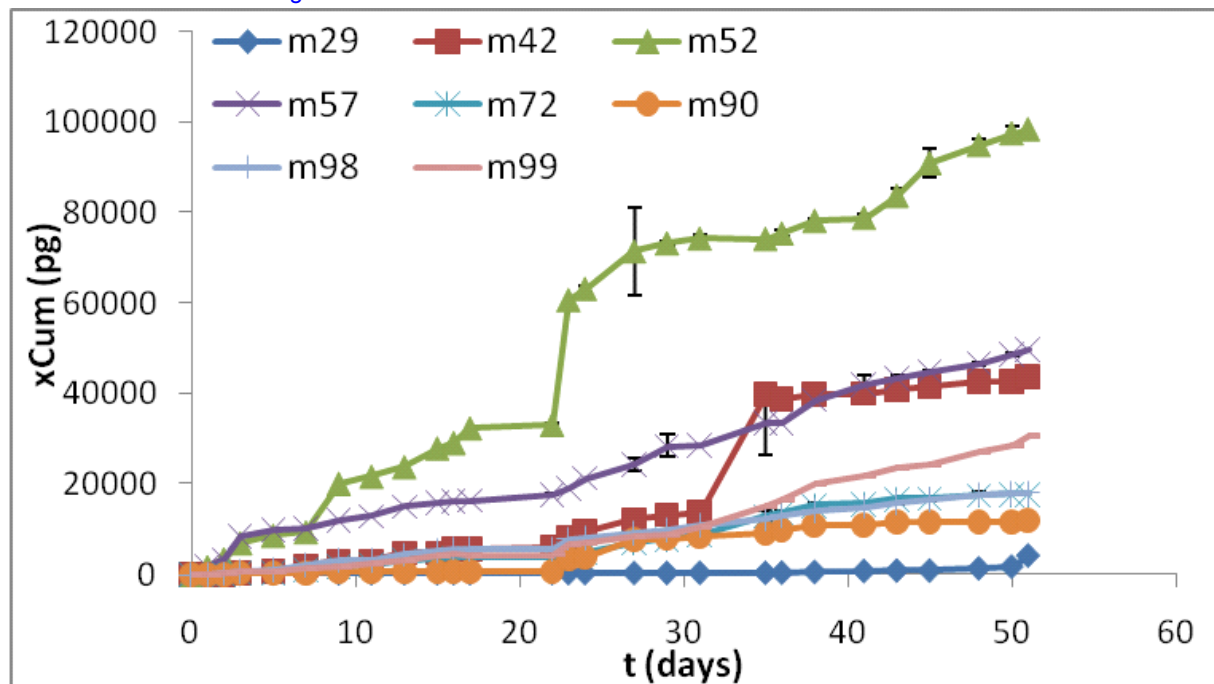


Figure 2.2.5 Cumulative IFN release from nDS of configuration 20x2 ($n = 8$).

Data show a very high variability among the different membranes in terms of IFN release. The spread between the replicates is probably due to fabrication issues, but it is stressed even more by the use of PBS as solvent, that was shown to reduce IFN detectability and accuracy of ELISA kit measurements compared to Diluent C.

IFN release from nDS configuration 20x3 (Diluent C)

The cumulative mass (X_{cum}) of IFN released over time (4 months) from 20x3 nDS membranes are individually shown in **Figure 2.2.6**.

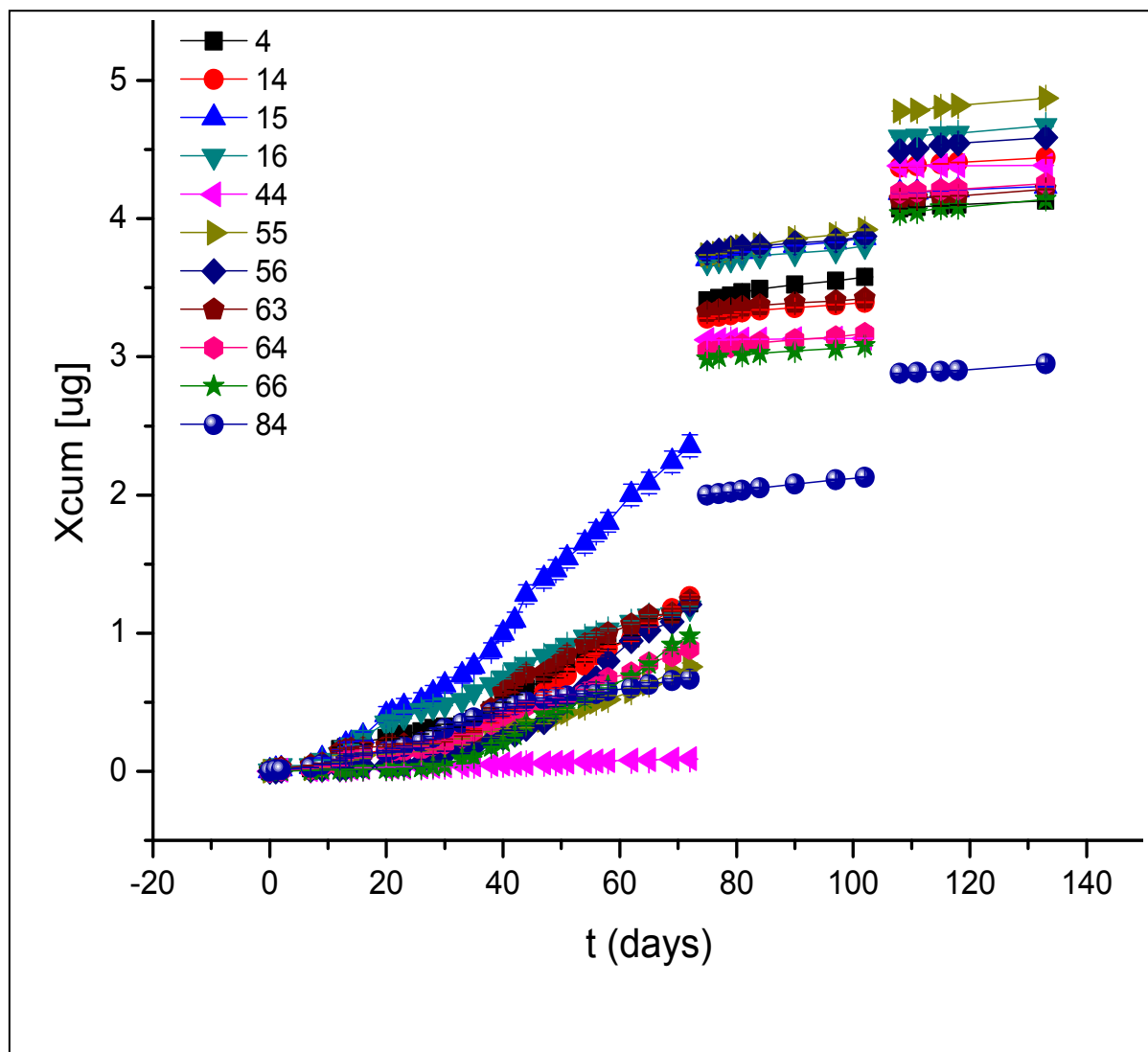


Figure 2.2.6 Cumulative release of IFN from nDS configuration 20x3, for each different membrane (indicated by an ID#).

The average of the data shown in **Figure 2.2.6** is presented in **Figure 2.2.7**, where some outliers were removed.

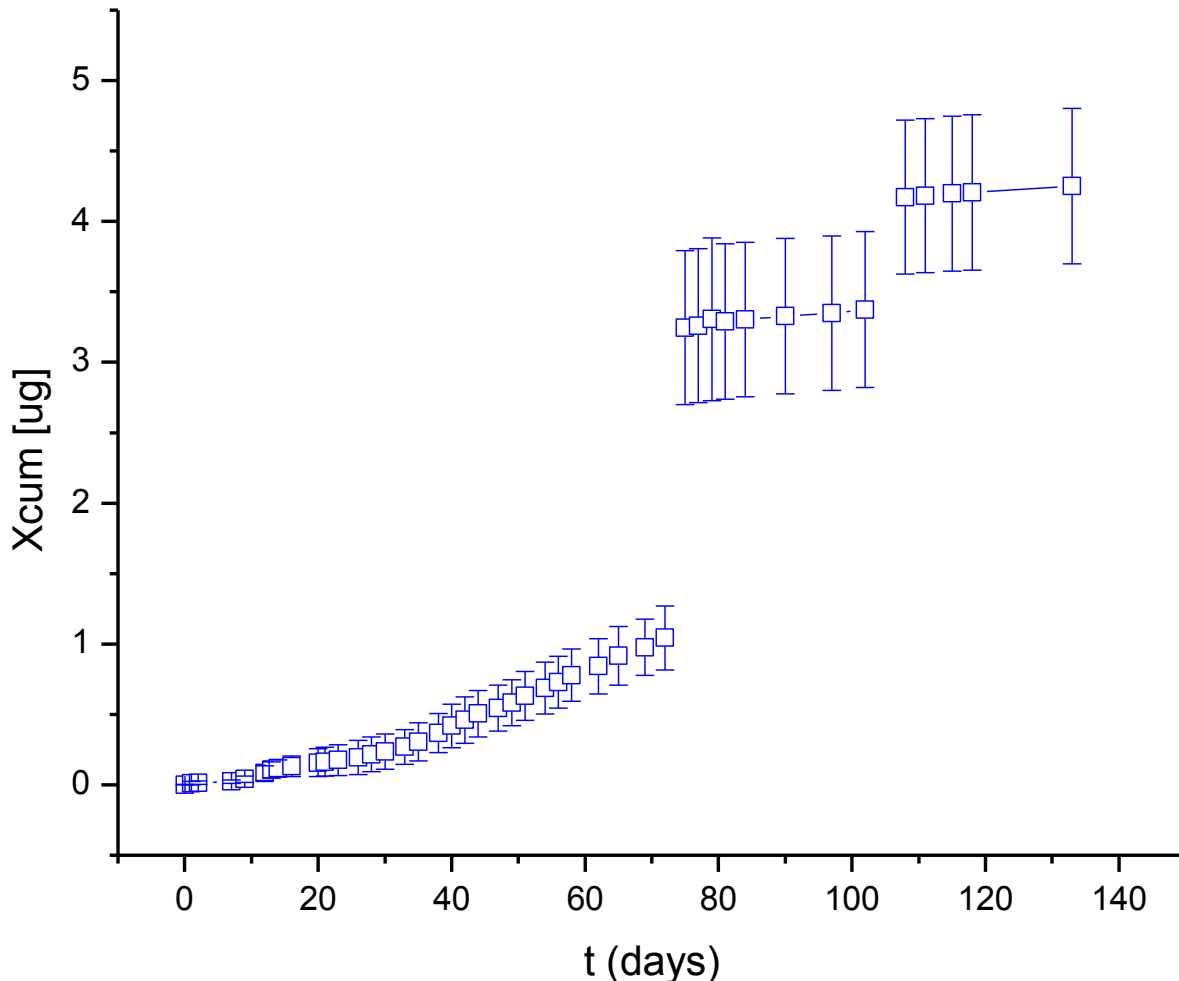


Figure 2.2.7 Cumulative release of IFN from nDS configuration 20x3, averaging all the membranes in **Figure 2.2.6** ('84' and '15' excluded).

The releases from the different membranes are quite similar, and the average shows a not large standard-deviation. A nice constant-release (14 ng/day) was observed until reservoir-solution was diluted the first time (day 72th). Linear fitting confidence improves significantly when removing first-week measurements, which are very low. After dilution of reservoir solution at day 72th and 102th, data showed constant-release but with different release-rates (4 ng/day and 3 ng/d, respectively). The estimate released percent is 15% at day 72th, 55% at day 102th and 70% at day 133th. Even if these values are slightly underestimated due to the observed inaccuracy of detection method (ELISA kit), the change of release rate in this experiment reveals a fickian release. The non-constrained diffusion may also be due to

the solvent used (Diluent C) that is more viscous than water and slows down the diffusion of IFN molecules.

Concentration and volume of all reservoirs measured during 1st and 2nd dilutions and at the end of the experiment are shown in **Table 2.2.5**; data variability is between 10÷30%. A remarkable reduction in the volume (compared to the initial 300μl) can be observed, probably due to evaporation.

Membrane ID#	Before 1 st dilution			Before 2 nd dilution			At the end		
	c (μg/ml)	SD	V (μl)	c (μg/ml)	SD	V (μl)	c (μg/ml)	SD	V (μl)
4	17.9	0.7	180	3.2	0.1	180	2.4	0.1	180
14	15.7	0.1	190	6.4	0.2	190	3.5	0.1	190
15	11.6	1.2	170	2.1	0.01	170	1.3	0.1	170
16	18.2	0.05	205	5.1	0.1	205	3.2	0.004	205
44	20.7	0.6	220	8.3	0.2	220	4.7	0.01	220
55	20.2	0.3	220	5.6	0.4	220	3.4	0.1	220
56	17.6	0.4	215	4.0	0.0	215	2.1	0.1	215
63	17.1	0.6	180	4.7	0.1	180	3.5	0.1	180
64	17.3	0.4	185	6.7	0.1	185	3.2	0.1	185
66	15.7	0.2	190	6.3	0.3	190	2.6	0.04	190
84	15.3	0.1	130	4.9	0.03	130	2.5	0.2	130

Table 2.2.5 Measured concentration and volume of reservoir solutions.

2.2.3.2 *In vivo* study

IFN titration in blood

IFN detection in blood using the ELISA kit specific for *in vivo* measurements resulted less effective than in aqueous solution, as in **Figure 2.2.8**.

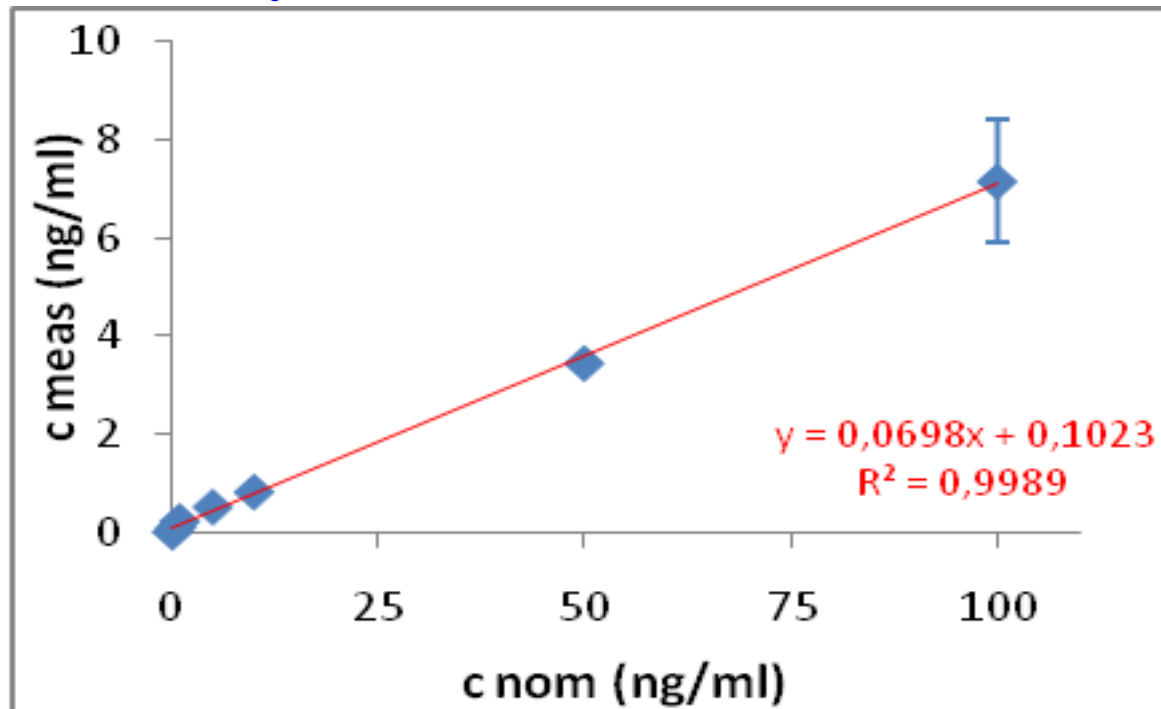


Figure 2.2.8 Average of measurements of IFN content in blood from different rats.

Legend: 'c nom', nominal (known) concentration; 'c meas', measured (by ELISA) concentration.

The concentration measured in serum was always much lower than the nominal one, probably due to proteases and other factors present in the serum (*serum effect*). Measurements showed no differences among different rats (standard deviation smaller than 15%).

Animal response to implant

Implant surgery procedure was simple and rats looked fine since right after waking up from anesthesia. One week after implantation, the hair was already grown and stitches were removed. Some of the capsules stayed in place and others moved under the skin to reach leg or closer to abdominal region.

Rats were fine during the whole experiment and nicely supported also blood drawing twice a week; but rat #23 (group ID# 2, rat ID# 3) after 2÷3 weeks exhibited a swelling in the capsule region, probably due to an immune reaction. The probable cause of this problem was an individual sensitivity of the rat, because all the other 4 rats were fine and all the 5 capsules

Tommaso Novellino
55

were treated through the same procedure. The rat was treated with antibiotic, which didn't interfere with the experiment, and healed for a week. After another week (6/22/09), few days before the end of the experiment, the implant was totally rejected, the rat had to be sacrificed and the capsule removed.

The other capsules were removed after 31 days, on June 30th 2009.

Images taken during explants procedure are shown in **Figure 2.2.9**.

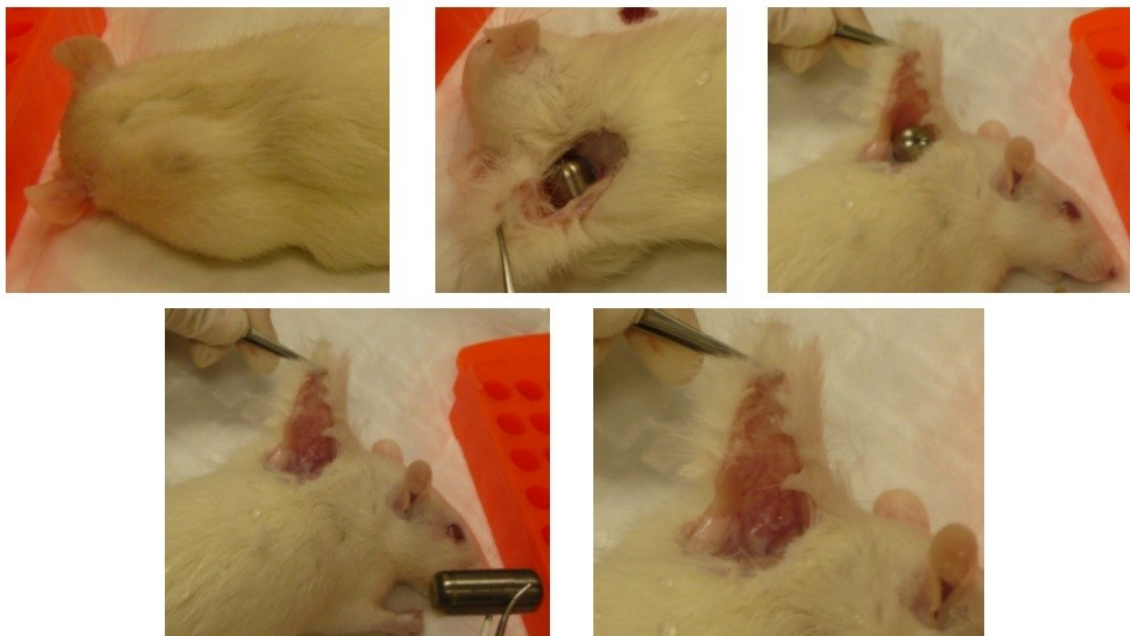


Figure 2.2.9 Photographs of capsule explantation (from rat #21).

IFN release

IFN content in the blood was measured with ELISA kit from rat serum.

All rats belonging to groups 1 and 4 (no IFN controls) showed negligible amount of IFN in their blood, as expected. Measures referred to rats of these groups were always below kit sensitivity (data not shown).

IFN detected in rats of group 3 nicely correlate with IFN amount injected (**Figure 2.2.10**).

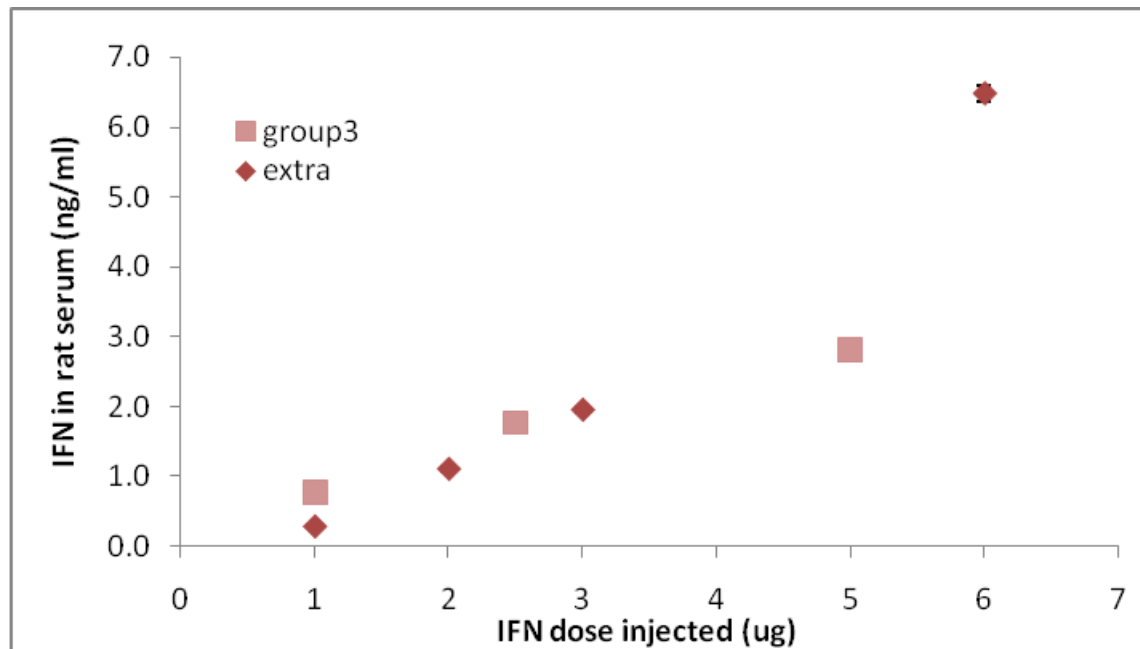


Figure 2.2.10 IFN measurements in rats of group 3 versus injected amount IFN.

Four days after injection, IFN presence in the blood was not detectable (measurements below detection-limit of the kit). All rats of group 3 showed complete IFN-clearance from their blood after 3÷4 days for all doses, in accordance with IFN pharmacokinetic data reported in the literature [Badkar *et al* 2007].

Among rats of group 2, with IFN-capsule implanted, only one rat (#21) showed a significant release, as shown in **Figure 2.2.11**. The other 2 rats of group 2 did not show a significant release (data not shown).

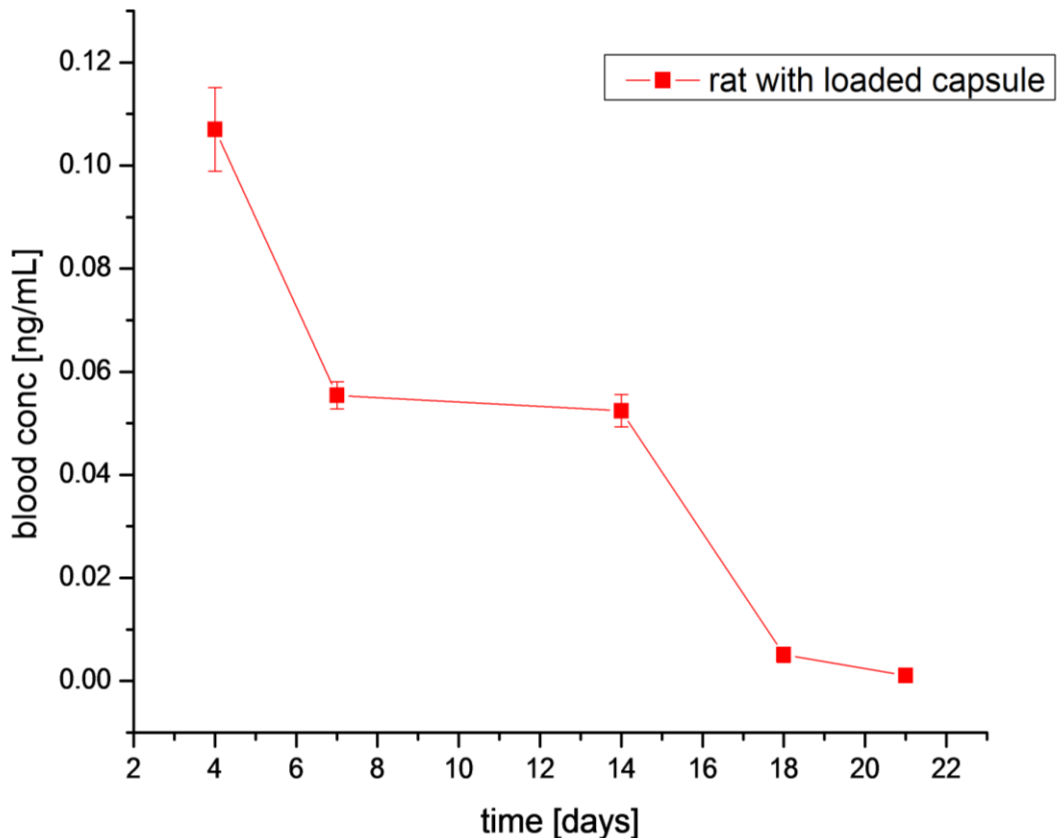


Figure 2.2.11 IFN detected in serum of rat #21.

IFN content in rat #21 decreases during the first week, then it stays constant for about 10 days and after that it becomes very low, close to detection limit. This result is promising, since the constant IFN level in the blood may be due to a constant release from the capsule. Further experiments would be required to assess if this is the actual case.

Capsules after explantation

Explanted capsules were analyzed, and concentration (c) and volume (V) of their content were measured, as reported in **Table 2.2.6**.

Capsule from rat ID	c ($\mu\text{g}/\text{ml}$)	V (μl)	Solution color
#21	18.6 ± 0.01	300	clear
#22	27.6 ± 0.8	170	clear
#23	53.1 ± 0.3	630	clear
#41	not detectable	1000	red
#42	not detectable	950	red

Table 2.2.6 Properties of solution found in the capsules after explantation.

Concentrations of group 2 are much lower than the initial one (0.9mg/ml), while IFN presence in group 4 are negligible, as expected.

IFN-containing capsules (group 2) showed large volume variability, always much lower than starting value (1÷1.2 ml). Solutions from capsules of group 4 had a larger volume and were more red-colored (**Table 2.2.6**).

The red color was probably due to the presence of few blood cells in the capsule, but since blood cells are too big to pass through the nanochannels then nDS membranes of this group may be broken; this could be occurred during the loading procedure, that in these capsules requested to break into the bottom hole which was sealed by extra glue. Another possibility is that it is correlated to the presence of fibrotic tissue around the capsules (**Table 2.2.7** and **Figure 2.2.12**).

Capsule from rat	tissue-encapsulation	Top cap – nDS membrane condition
#21	clean – no tissue formation	3 holes almost closed and 2 partially closed – nDS with few tissue
#22	clean – no tissue formation	4 holes closed and 1 half closed – nDS with few tissue
#23	completely encapsulated – after swelling totally rejected	2 holes closed – nDS covered of tissue
#41 (control)	almost totally encapsulated by fibrotic tissue	1 hole closed and 1 half closed – nDS with tissue
#42 (control)	almost totally encapsulated by fibrotic tissue	3 holes partially closed – nDS with a lot of tissue

Table 2.2.7 Explanted-capsules condition.



Figure 2.2.12 Capsule explanted from rat #41 with fibrotic tissue.

Capsules of group 4 were both partially covered by thin fibrotic-tissue as shown in **Figure 2.2.12**, while capsule from group 2 (rats #21 and #22) were clean. The capsule in titanium seemed to be more biocompatible and to induce less fibrotic-tissue formation.

Capsule cap facing nDS membrane (top) presented some holes occluded by fibrous material. Some representative pictures of occlusions are shown in **Figure 2.2.13**.

Tommaso Novellino
60

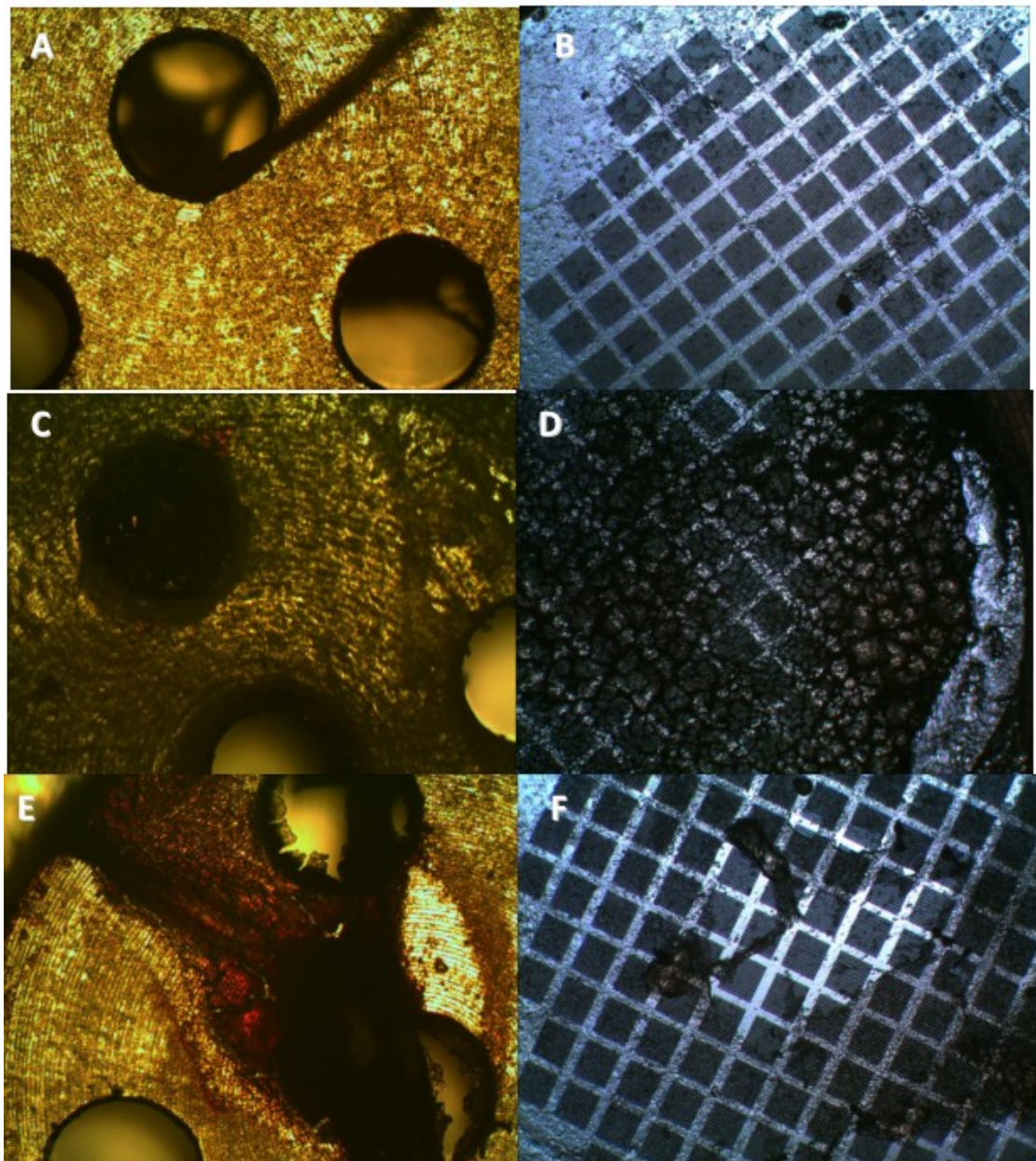


Figure 2.2.13 Pictures (microscope with objective 4x) of the titanium top-cap holes (**A, C, E**) and nDS membranes (**B, D, F**) of capsule explanted from rat #21 (**A and B**), #23 (**C and D**) and #42 (**E and F**).

Figure 2.2.13 shows the massive tissue formation in the holes and on the membranes of rat #23 that rejected the implant, and minor encapsulation of cap and membranes from rats #21 and #42. The amount of tissue in the holes and on the membranes nicely correlates with tissue encapsulation of the capsules.

Tommaso Novellino
61

Histological analysis

Tissues harvested from next to the capsule (wound) and far from it (normal) have been stained with Myeloperoxidase and Hematoxylin & Eosin. No evidence of inflammatory response in the normal tissue and the wounded one was observed in all the rats, except for the rat #23 that rejected the capsule.

Image of harvested tissue from rat #23 are shown in **Figure 2.2.14**.

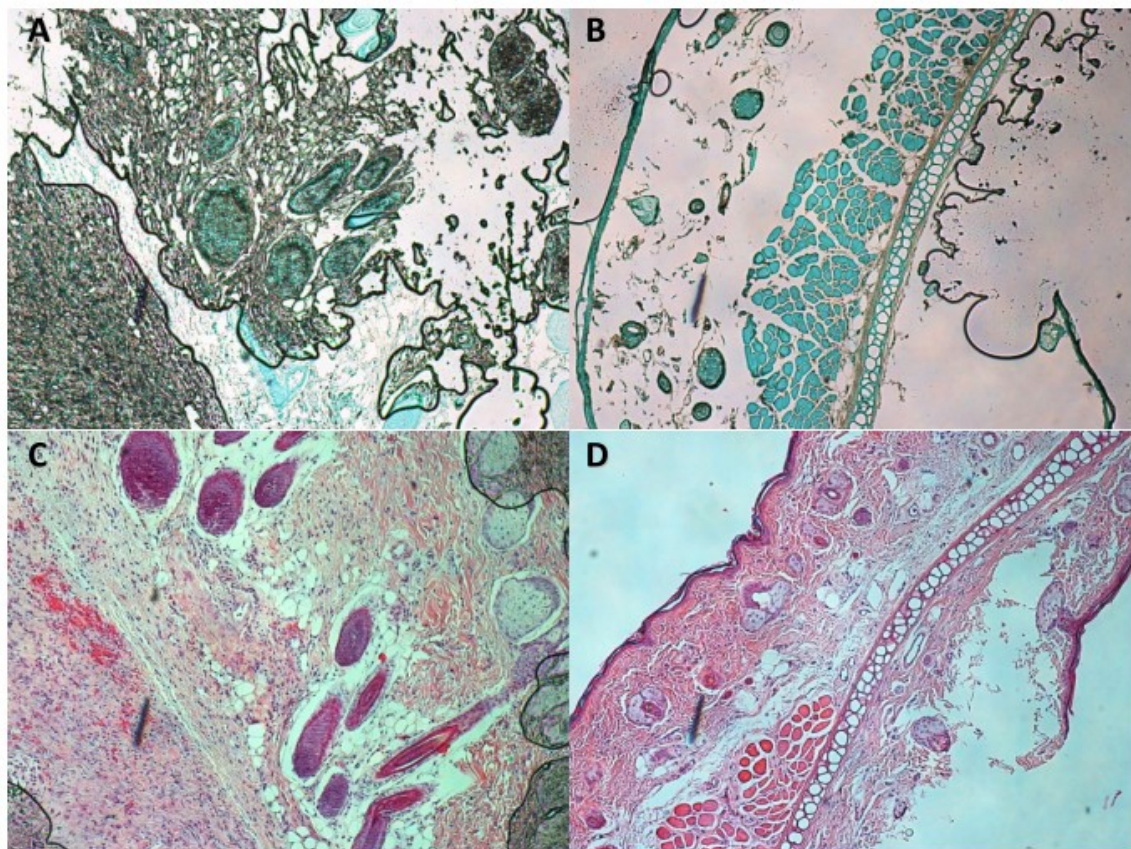


Figure 2.2.14 Myeloperoxidase (**A, B**) and Hematoxylin and Eosin (**C, D**) stained tissues (microscope with objective 10x) from rat #23 harvested next to the capsule (**A, C**) and far from it (**B, D**).

Images related to rat #23 in **Figure 2.2.14** show high inflammation of the tissue next to the capsule, while tissue taken far from it looks fine.

Sample images of normal (far from the capsule) and wounded (next to the capsule) tissue from the other rats are shown in **Figure 2.2.15**.

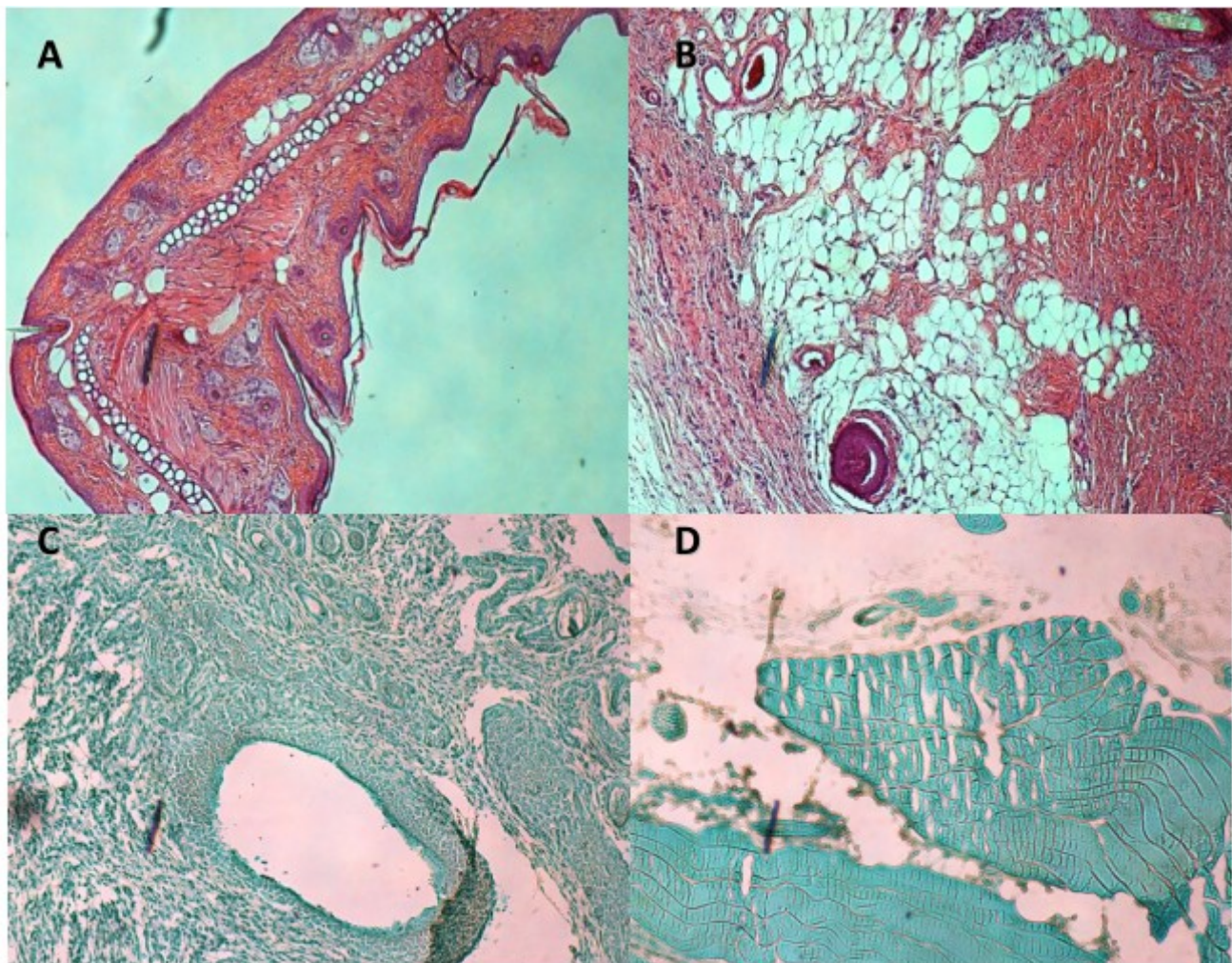


Figure 2.2.15 Hematoxylin and Eosin (**A, B**) and Myeloperoxidase (**C, D**) stained tissues (microscope with objective 10x) of rat #21 and #22, respectively, harvested next to the capsule (**A, C**) and far from it (**B, D**).

Images of **Figure 2.2.15** show no evidence of inflammation or abnormalities for both types of tissue and both animals.

2.2.4 Conclusions

In lab study of IFN release through nDS membranes showed that ELISA kit measurements of IFN concentration are strongly dependent on dilution ratio in a non-linear way and it was not possible to detect the actual concentration. Data are usually underestimated and released percent cannot be precisely quantified. Preliminary results using 20nm-height nanochannel and a 20 μ g/ml reservoir solution in Diluent C showed that IFN release is fickian and the variability among the different membranes is not large. It is worth noting that during this experiment the measured release-rate was constantly equal to 14 ng/day for more than 70 days, and hence it was anyway achieved a long-term constant-release from nDS.

In vivo preliminary study performed on 10 rats showed that animals nicely tolerate the implant. Implantation and explantation surgery were quite simple and rats recovered immediately after capsule implantation. Capsules tissue encapsulation differs from animal to animal; the presence of tissue around the capsule probably depends on animal sensitivity and capsule handling during loading procedure. The concentration used for the release *in vivo* is high enough to detect IFN presence in the blood. Not all the implanted capsules loaded with IFN ($n = 3$) released drug, only one rat showed constant IFN level in the body for about 10 days, but further study would be required to quantify IFN release *in vivo*. The study of IFN presence in rat blood after subcutaneous injections may drive to an estimate of the actual amount of IFN released *in vivo* from nDS.

Another *in lab* study with the same nDS membranes and reservoir concentration as the present *in vivo* experiment would be required in order to find *in vivo – in lab* correlation.

2.2.5 Acknowledgements of Section 2.2

- Experiments were planned and designed by Tommaso Novellino and Enrica De Rosa;
- Animal protocol was written by Enrica De Rosa and April Ewing;
- Stability-test was performed by Tommaso Novellino;
- *In-vivo* capsules were fabricated and assembled by *NanoMedical Systems*;
- *In-lab* testing-devices were assembled by Tommaso Novellino and Enrica De Rosa;
- Animals (surgery, drawing, injection) were handled by April Ewing, Melissa Vetter and Qing-po Li;
- Concentration measurements (ELISA) were executed by Tommaso Novellino, Erika Zabre and Dino Nguyen;
- Data analysis was performed by Tommaso Novellino;
- Results interpretation and discussion was done by Tommaso Novellino and Enrica De Rosa.

2.3 Release of probe from nanochanneled devices in laboratory condition

In order to estimate the actual release profile of some nDS membranes with a molecular probe (dextran), particularly to check if it was linear, the following diffusion experiment has been performed.

2.3.1 Experimental methods

The membranes to test were selected again according to optical observation (no defects, clear outlets-opening and nice overall appearance) and gas testing. 16 membranes, of configurations 20x2 ($n = 11$) and 20x3 ($n = 5$) which were anyway shown to behave very similarly, were selected and used.

Experiment started on 1/27/2009, and lasted about 2 months.

Test preparation

Commercial fluorescently-labeled 10kDa dextran (*Molecular Probes*), conjugated with fluorescein isothiocyanate (FITC), was used to prepare two solutions with pH 7.2 Phosphate-Buffered Saline (PBS, *GIBCO*): 5mg/ml, used for diffusion test as reservoir solution; and 0.1mg/ml, used for the standard curve as calibration system. The standard curve was obtained serially-diluting (ratio 1:2) the 0.1mg/ml solution, putting 100 μ l/well in duplicates, in a 96 wells μ -plate (*Greiner*); pure PBS was used as blank. The same standard curve was used all over the experiment; its stability was monitored over the 2 months.

The chosen membranes were assembled in the specifically-designed cylindrical testing devices: o-rings were placed in the grooves of two stainless-steel bodies, screws were put in one body, then one selected nDS1 membrane was inserted in its outer groove (gently chopping membrane corners in case of non fitting), finally bodies were joined screwing in the nuts.

After assembling the testing devices, the following wetting procedure was performed on the membranes, to assure uniform and complete capillary-filling of liquid inside them. The Si sides of the membranes were filled with ethanol (400 μ l) and a check of air-bubbles was performed with optical microscope. Bubbles eventually present (especially inside the macro-channels) were removed by cap-pressuring or by pipetting, in order to avoid hinder in the wetting and diffusion. After waiting 15min, to not have bubbles trapped inside the membrane, a cap (silicon rubber) was placed, and the Pyrex side was then filled with ethanol and capped. Ethanol was left both sides overnight. The Si sides were then partially dried –leaving a liquid veil to prevent un-wetting inside the membrane by evaporation– and checked again for bubbles, then filled immediately with de-ionized water (400 μ l) and capped; the same was

done for the Pyrex sides. After 1h, both sides were dried (always partially) and de-ionized water was inserted: this was repeated 4 more times, to completely remove ethanol from inside the membranes. Finally, both sides were washed 2 times using the test solvent (PBS).

After wetting, the Si sides were totally dried, and 300 μ l of the 5mg/ml dextran solution were inserted promptly (always to prevent evaporation of the internal liquid). The reservoir chamber was then capped inserting a needle in the center of the cap (to avoid overpressuring and to facilitate eventual liquid-spilling); the cap was then sealed with Gasket tape (chemically-inert and sealant) to limit liquid loss. After Si side filling and capping, the sink chamber was first washed with the solvent, to remove eventual dextran solution passed through the membrane during the last step; then, 250 μ l of PBS plus a stainless-steel sphere (to improve mixing) were inserted in it, which was then capped always with needle.

Testing procedure

The testing devices were stored at room temperature and placed on a rotator. The measurements were performed daily during the first week than every 2÷3 days for the following two weeks. Two 100 μ l samples were collected from the sink chamber of each device and replaced with 200 μ l of PBS. The standard curve was incubated at 25°C.

All the collected samples were placed in 96-wells μ -plate and measured by a spectrophotometer (*BMG Labtech*), using reading-settings shown in **Table 2.3.1**.

Parameter	Utilized
Modality	Fluorescence
Type	End-point
Excitation wavelength	485 nm
Emission wavelength	520 nm
Gain	735

Table 2.3.1 Spectrophotometer settings used in the concentration measurements.

Data Analysis

Spectrophotometrically-obtained fluorescence data were converted, through the standard curve ($F = 626722 \cdot c + 733.4$), in concentrations. From the latter, dextran released masses were derived, introducing the sink volume (250 μ l) and correcting the PBS replacing:

$$x(t_i) = c(t_i) * V_{sink} - x(t_{i-1}) * V_{left}/V_{sink} \quad (\text{Equation 2.3.1})$$

The daily-released masses were then summed, to obtain the cumulative release profile:

$$x_{tot}(t_i) = x_1 + x_2 + \dots + x_i \quad (\text{Equation 2.3.2})$$

2.3.2 Main results and discussion

The standard-curve stability results are shown in **Figure 2.3.1**, which demonstrates its stability over the period assessed (2 months).

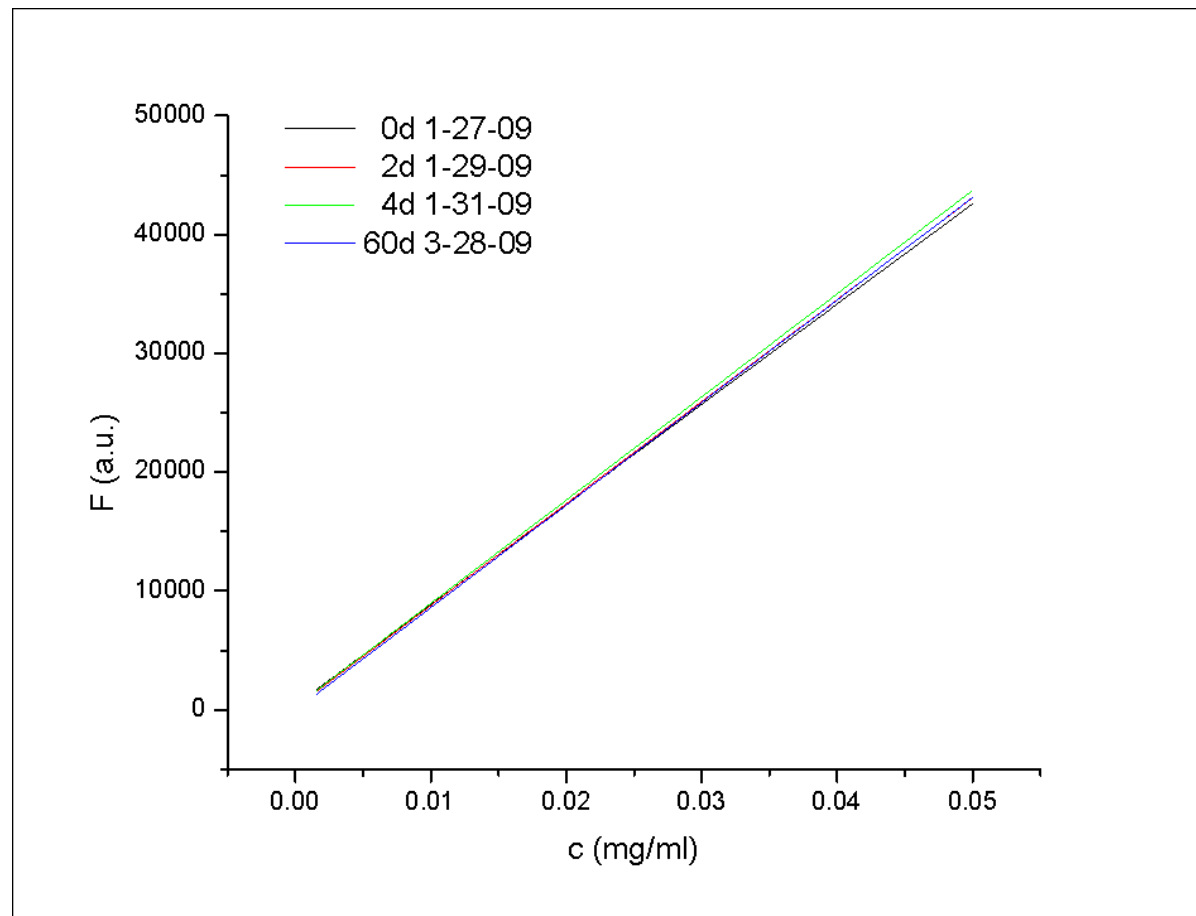


Figure 2.3.1 Standard curve fluorescence stability over time.

The measured release results of the experiment are shown in **Figure 2.3.2-5**.

Figure 2.3.2 shows the individual results for the configuration 20x2; an outlier (ID# 'VII49') can be observed.

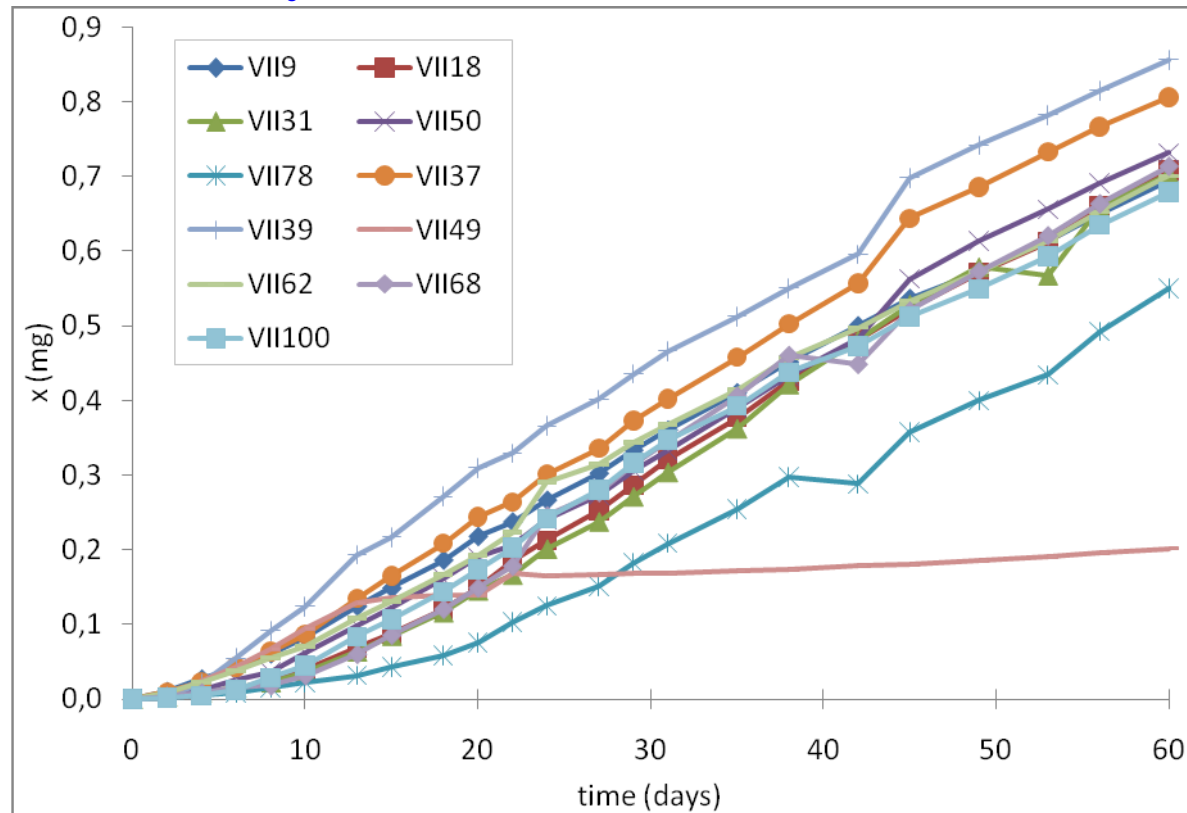


Figure 2.3.2 Individual mass-cumulative release of membranes with configuration 20x2.

Figure 2.3.3 shows the individual results for the configuration 20x3.

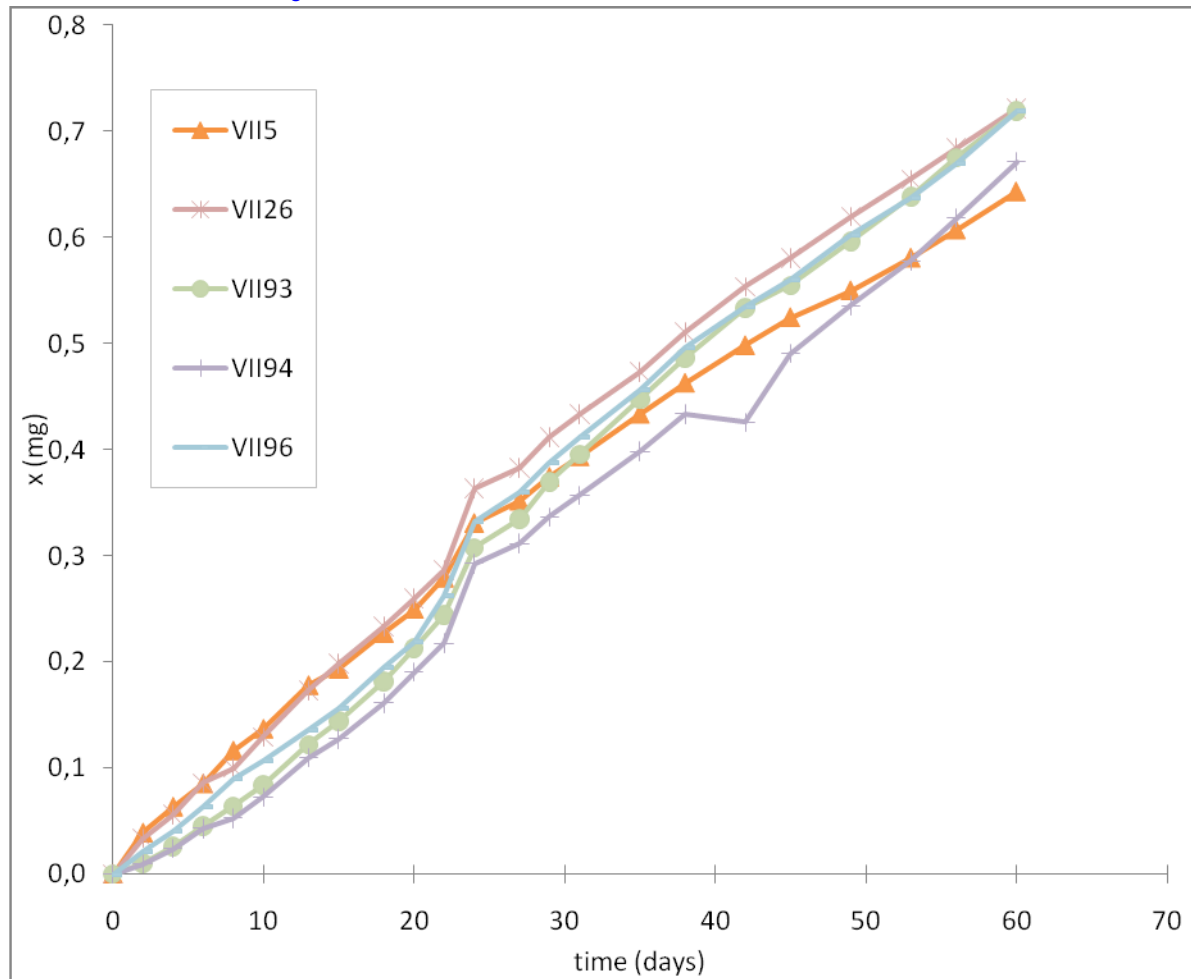


Figure 2.3.3 Individual mass-cumulative release of membranes with configuration 20x3.

Figure 2.3.4 shows the individual results for both the configurations 20x2 and 20x3: their release behavior is clearly undistinguishable, so they could be averaged together, giving data shown in **Figure 2.3.5**.

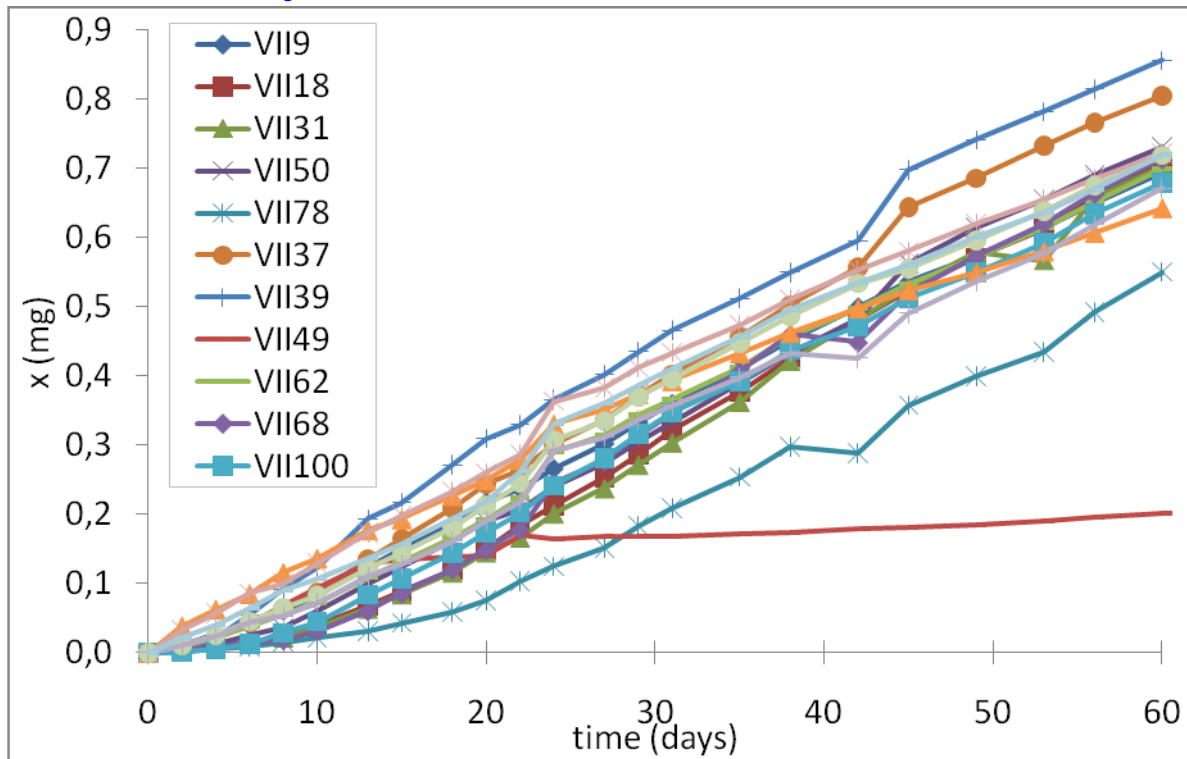


Figure 2.3.4 Individual mass-cumulative release of membranes with both configurations 20x2 and 20x3.

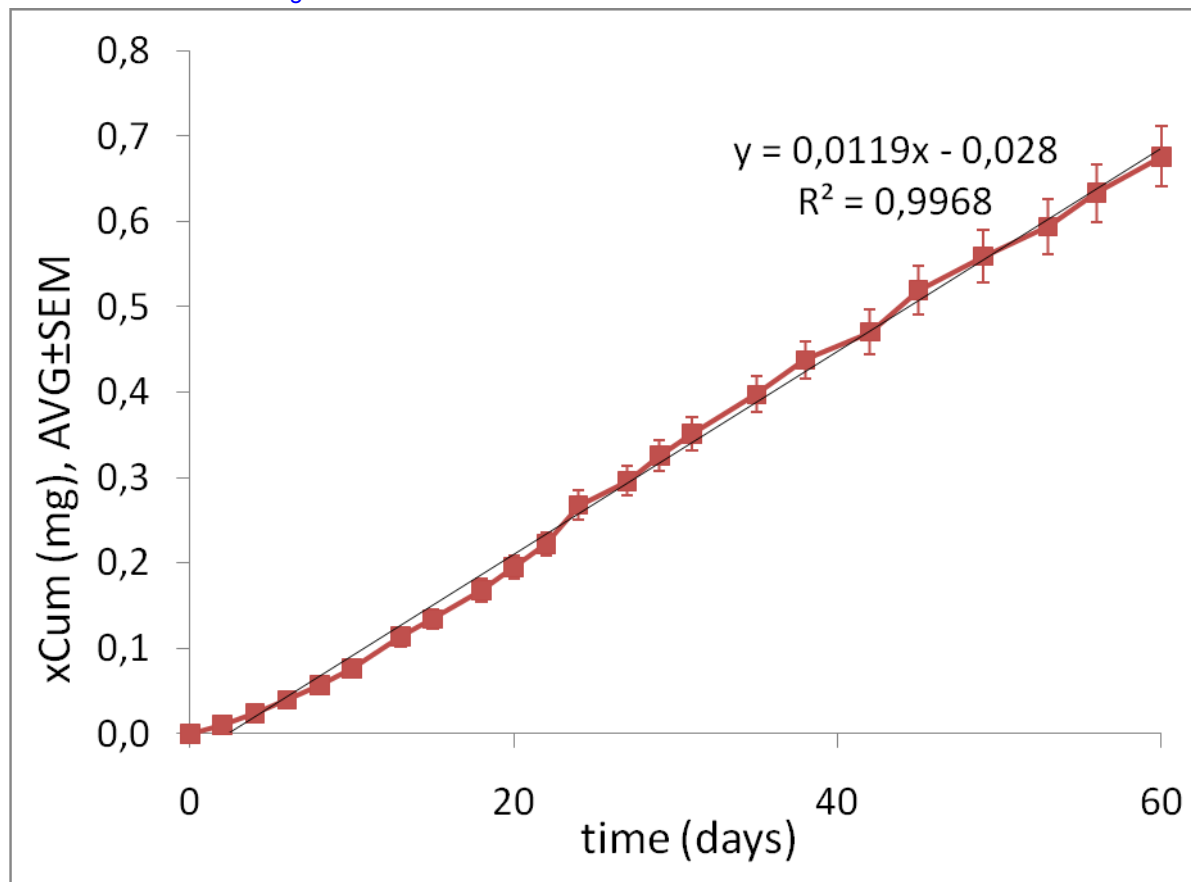


Figure 2.3.5 Experimental average cumulative-release.

Results are presented as mean \pm SEM.

Figure 2.3.5 demonstrate that, for the membrane configurations utilized and the dextran molecular-weight chosen, the mass release is linear over a long period of time (2 months).

2.3.3 Personal contribution

My contribution to the research presented here has been mainly related to the diffusion test-preparation, concentration measurement, data analysis and interpretation of the results.

2.4 Acknowledgements

I acknowledge Enrica De Rosa for her guidance and work in both the IFN and dextran experiments, including experimental preparation and data analysis; Alessandro Grattoni for project guidance, membranes design, gas-system and testing-devices development, 3D images and schematics; Erika Zabre and Dino Nguyen for membrane characterization; Daniel Fine and Xuewu Liu for membrane design and fabrication; *NanoMedical Systems, Inc* for membrane and capsule fabrication; Mauro Ferrari as principal investigator, advisor and project director.



A handwritten signature in black ink, appearing to read "Tommaso Novellino".

3 The endothelial barrier and cell cytoskeleton

3.1 Rationale of the study

The vasculature, the body delivery system, can be both probed *in-vitro* by nanotechnology (AFM) and used to delivery nanotechnological-agents (*vascular targeting*, where nanoparticles are conjugated with moieties specific for endothelial cell membrane receptors).

The endothelial layer, lining all the blood vessels (arteries, veins, capillaries), acts as a barrier regulating the substance exchange between the blood compartment and the extravascular region; sometimes it protects the latter from the entry of dangerous chemicals or micro-organisms, while sometimes –as, for e.g., during an inflammation– it allows the transport of endogenous cells into the latter. The endothelium integrity is important both in patho-physiological processes as the inflammation, where it becomes more permeable (in order, for e.g., to permit the immune-cells diapedesis), and also in systemically-injected nanoparticles, which may interact with the endothelial mono-layer.

Two studies are presented here. Both are *in-vitro* works with live human vascular endothelial cells (ECs), which were probed by a micro-particle (5 μ m-diameter silica sphere) attached as tip of an atomic force microscope (AFM), a recent but already-established tool in biology as well as many other fields.

In the first study, cells were incubated with Tumor Necrosis Factor-alpha (TNF- α), a known pro-inflammatory cytokine, in order to evaluate possible effects in their mechanical properties (cell Young's modulus and non-specific, visco-elastic adhesion) and cytoskeletal structure. Blood vessel endothelial cells inflammation by TNF- α was induced in order to better understand its functioning and to characterize it *in-vitro* with a fast and agile methodology (AFM); this is, to the best of our knowledge, the first study analyzing the effect of pro-inflammatory cytokines on three different EC types and demonstrating that the response to TNF- α stimulation is independent of the vascular district.

In the second study, the possible dependence of ECs mechanics (stiffness) and cytoskeleton upon the incubation with gold nanoparticles was assessed. Two particle sizes (30

and 100 nm) and four different incubation-concentrations (0, 0.1, 0.2, 0.5 mg/ml) were used, in order to see the possible dependence of the cellular response on those experimental parameters.

The obtained results aimed to add a contribution towards the comprehension of the bio-physical mechanisms governing the cells and their functions, both in patho-physiological cases (inflammation) and when systemically-, intravenously-injecting nanoparticles inside the bloodstream (gold colloid).

3.2 Endothelial cells and cell cytoskeleton

3.2.1 Endothelial structure and functions

The endothelium is a tissue (a specialized type of epithelium tissue, more specifically a simple squamous epithelium) formed by a single-layer of endothelial cells (ECs mono-layer). It lines the blood vessels (**Figure 3.2.1**): the endothelial cells form a thin layer lining their interior surface, forming an interface between circulating blood in the lumen and the rest of the vessel wall as well as the extravascular space.

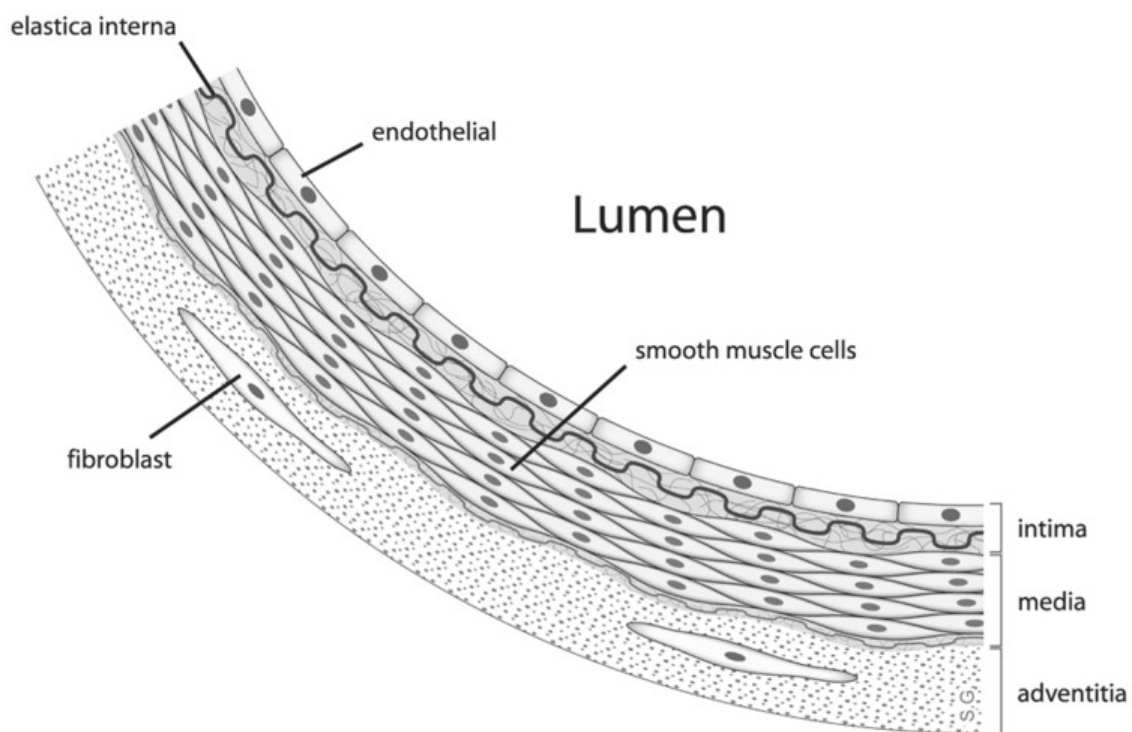


Figure 3.2.1 Diagram showing the location of endothelial cells [[Wikipedia](#)].

It presents: the lumen (where the blood flows) and the three tunicas (intima, media,

adventitia) constituting the vessel wall. The ECs constitute the tunica intima.

Endothelial cells are involved in many aspects of vascular biology, both physiological and pathological.

Physiology

Endothelial cells line the entire circulatory system, from the heart to the smallest capillary. Endothelium lining the interior surfaces of the heart chambers is called endocardium. Both blood and lymphatic capillaries are lined by the endothelial mono-layer. ECs reduce turbulence of the blood flow, allowing the fluid to be pumped farther.

The endothelium acts as a selective barrier between the vessel lumen and the surrounding tissue, controlling the passage of materials and white blood cells into and out of the bloodstream; it also plays a role in the formation of new blood vessels (angiogenesis), in vaso-constriction and vaso-dilation (blood-pressure control) and in blood clotting.

Pathology

Endothelium-related pathological conditions are atherosclerosis and inflammation.

Endothelial dysfunction –the loss of proper endothelial function– is a hallmark for vascular diseases, and is often regarded as a key early event in the development of atherosclerosis. Endothelial dysfunction has also been shown to be predictive of future adverse cardiovascular events. The most prevailing mechanism of endothelial dysfunction is an increase in reactive oxygen species, which can impair nitric oxide production and activity via several mechanisms [Deanfield *et al* 2005]; nitric-oxide reduction is one of the main mechanisms for endothelial dysfunction.

In certain cases, as during chronic inflammation, an excessive or prolonged increase in permeability (hyper-permeability) of the endothelial monolayer may happen.

3.2.2 Cytoskeleton structure and functions

The cytoskeleton is an intra-cellular structure, whose basic function is to both provide structure to the cell itself and intra-cellularly transport molecules of interest.

It is present in all cells (in eukaryotic –**Figure 3.2.2**– as well as in prokaryotic cells), is contained within the cytoplasm and is made out of proteins; it has structures such as flagella, cilia and lamellipodia. It plays important roles in both intracellular transport (the movement of vesicles and organelles, for example) and cellular division. It has been described as a ‘protein mosaic’ that dynamically-coordinates the cytoplasmic biochemistry [Peters 1929].

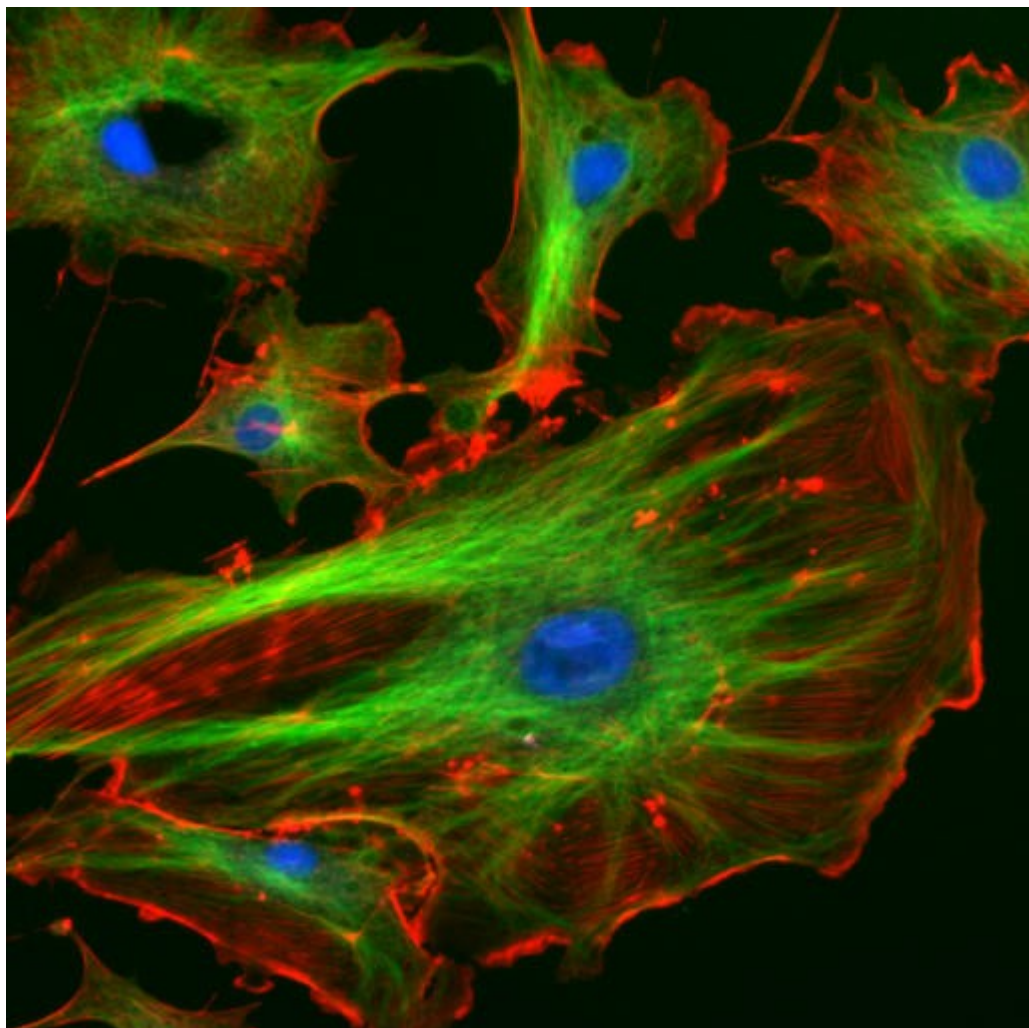


Figure 3.2.2 Fluorescent image of eukaryotic cell cytoskeleton [[Wikipedia](#)].

Actin filaments are shown in red, microtubules in green, nuclei in blue.

The eukaryotic cytoskeleton

The cytoskeleton provides the cell with structure and shape. Cytoskeletal elements interact extensively with the cellular membranes [Doherty *et al* 2008].

Eukaryotic –as the mammalian– cells contain three main kinds of cytoskeletal filaments: micro-filaments (or actin-filaments), intermediate-filaments, micro-tubules.

Microfilaments are the thinnest filaments of the cytoskeleton (6nm diameter), having a double-helix structure. They are composed of linear polymers of actin sub-units, generating force. They also act as tracks for the movement of myosin molecules.

Intermediate filaments, which are around 10nm in diameter, are more stable than actin filaments; like the latter, their function is maintaining the cell shape. Intermediate filaments organize the internal tridimensional structure of the cell, anchoring organelles and serving as structural components of the nuclear lamina and sarcomeres. They also participate in some cell-cell and cell-matrix junctions.

Micro-tubules are hollow cylinders, about 23nm in diameter (lumen \approx 15nm in diameter), made of tubulin sub-units. Microtubules have a very dynamic behavior, and their function can vary with their arrangement –with different shapes, they form either the centrioles or cilia and flagella. As both flagella and cilia are structural components of the cell, and are maintained by microtubules, they can be considered part of the cytoskeleton; they play a key role in the intracellular transport of organelles as mitochondria or vesicles.

3.3 Atomic force microscopy and colloidal probe

Atomic force microscopy (AFM), or scanning force microscopy (SFM), is a relatively-recent scanning probe microscopy technique, versatile in terms of both measurable sample and possible output. It indeed permits to extract many features and information, e.g. topographical images and characterization of different chemico-physical forces, from a wide range of samples, including biological specimen, both in dry and in liquid environment.

A general introduction on the operating principle of the AFM will be presented, followed by a focus over the two classical and more established modalities of operation, height topography and force–displacement curves, and completed by a brief overview about the colloidal probe technique and some biological applications.

3.3.1 Near-field and far-field microscopy

Microscopy permits to obtain information about a sample, particularly to image it. There are different microscopy techniques, exploiting different physical mechanisms: some irradiate the sample with electromagnetic waves (*optical microscopy*) or with electrons (*electron microscopy*), while others mechanically-probe the sample (*scanning-probe*, or *near-field, microscopy* – SPM).

Optical and electron microscopies, collectively called *far-field microscopy*, are established techniques which use waves (such as light or electrons) plus suitable imaging optics in order to create a two-dimensional projection of the sample, exploiting certain sample properties such as its local absorbency.

SPM's principle consists in perturbing a surface of the sample with a small, sharp probe (*tip*) brought into its close proximity: by guiding the probe over the sample surface, a three-dimensional relief of that surface can be created. The SPM probe, which is the core of the SPM system, has geometrical dimensions ranging from the nano- to the micro-scale. The generated relief reflects the nature of the *local* interaction between the probe and the sample [Hansma *et al* 1988].

SPM is a family of tools, comprising for example the *scanning-tunnel microscopy* (STM) and the *atomic-force microscopy* (AFM), very useful in order to study the *surface* of an object, either relatively-rigid or soft. Surfaces and interfaces are obviously everywhere, and understanding their composition and properties has tremendous value for all scientific fields, both theoretical and practical, particularly e.g. in adhesion, biology, rheology, friction studies. A significant technological improvement in surface analysis was the invention of the SPMs, which allow studying surface properties of materials from the atomic to the micron level. Initially (1980s), SPM measurements were limited to morphological output only; then, over the past two decades, they have been proven to be a great asset in solid surface characterization; in more recent years, they have been applied also to studies on soft materials and fluids, such as organic specimens, colloidal dispersions, fibers, thin films, fluid interfaces. The use of forces has proved to be a general approach [Radmacher *et al* 1992], and has made the SPM relevant to a wide range of applications, leading also to the emergence of

Tesi di dottorato in Ingegneria Biomedica, di Tommaso Novellino,
discussa presso l'Università Campus Bio-Medico di Roma in data 10/03/2011.
La disseminazione e la riproduzione di questo documento sono consentite per scopi di didattica e ricerca,
a condizione che ne venga citata la fonte.

new techniques. A list of some of the techniques currently available is reported in **Table 3.3.1.**


Tommaso Novellino
86

Technique	Common synonyms	Related techniques	Common synonyms
scanning tunneling microscopy (STM)		scanning tunneling spectroscopy (STS) scanning noise microscopy (SNM) scanning noise potentiometry (SNP) alternating current STM (ACSTM) scanning chemical potential microscopy (SCPM) scanning optical absorption microscopy (SOAM) spin polarized STM (SPSTM) ballistic electron emission microscopy (BEEM) photon emission STM (PESTM)	scanning tunneling optical microscopy (STOM) laser assisted STM (LASTM)
scanning force microscopy (SFM) atomic force microscopy (AFM)		friction force microscopy (FFM) Young's modulus microscopy (YMM) force-distance measurements	lateral force microscopy (LFM)
tapping mode AFM (TM-AFM)	intermittent contact AFM		
electric force microscopy (EFM)	scanning Maxwell stress microscopy (SMM)	scanning surface potential microscopy (SSPM) scanning Kelvin microscopy (SKM)	
magnetic force microscopy (MFM) van der Waals force microscopy (VDWFM)			
scanning near-field optical microscopy (SNOM)	near-field scanning optical microscopy (NSOM)		
aperture SNOM (ASNOM) transmission ASNOM (T-ASNOM) collection ASNOM (C-ASNOM) emission ASNOM (E-ASNOM) nonaperture SNOM (NA-SNOM) evanescent field SNOM (EF-SNOM)	photon scanning tunneling microscopy (PSTM) evanescent field optical microscopy (EFOM)		
scanning near-field plasmon microscopy (SNPM)			
scanning electrochemical microscopy (SECM)			
scanning capacitance microscopy (SCaM)			
scanning ion conductance microscopy (SICM)			
scanning thermal microscopy (SThM)	scanning thermal profiler (SThP)		
scanning near-field acoustic microscopy (SNAM)			

Table 3.3.1 Overview of different SPM techniques [Friedbacher *et al* 1999].

Historically, optical microscopy has artificially-increased the discriminative capability of the human eye; the electron microscopy has then further enhanced the achievable resolution; the scanning-probe microscopy has eventually widened the possibilities in obtaining the output (3D images instead than 2D, physical quantities as forces besides images). The resolution of the unaided human eye is, under optimal conditions, 100 µm; the common optical microscope can resolve down to 0.1 µm; the electron microscopes, *scanning electron microscope* (SEM) and *transmission electron microscope* (TEM), are able to routinely image morphological features ranging from 10 µm to 1 nm (particularly, the TEM, under ideal circumstances, is capable of atomic resolution). SPMs have some very important advantages over the optical and electron microscopes: generally, SPMs are cheaper, smaller, operable in ambient conditions, and capable of *real* topographic probing (where optical and electron microscopes can directly give only two-dimensional measurements). The invention of the AFM, particularly, has enhanced the human capabilities to deal with the nano-scale, for at least three reasons: first, it extended the SPM applications to insulating substrates; second, the AFM is capable to both acquire three-dimensional topography ranging from microns to Angstroms and measure an ample variety of forces (as van der Waals, double-layer, electrostatic, magnetic, chemical, friction, hydration) with sensitivity below nanonewtons [DiNardo 2004, Strausser *et al* 1994]; third, numerous modes of operation are continuously being discovered, broadening the SPM applications to map surface properties such as adhesion, visco-elasticity, phase-transition temperatures, thermal expansivity, diffusivity, conductivity, capacitance, electric and electrochemical potentials, and more [Wiesendanger 1994].

3.3.2 Scanning-tunnel and Atomic-force microscopy

The first and ancestor of all scanning-tunnel microscopes (SPMs) is the scanning tunneling microscope (STM), in which the probe is guided relatively to the sample such that the tunneling-current occurring between probe and the sample, separated by a distance of only few angstroms, remains constant [Binnig *et al* 1987]. In the atomic force microscope (AFM), historically derived from the former, the probe is guided over the sample surface instead by force-fields existing between probe and sample [Binnig *et al* 1986a]. Both STM and AFM have been invented by the same research group.

The STM was invented in 1981 by Gerd Binnig and Heinrich Rohrer at IBM in Zurich, Switzerland; in 1986 they were awarded the Nobel Prize in Physics for this invention. The STM was the first instrument to generate real-space images of surfaces with atomic resolution [Binnig *et al* 1982]. It uses a sharpened, *conducting* tip; a bias-voltage is applied between the tip and the sample under study; when the tip is brought within about 10 Å of the sample, electrons begin to tunnel through the 10Å-gap, from the sample into the tip or vice versa (depending upon the sign of the applied voltage) [Binnig *et al* 1982]. In order for the tunneling phenomenon to occur, both the sample and the tip must be conductors or, at least, semi-conductors. The resulting tunneling current, which is the signal used to create an STM image, varies with the tip-to-sample separation distance. More particularly, the tunneling current is an exponential function of the distance [Binnig *et al* 1982], giving the STM its remarkable sensitivity. Indeed, while imaging the sample it features a sub-angstrom vertical-resolution and an atomic lateral-resolution, measuring forces with the outstanding resolution of 10 aN [Binnig *et al* 1986a]. STM generates three-dimensional images, which are obtained by rastering (*scanning*) the probe over a defined region of the sample surface while at the same time recording the current of tunneling electrons. The rastering is accomplished by piezoelectric actuators, which can manipulate either the probe or the sample in all three spatial dimensions.

AFM was invented by Binnig, Quate and Gerber as collaboration between IBM and Stanford University in 1986 [Binnig *et al* 1986a]. The AFM probing-tip is mounted at the end of a flexible, reflective *cantilever*, which is normally fabricated by silicon micro-manufacturing [Akamine *et al* 1990]. The interaction between the AFM probe and the surface

of the sample can be exploited to perform a wide variety of tasks: imaging the sample itself [Binnig *et al* 1986a], measuring some of its significant properties [Maivald *et al* 1991, Radmacher *et al* 1992], manipulating it at the nano-scale [Sitti 2003]. In order to image the surface of the sample and to measure surface information, it is necessary to determine the forces of interaction occurring between the sample and the probe. This is accomplished by measuring the deformation of the cantilever, from which the force is then readily derived. From this force, a variety of information –as sample height (topography), surface mechanical and electro-magnetic properties– can be extracted. Indeed, ‘images’ obtained through AFM are richer in information than images produced using a different methodology as optical microscopy: they reflect, in the widest sense, the local *mechanical properties* of the sample [Maivald *et al* 1991]. In the case of hard samples, the image is dominated by the sample topology and the tip geometry; while for soft samples, the viscoelastic properties of the sample contribute significantly to the image formation [Burnham *et al* 1991].

AFM, like all SPMs, historically evolved from the STM [Binnig *et al* 1987], but, because of their different working principle, while STM is limited to conductors only, the AFM can instead image also *insulating* materials. This fact opens the possibility to experimentally characterize a wider range of materials of interest, in both the industrial processes and the biomedical applications; particularly, since AFM allows sensing of non-conducting materials under various ambient conditions, also such as physiological buffer solutions, it has become a very important and versatile tool in life sciences [Ludwig *et al* 2008].

Besides their differences, AFM shares with the STM, from which again it conceptually stemmed, the following interesting features:

- a very-high resolution, in the molecular scale [Binnig *et al* 1982, 1986a], which is mainly allowed by the presence of *piezo-electric elements*, used as actuators to position, either the probe or the sample, with an accuracy of fractions of atomic diameters [Binnig *et al* 1986b].;
- the interaction between the probe and the sample, which produces the signal from which the image or other features are extracted, is limited to only the *surface* of the sample (though, recently, a new, innovative AFM mode has been proposed in the literature [Tetard *et al* 2010], which permits to obtain also sub-surface information);
- the interaction *force* between the probe and the sample is a function of the *distance* between the probe and the sample surfaces.

As a historical note, in its first published version [Binnig *et al* 1986a], AFM used to comprise an STM, whose sample was the AFM cantilever itself (**Figure 3.3.1**). The tip was then made of diamond, while the cantilever of gold; currently, the tips are usually made either of silicon-nitride or of silicon, and they are integrated with the cantilever itself which is made of the same material than the tip. This integration, which is achieved through micro-fabrication processes, provides also a better mechanical stability [Petersen *et al* 1982]. Silicon, historically used as an electronic material only, began –because of its excellent mechanical properties– in the last few decades to be used also as a mechanical material. This rose the possibility to obtain a broad range of inexpensive, batch-fabricated, high-performance, easily-interfaced systems, the AFM cantilevers being amongst them.

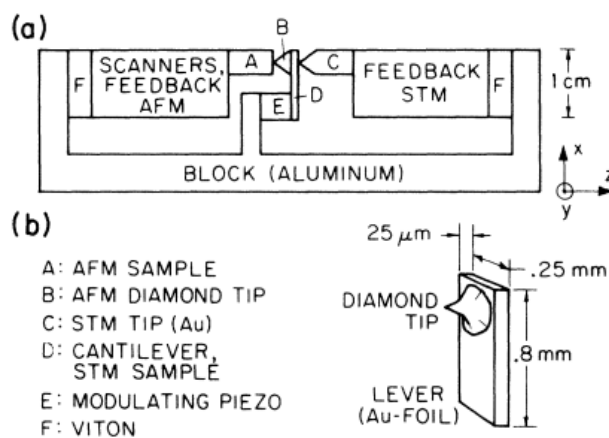


Figure 3.3.1 First AFM experimental-setup [Binnig *et al* 1986a].

- (a) System comprises also STM component; lever is not to scale.
- (b) Geometrical dimensions of lever, bearing a diamond tip.

3.3.3 AFM functioning, imaging topography and force measurement

As per the general principle, AFM, like all SPMs, uses a very sharp tip to image features and measure forces within the *near* field of a sample surface [Strausser *et al* 1994]: distances between probe tip and sample are below 1 μm , often less than 1 nm [DiNardo 2004]. The mass and dimension of the probe are small enough that the weaker, surface interactions become dominant and, therefore, accessible for scrutiny. Various applications and experimental setups consent to acquire both qualitative and quantitative knowledge about morphology, material properties, and interaction forces of diverse systems. AFM can probe mechanical interactions real-time and with molecular resolution (< 1 Å in height [Binnig *et al* 1986a] and 0.1 pN in force [Cappella *et al* 1999]). The maximum resolution that can be actually reached depends on the features of the tip (particularly its shape and sharpness) and on the experimental conditions (particularly the operating environment, i.e. either gas or vacuum or liquid); its molecular-scale is mainly due the outstanding precision of the piezo-electric elements. This high force-sensitivity can be exploited both in inorganic systems, e.g. at the molecular level to measure the force necessary to break a single chemical-bond [Stuart *et al* 1995], and in organic systems, e.g. at the cellular level where an individual cell can be evaluated in quasi-physiological situations [Dufrene 2002].

As the AFM tip is scanned over the sample surface, which can be either conductive or insulating, it experiences attractive and repulsive ultrasmall forces, which are on the atomic scale and that depend on the chemical and mechanical properties of the sample. A list of characteristic forces experienced while operating the AFM are presented in **Table 3.3.2**.

Type	Distance (nm)	Comment
Long range		
Electrostatic (air)	100	
Double layer (in electrolyte solution)	100	Depends on electrolyte concentration
Van der Waals	10	
Solvation	5	May be oscillatory; follows solvent density
Short range		
Hydrogen bonding	0.2	
Contact	0.1	

Table 3.3.2 Forces characteristically present during AFM measurements at different distances [Reich *et al* 2001].

Forces between the tip of the cantilever and the surface of the sample cause the cantilever (which acts as a spring, with an ultrasmall mass) to bend. This cantilever deflection is measured, through an appropriate detector, as either the tip is scanned over the sample or the sample is scanned under the tip; optical-lever and interferometry are most commonly used techniques to detect those deflections. In order to modulate the interaction between the probe and the sample, a physical quantity is chosen as feedback in the control of the movements operated by the piezo-electric actuators: this in virtue of the fact that the interaction depends on the tip-sample distance. While measuring the cantilever deflection, at the same time the AFM measures motion of the cantilever or of the sample (depending on the system, either one of the two can be moved). The raw data originally measured by the AFM are thus the relative position of the scanner and the deflection of the cantilever. The measured cantilever deflections, which are used as a measure of the interaction forces, are acquired by a computer and can be used to generate the final output(s), e.g., a map of the surface topography (in the so-called *imaging* mode), a profile of the force as a function of the distance (in the so-called *force* mode), or others (as in **Table 3.3.1**). Usually, only relatively small samples – few centimeters in any dimension – can be probed by AFM, depending on scanner size. Typically, square regions having side length in the order of microns may be measured without having to move the sample (either manually or with motors). Surface features varying more than several microns from-peak-to-valley are not accessible and may damage the probe tip. Another important feature, besides sample size and smoothness, is the vibration

isolation, which can be achieved in different manners; since the ultrasmall dimensions of interest, any acoustic, electrical, structural vibration can seriously hamper the AFM capability to resolve features, so it should be provided with reliable noise isolators (this is also true for other SPMs). Atomic resolution can be routinely achieved even under ambient conditions with good isolation and extremely flat samples. Because of the very low mass of the cantilever, permitted by micro-fabrication [Petersen *et al* 1982], the force to move the cantilever through measurable distances (10^{-4} Å) can be as small as 10 aN [Binnig *et al* 1986a]. In air, the AFM exhibits a vertical resolution < 1 Å and a lateral resolution of 30 Å, depending also on the tip configuration; in optimal conditions, force sensitivity can be down to 1 fN at room temperature [Binnig *et al* 1986a]. Force sensitivity is limited by thermally-induced vibrations of the cantilever, so it could be decreased by decreasing the operating temperature. This level of sensitivity, allowed by the fact that the mass is so small, permits the AFM also to detect inter-atomic forces between single atoms. Generally speaking, the AFM can measure not only interatomic forces, which range from 0.1 µN (ionic bonds) down to 10 pN (van der Waals bonds), but any type of force, including electro-magnetic [Binnig *et al* 1986a]. While having an appropriately-sized tip is important for acquiring real surface features with atomic resolutions, the most important advancement –which ultimately enabled the AFM, and more generally SPMs, to reach sub-Angstrom precision– is the presence of the piezoelectric transducers: with proper vibration isolation, they have typical planar (x, y) and height (z) resolutions around 20 Å and 1 Å, respectively [Strausser *et al* 1994], and even two orders of magnitude lower are possible under ideal conditions.

3.3.3.1 AFM components

AFM, and more generally SPM, setups have varied in a few important ways since their production, from homemade units to standard commercial models [Binnig *et al* 1982, Strausser *et al* 1994, Lieber 1994]. While designs for ambient and vacuum operating conditions are common, the SPM can be fitted also with a liquid cell under ambient or purged atmospheres (N₂ or Ar).

Cantilever

Commercial cantilevers are usually made of either silicon or silicon nitride (Si_3N_4), and can be also differently-shaped (**Figure 3.3.2**). Spring constants for commercial cantilevers span a few orders of magnitude, i.e. $0.01 \div 100 \text{ N/m}$. The hardness of the sample as well as the particular forces of interest, in general, dictate the desired stiffness of cantilever. Deflections corresponding to typical atomic interactions (such as van der Waals attraction and electrostatic repulsion) are usually of the order of nanometers, generating forces of less than $0.1 \mu\text{N}$; but studies in friction, nanowear and nanoindentation often deal with force greater than $1 \mu\text{N}$ [Bhushan *et al* 1995].

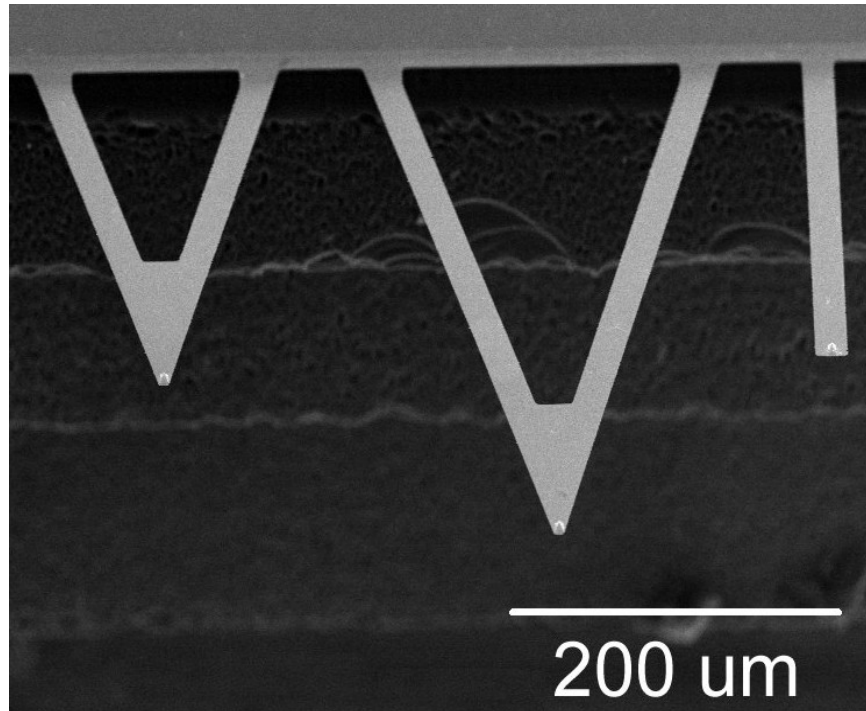


Figure 3.3.2 Some of the different AFM cantilevers commercially-available.

Probe

On the apex of the free-end of the cantilever is placed the AFM probe (*tip*), which can be variously-shaped or even absent (*tipless* cantilever). A very common shape is the pyramidal one (**Figure 3.3.3**), which is atomically-sharp, having radius of curvature in the order of magnitude of the nanometers: typical radii of curvature are $5 \div 50 \text{ nm}$ [Tykoniuk *et*

al 2007] or more broadly 10÷100 nm [Ott *et al* 1994]; another common shape is the conical one. While the previous tips are built as already-integrated with the cantilever structure, many other possibilities are offered by the so-called *colloidal-probe* technique, consisting in customly-attaching different materials with different shapes to a cantilever (usually tipless). This permits to partially-choose –at least on the AFM side, the sample is not always controllable or modifiable– the type and order-of-magnitude of the forces of interaction (choosing the material) and the geometry of the interaction (choosing the shape). Particularly, AFM can be used to explore adhesive interactions between cells and particles, as it has been done in the present work. A set of examples of different AFM “colloidal” probes (where, in the literature, the adjective ‘colloidal’ is used for particles sizing also more than 1 μ m) is shown in **Figures 3.3.4÷7**, where the probe can be constituted not only by nano- or micro-particles, but also by cells.

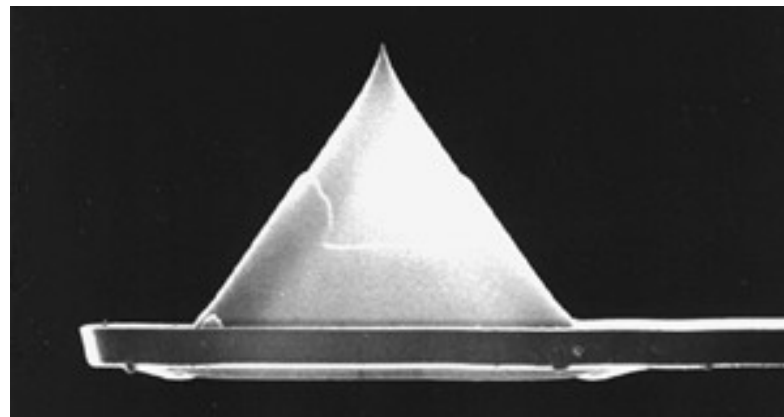


Figure 3.3.3 Typical pyramidal AFM tip.

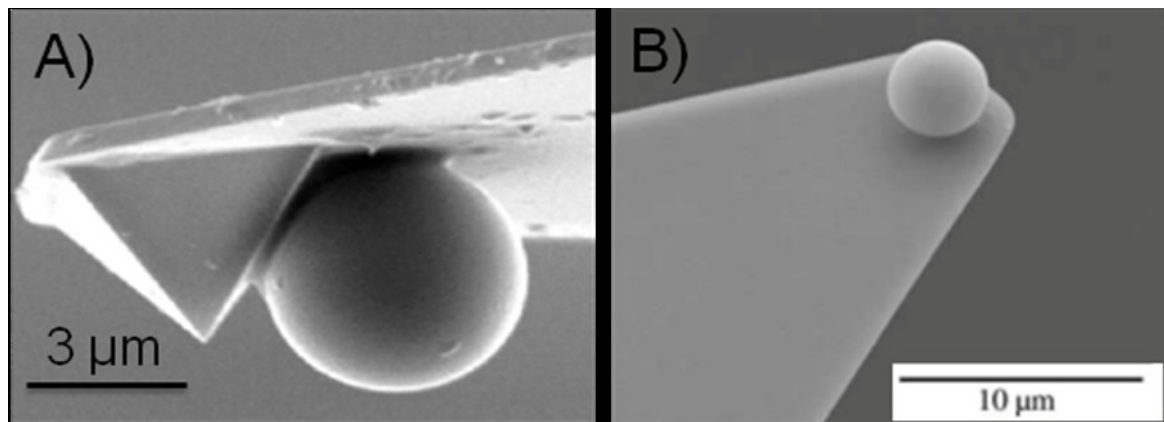


Figure 3.3.4 Micro-particle colloidal probe, mounted on a cantilever either tipped (**A**) [Berdyyeva *et al* 2005] or tipless (**B**) [Kappl *et al* 2002].

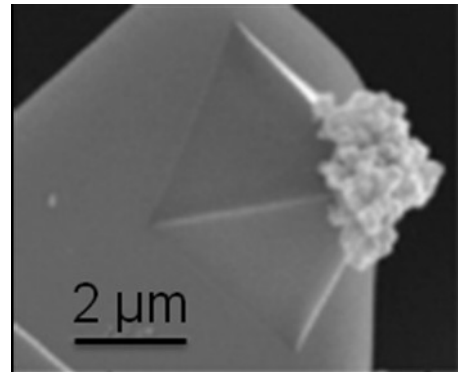


Figure 3.3.5 Nano-particle colloidal probe, made by $\approx 50\text{nm}$ ceria particles [Ong *et al* 2007].

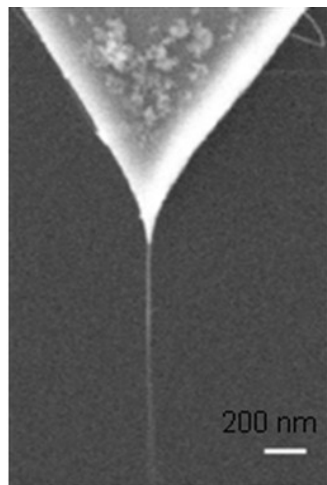


Figure 3.3.6 Carbon-nanotube colloidal probe [Hafner *et al* 2001].

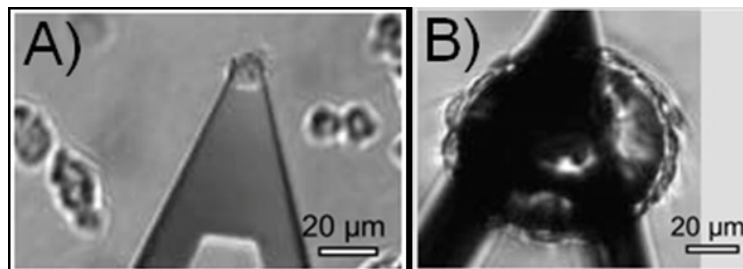


Figure 3.3.7 Bio-colloidal probe, where either a single-cell (**A**) or a cell-monolayer (**B**) has been attached to the cantilever [Benoit *et al* 2002].

Scanner

Piezo-electric elements are an important AFM part and reason for its success. AFM, as SPM, movements are permitted by actuators which are made of piezo-electric transducers. A piezo-electric material, by definition, transduces an electrical voltage in a mechanical deformation and vice versa; in AFM, only the direct principle is exploited, where the actuators deform in dependence of the applied voltage. Whether they elongate or contract, depends upon the polarity of the voltage applied. The piezoelectric material expands preferentially with the application of a potential bias between the appropriate electrodes and ground: a difference of electric potential of 1 V gives a $\approx 10 \text{ \AA}$ displacement for the usual

ceramics [DiNardo 2004]. The AFM *scanner* is composed of several piezo-actuators, permitting to independently-operate the x , y and z directions (usually, one piezo-transducer is user for z movement and another for x - y movements). The actuators allow manipulating either the sample or the AFM probe with extreme precision in the three spatial dimensions, whether the scanner tube moves either the sample relative to the tip or the opposite depends on the AFM structure and model. AFM piezo-actuators show nonlinearity and hysteresis, which can cause feature distortion in AFM imaging but which can be corrected (e.g. by applying a proper nonlinear voltage to the piezo-electrodes as in [Elings *et al* 1991], shown in **Figure 3.3.8**). Another piezo-scanner property is aging: the sensitivity of piezoelectric materials decreases exponentially with operation time, so most of the change in their sensitivity occurs at the early beginning of their life, while after that they will need seldom recalibration.

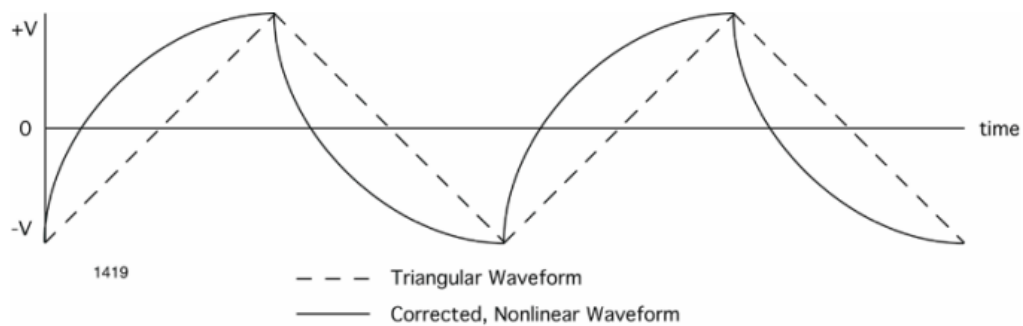


Figure 3.3.8 Waveforms used to control piezo-actuator movement [Elings *et al* 1991]. Non-linear waveform (solid line) applied to the piezo-electrodes to produce linear scanner-movement; the unaltered triangular waveform (dashed line) is included for reference.

3.3.3.2 AFM measurement

Deflection sensor

Three techniques for measuring the deflection of the cantilever are: electron tunneling to the back of the cantilever [Binnig *et al* 1987], interferometry [Erlandsson *et al* 1988], and detecting the angular deflection of a laser beam reflected from the back of the cantilever

[Meyer *et al* 1988a,b, Alexander *et al* 1989]. Although various ways are existing to measure the cantilever deflection [Wickramasinghe 1990, Amer *et al* 1988], all commercially-available instruments do this optically, either by interferometry or with displacement sensors [Radmacher *et al* 1992].

The cantilever deflection is most typically measured through a laser beam (**Figure 3.3.9**). The laser is emitted and focused over the cantilever's apex, which is located on the upper face of the cantilever (while the tip is located downwards facing the sample to be scanned) and which is usually covered by a reflective layer (e.g. gold) in order to increase the optical output and the resolution. The apex reflects the laser beam onto a sensor, a position-sensitive photo-diode (PSPD), which converts it into an electric voltage; the latter is further elaborated and used to control, through the feedback and the electronics, the piezo-actuators. The deflection signal, i.e. the laser reflected from the apex onto the photo-diode, can be exploited in two different ways of reading, which are perpendicular one to the other: one (normal) for imaging and the other (lateral) for friction measurement, as shown in **Figure 3.3.9**.

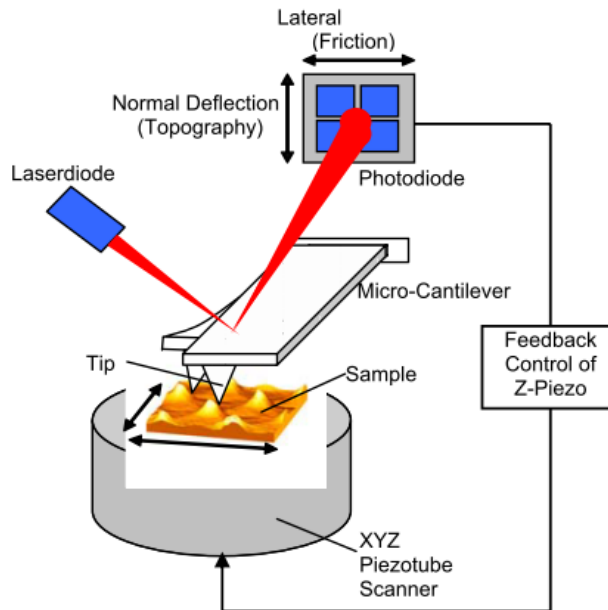


Figure 3.3.9 AFM typical set-up, showing two different possible modalities of interpreting the deflection signal [Sitti 2004].

Force derivation and interpretation

The interaction force between the surfaces of the cantilever's tip and of the sample depends on both:

- the current *distance* between the tip and the sample (distance which is not directly measured by the system, but which can be easily calculated), here indicated as D ;
- the *history* of pathway which has been followed up to that particular moment, which is reflected in phenomena as hysteresis of piezo-elements and of force–distance curves and as sample–tip adhesion.

The cantilever deflection, which is determined by the interaction between the cantilever tip and the sample, also depends on those two aspects. In the range of displacements and forces where the AFM cantilever is usually operated, it can be assumed to behave like a linear spring, hence the cantilever deflection (d) is related to the force mutually-exerted between the tip of the cantilever and the sample (F) through the Hooke's law:

$$\vec{F} = \mathbf{k}_{CL} \cdot \vec{d} \quad (\text{Equation 3.3.1})$$

Tommaso Novellino
 101

where k_{CL} indicated the spring-constant of the cantilever.

There are two opposite requirements on the cantilever's spring constant (k_{CL}): from one side, it is desired to be low, in order to increase sensitivity (maximum deflection for a given force) for the forces of interest; but, at the same time, it should be high, in order –by increasing the cantilever resonance-frequency– to minimize its sensitivity to vibrational noise (e.g. that, around 100Hz, normally present in buildings) [Binnig *et al* 1986a]. But, since the cantilever's resonance-frequency (f_{CL}) is given by:

$$f_{CL} = \frac{1}{2\pi} \sqrt{\frac{k_{CL}}{m_{CL,eff}}} \quad (\text{Equation 3.3.2})$$

where $m_{CL,eff}$ is the effective mass of the cantilever, it is then possible to simultaneously decrease both k_{CL} and $m_{CL,eff}$ in order to augment the f_{CL} value. Here becomes clearer the importance of microfabrication in reducing cantilever's mass. In order to obtain absolute values of the interaction force, it is clear of being the utmost importance a correct and reliable calibration.

So the force of interaction can be simply calculated from the measured deflection and the knowledge of the cantilever spring-constant, which has to be calibrated prior to the actual experiment. Actually, that force is the *total* equilibrium force (acting between tip and sample at a given separation), but a challenging aspect of AFM is discriminating the different types of interactions included in that total force, which depend on the particular application. For e.g., between the several forces which typically contribute to the deflection of an AFM cantilever, the most common is the van der Waals interatomic force, whose dependence with the distance D between the tip and the sample is shown in **Figure 3.3.10**. Two distance regimes are shown in **Figure 3.3.10**: the so-called *contact* regime and *non-contact* regime. In the contact regime, the cantilever is held less than a few angstroms from the sample surface, and the interatomic force between the cantilever and the sample is repulsive. In the non-contact regime, the cantilever is held on the order of tens to hundreds of angstroms from the sample surface, and the interatomic force between the cantilever and sample is attractive (largely as a result of the long-range van der Waals interactions). These different regimes are exploited in different imaging techniques, as detailed subsequently.

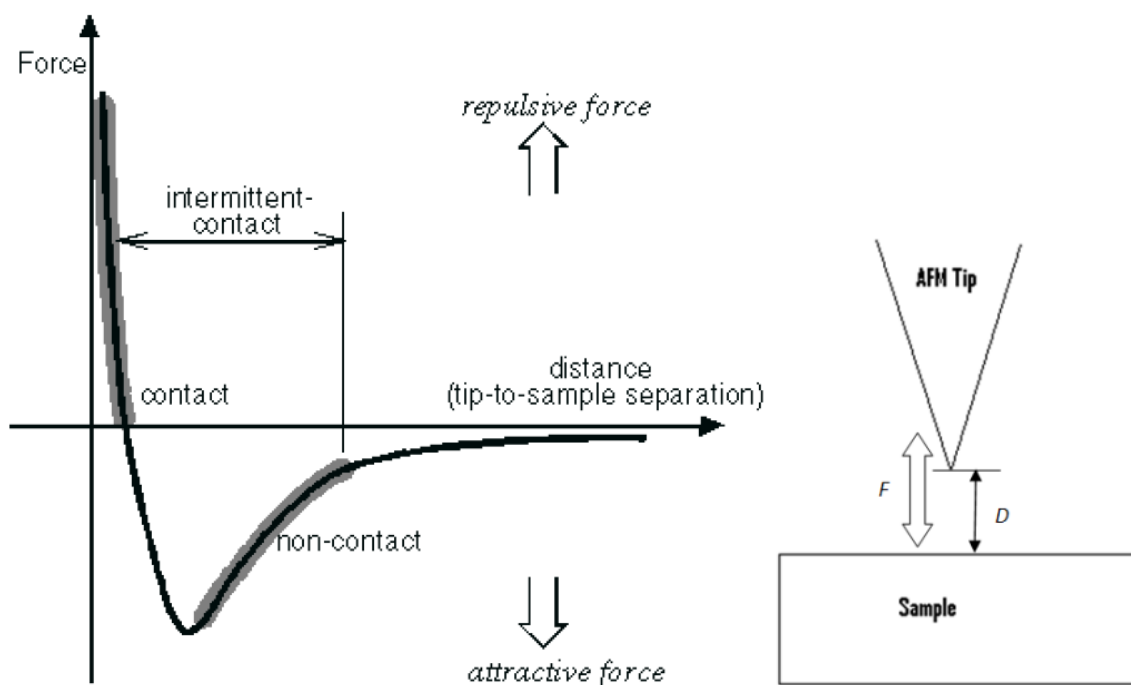


Figure 3.3.10 Van der Waals force as a function of the distance [Howland *et al* 2000].

3.3.3.3 AFM modalities

The AFM can be operated in several different modes of operation, each permitting to obtain different quantities of interest, the choice of the most suitable mode usually depending on the application. AFM, as well as other SPMs, can image the topography of the sample, measure the interaction force between the sample itself and its tip as well as other physical properties –such as surface conductivity, static charge distribution, localized friction, magnetic fields, elastic moduli. This can result in very diverse applications. Those applications and the variety of different quantities which is possible to assess are supported by different operating modalities available.

In each modality, there is usually a different physical quantity –as the deflection of the cantilever or the amplitude of the induced-oscillation of the cantilever– which is elaborated and used as electronic input in order to control the movements of the piezo-scanner. More specifically, the piezo-scanner is controlled both in the z direction, in order to

modulate the sample–tip separation distance, and in the xy directions, in order to move on specific point on the sample surface. The piezo-scanner typically needs to be guided in order not to damage both the AFM system and the sample, as well as to extract significant properties from the measurement. Thus, feedback is very often used; anyway, sometimes feedback is disabled, e.g. in the so-called *constant height mode*, where the deflection signal is only used to create the image and is only recommended for atomically-flat surfaces. The most basic modalities of operation are the imaging modality and the force modality.

Imaging modality

If used in the so-called *imaging* modality, the AFM can provide the topography of a sample, a map of its relative heights for each point of a defined surface area of the sample. For each point (x, y) in the chosen sample area, the corresponding height –better, the relative variation of the sample height– is recorded. Those acquired data can then be further elaborated as colors (each height corresponding to a certain color), which can produce a 2D colorimetric-map of the sample or be plotted as a 3D-image. As the AFM image is obtained by from the force created on the sharp tip by the proximity with the surface of the sample, depending on the relative average distance between the tip and the sample, different imaging modes are available: the so-called *contact*, *intermittent-contact* (or *Tapping®*) and *non-contact* modes.

The AFM was first used to image samples [Binnig *et al* 1986a]. The first way to image samples was the so-called *contact* mode, which is also one of the currently most utilized for its simplicity. In contact mode, the feedback quantity is the cantilever deflection d . The AFM system behaves in order, adjusting properly Z (i.e. the height, in the z direction) of its piezoelectric motors, to keep constant d (hence, because of the Hooke's law, also the interaction force F will be kept constant). The resulting image is an isoforce relief of the sample, depending also on the operating environment. E.g., when imaged in air, the meniscus force of a wetting water film may dominate the attraction [Radmacher *et al* 1992]; when scanning in liquids, the overall forces between the tip and the sample are typically – depending on the size of the tip used– $10 \text{ pN} \div 10 \text{ nN}$, lower than in ambient air.

Force modality

The AFM, as previously mentioned, first application was imaging the topography of surfaces with high resolution; however, soon after its invention, it was realized that it could also be used to directly measure forces, exploiting its core principle-mechanism, in the so-called

force modality, pioneered around 1989 [Meyer *et al* 1989, Weisenhorn *et al* 1989]. This modality permits to obtain a plot of the interaction force between AFM tip and sample surface as a function of their distance, the so-called *force-distance (F-D)* curve, or simply *force curve*; data from such force–distance curves are useful to study all kinds of surface forces or material properties like adhesion events or elasticity [Kappl *et al* 2002]. As in 3D images (topography), in force measurements (spectroscopy) the piezoelectric actuators (whose height is measured) permit to vary the tip–sample relative distance and so the force of their interaction, hence the cantilever deflection; the measured value of the latter can be used as feedback to electronically-control the actuators, in order to perform a controlled measurement and to not damage the sample.

While topography is obtained by probing a certain area of the sample, force curves are instead obtained in a specific point of that area, ramping the probe over the sample while measuring the cantilever deflection; since again Hooke's law holds, the interaction force can be calculated. The ramping movement consists in one or more cycles of two phases: the *approach* or *extension* phase, where the probe and the sample decrease their relative distance; and the *retraction* phase, where the probe gets further from the sample. In this way, fixing the (x, y) coordinates, an entire force-profile, in a pre-defined z -range of ramping (which is referred to as *ramp size*), can be obtained for a specific sample-point. The typical AFM cycle –consisting in the approach-to-contact before and retraction-to-starting-point then, both along the z axis– is controlled by variables input before acquisition, e.g., the maximum deflection permitted (*setpoint*) or force exerted on the sample (*trigger mode*), the cantilever approaching and retracting velocity, the delay time of residency of the probe over the sample once in contact, etc.

Cantilever deflection versus z -displacement gives a force curve. Using **Equation 3.3.1**, it is possible to obtain, from the AFM raw data (d – Z curves), F – Z curves.



3.3.4 AFM applications

Although its relatively-recent invention, AFM has been widely used to study the physical properties of inorganic and also organic samples at the nanoscale: it can, for e.g., quantify forces in the range of a single antibody–antigen interaction [Ludwig *et al* 2008]. A representative gallery of AFM outputs spanning different samples from the atomic to the cellular scale is provided in **Figure 3.3.11** [Reich *et al* 2001].

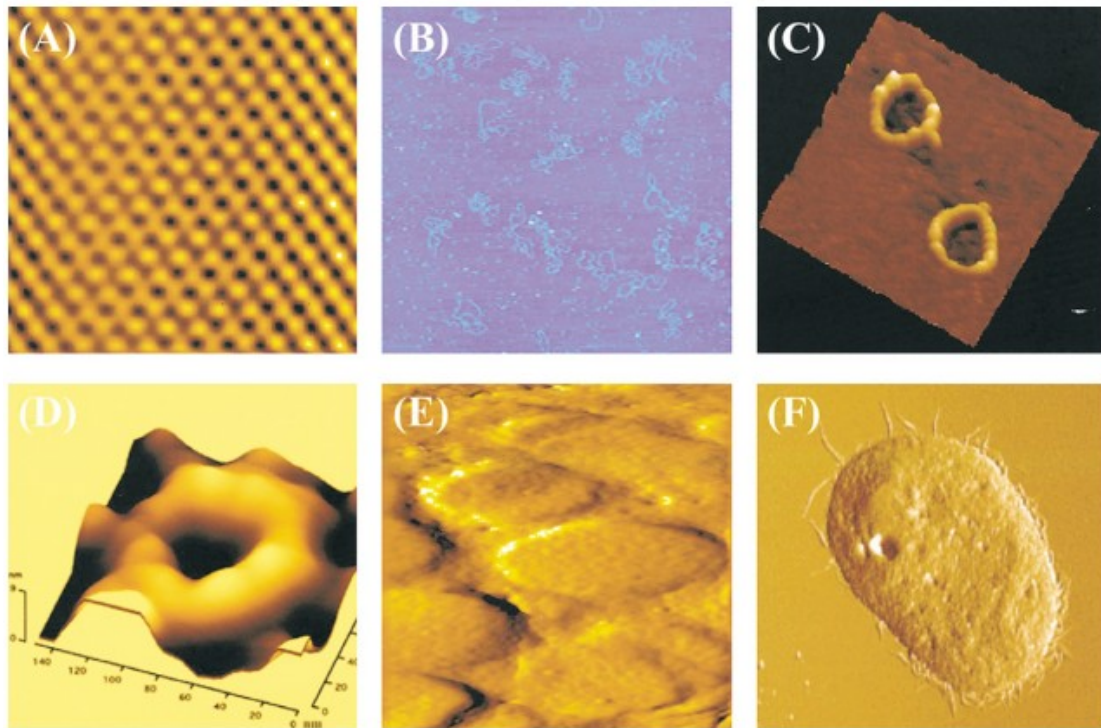


Figure 3.3.11 AFM images showing from atoms to cells: (A) mica, (B) plasmid DNA, (C) RecA–DNA complex, (D) nuclear pore complex channel, (E) intact thylakoid, (F) *Tetrahymena* cell [Reich *et al* 2001].

The following AFM features allow it to follow dynamics and processes on the molecular and cellular scale directly: its non-invasive nature (if applied force does not

damage the sample), its possibility to operate under wet condition, its high force-sensitivity (≈ 0.1 pN), its possibility to investigate biological samples under physiological conditions without fixation or other invasive sample preparation [Dufrene 2002].

Particularly, AFM has a unique advantage in studying mechanics, particularly in cells: the AFM-tip lateral position as well as the load force can be controlled with extremely high precision [Sokolov 2007]. An overview of a specific mechanical property –the Young's modulus– of many biological as well as abiological materials is presented in **Table 3.3.3**. More particularly, cytoskeletal actin de-polymerization produces a decrease in cell Young's modulus [Sugitate *et al* 2009].

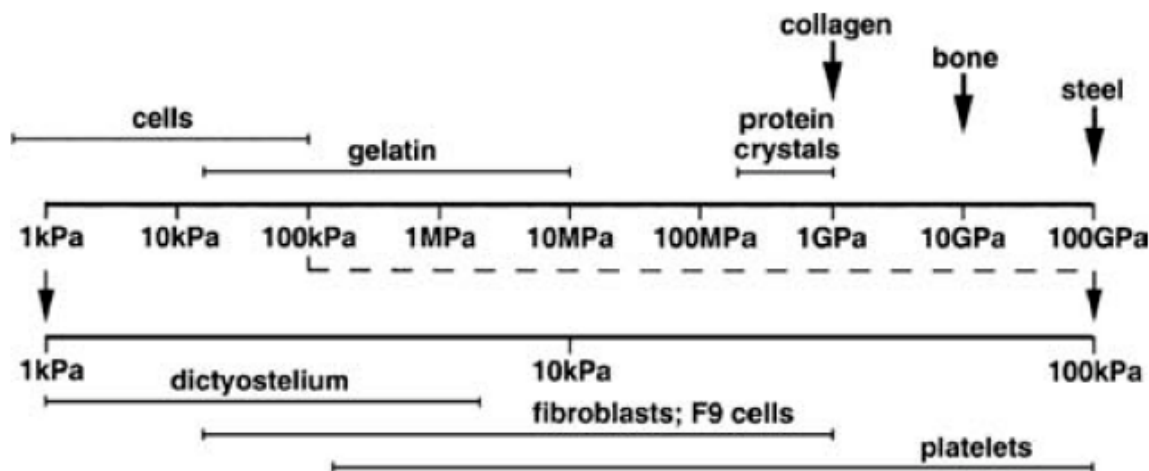


Table 3.3.3 Young's moduli of different materials, showing a spectrum from very hard to very soft [Sokolov 2007].

Steel > bone > collagen > protein crystal > gelatin, rubber > cells; a considerable variation of rigidity even within cells can be observed.

Inorganic samples

As per abiological applications, AFM has been proven useful particularly in material science as it has been used to study, for e.g.: the interaction between different couples of materials (polystyrene–silicon, polystyrene–mica, polystyrene–polyurethane, polystyrene–gold, silica–silicon, etc.), particularly exploiting the colloidal-probe technique [Kappl *et al*

2002]l; the direct interaction between a single nanoparticle and surfaces, attaching nanoparticles to the AFM tip [Ong *et al* 2007].

Organic samples

As per biological applications, AFM has been used, for e.g., for imaging of various samples of biological origin (DNA, DNA–protein interaction, proteins, lipid membranes, cells) and also for measuring forces in several contexts (force mapping on living cells, force curves in single-molecule inter- and intra-molecular interactions) [Alessandrini *et al* 2005]. Both cellular and acellular/subcellular have been measured by AFM.

As per acellular samples, the following ones were, for e.g., studied: cell membranes with bound proteins and gap junctions [Radmacher *et al* 1992]; frequency-dependent microrheology of polymer gels [Mahaffy *et al* 2000].

As per whole cellular samples, whole-cell imaging by AFM is a complicated process due to a complex mixing between topography and mechanical and frictional forces; moreover, if the cells are imaged under native, hydrated conditions, then additional complications –associated with surface compliance, lateral displacements, surface instability– come into play. Consequently, spatial-resolution drops considerably, typically reaching 10÷50 nm [Reich *et al* 2001]. Despite these obstacles, cells were amongst the first biological substances to be imaged by AFM, first under fixation conditions [Butt *et al* 1990] and later under living, native, hydrated conditions [Haberle *et al* 1991], using micropipettes to hold the cells during scanning. Later on, AFM has been applied to study a wide range of cellular phenomena. More specifically, AFM has been applied to evaluate: adhesion forces between live cells or between live cells and surfaces, particularly attaching cells on the AFM cantilever (what can be called 'cell probe') [Benoit *et al* 2002]; frequency-dependent complex shear modulus (elastic and dissipative behaviors) of live cells [Alcaraz *et al* 2003]; uptake rate and adhesion force between micro-sized particles (positively- and negatively-charged polymer micro-capsules) and cells [Munoz Javier *et al* 2006]; nanomechanical properties, surface and molecular-recognition forces of microbial cells [Gaboriaud *et al* 2007]; force of nanoparticle–cell membrane interactions and its influence on intracellular trafficking of nanoparticles [Vasir *et al* 2008]; differences in mechanical modulus between normal and cancerous cells, and also the ECMs produced by them [Pernodet *et al* 2008]; differences in the surface-brush of normal and cancerous cells [Iyer *et al* 2009].

3.4 Influence of pro-inflammatory cytokine on cytoskeleton organization

In this study [Lee *et al* 2011], the mechanical properties of TNF- α -stimulated endothelial cells were probed by atomic force microscopy (AFM) in order to evaluate their possible dependence on such patho-physiological biochemical substance.

Tumor Necrosis Factor- α (TNF- α) is a potent pro-inflammatory cytokine that regulates the permeability of blood and lymphatic vessels. The plasma concentration of TNF- α is elevated ($>> 1$ pg/ml) in several pathologies, including arthritis rheumatoid, atherosclerosis, cancer, pre-eclampsia, obesity and trauma. To test whether circulating TNF- α could induce similar alterations in different districts along the vascular system, three human endothelial cell lines –namely HUVEC, HPMEC and HCAEC– were characterized in terms of:

- mechanical properties, employing atomic force microscopy;
- cytoskeletal organization, through fluorescent optical microscopy;
- membrane over-expression of adhesion molecules, by sandwich immuno-assay (ELISA) and fluorescent immuno-staining.

As it will be shown later in greater detail, upon stimulation with TNF- α (10 ng/ml for 20h), for all three endothelial cell-lines:

- the mechanical stiffness increased by about 50%, with a mean apparent elastic modulus of $E \sim 5 \pm 0.5$ kPa ($\sim 3.3 \pm 0.35$ kPa for the control cells);
- the density of F-actin filaments increased in the apical and median planes;
- the ICAM-1 receptors were over-expressed as compared to controls.

Collectively, these results demonstrate that sufficiently-high levels of circulating TNF- α have similar effects on different human endothelial districts, and provide additional information for unraveling the possible correlations between circulating pro-inflammatory cytokines and systemic vascular dysfunction.

3.4.1 Inflammation and surface adhesion molecules

Along the circulatory system, endothelial cells (ECs) line the walls of blood and lymphatic vessels and finely regulate the exchange of nutrients and waste products between the vascular compartment and the surrounding tissue.

The solute exchange is accomplished through two pathways: transcellular and paracellular [Komarova *et al* 2001]. The first pathway is associated with the active transport of macromolecules (plasma proteins) and particulate-agents across the endothelial layer, mediated by cellular vesicles, following a process known as transcytosis. The second pathway is associated with the convective and diffusive transport across the inter-endothelial gaps within adjacent cells.

Depending on the organ and vascular district, the proportion of paracellular to transcellular transport varies. In organs of the reticulo-endothelial system (RES) –such as the liver, spleen and bone marrow– the discontinuous and highly-fenestrated endothelium favors the paracellular transport across vascular openings, which can be as large as several hundreds of nanometers [Michiels 2003]. Differently, the vasculature in non-RES organs is characterized, under physiological conditions, by a continuous endothelium, which does not allow the extravasation of solute molecules larger than 3÷5 nm [Michiels 2003].

The integrity of the vessel walls and the regulation of the para- and trans-vascular transport are of fundamental importance in preserving tissue–fluid homeostasis. Several factors are known to alter the paracellular and transcellular transport, eventually leading to unbalanced homeostasis and major vascular dysfunctions. These include physical factors –as the trans-endothelial hydrostatic fluid pressure [Tokuda *et al* 2009]– and biochemical factors –as:

- the pro-angiogenic cytokine VEGF (Vascular Endothelial Growth Factor) [Dvorak 2006];
- the pro-inflammatory cytokines TNF- α (Tumor Necrosis Factor - α) [Worral *et al* 1997], histamine [Pober *et al* 2007] and thrombin [Komarova *et al* 2007];
- bacterial toxins, as lipopolysaccharide (LPS) [Wu *et al* 2005].

All these circulating molecules and agents can recognize counter-molecules (receptors) expressed on the ECs and trigger an increase in vessel permeability, favoring the paracellular

transport.

The continuum endothelium in healthy vessels can become hyperpermeable during an inflammatory process. This is a normal response to external injury and pathogens in which TNF- α plays a major role, being involved in the activation and maturation of leukocyte and in the over-expression of specific adhesion molecules on the endothelium (E-selectin, ICAM-1, VCAM-1), which eventually favor the local recruitment of circulating leukocytes. A large number of diseases, not associated with any external stimuli or injury, are known to induce high plasma-levels of several cytokines, including TNF- α .

In healthy patients, the plasma level of TNF- α is generally smaller than 1 pg/ml, but its concentration can be abnormally high:

- in the presence of atherosclerosis [Bozkurt *et al* 2009, Feldman *et al* 2000, Libby *et al* 2006, McKellar *et al* 2009];
- during tumorigenesis and tumor growth [Kim *et al* 2006];
- in patients with rheumatoid arthritis [McInnes *et al* 2007];
- in women undergoing pre-eclamptic pregnancies [Laskowska *et al* 2006];
- in obese individuals [Rocha *et al* 2009];
- in incidences of acute trauma, including –but not limited to– traumatic brain injury [Harting *et al* 2008] and hemorrhagic shock [Roumen *et al* 1993, Suter *et al* 1992].

Also, others have reported that soluble forms of membrane receptors (TNFR) rather than TNF- α are initially released following trauma (based on serum levels one hour after arrival at a trauma center) and may serve as an indirect indicator that TNF- α associates with trauma [Tan *et al* 1993]. Significantly elevated TNF- α levels have also been linked to the onset of multiple organ failure (MOF) in trauma patients, where elevated cytokine levels, as early as one hour post admission to a trauma center, are indicative of risk of developing MOF [Roumen *et al* 1993].

In this study, three human ECs originating from different vascular districts –namely coronary (HCAECs), pulmonary (HPMECs) and umbilical (HUVECs)– were analyzed upon stimulation with TNF- α in terms of mechanical properties and cytoskeletal re-organization.

In particular, the apparent elastic modulus, the viscoelastic response and the non-specific adhesion force for the three ECs were estimated using atomic force microscopy (AFM). This technique has been successfully used in characterizing the mechanical response of several cell types in different species [Iyer *et al* 2009, Mahaffy *et al* 2004, Mathur *et al*

2001].

In addition, the biological response of the three ECs to the pro-inflammatory stimulus was characterized by observing the re-organization of the F-actin filaments within the cytoskeleton, through fluorescence microscopy, and by quantifying the level of membrane expression of adhesion molecules, as ICAM-1, through ELISA and immunostaining. The main objective of the present analysis is understanding how and if the response to TNF- α would depend on the vascular district.



A handwritten signature in black ink, appearing to read "Tommaso Novellino".

112

3.4.2 Experimental methods

Cell culture and TNF- α treatment

Supplies were purchased from the following sources:

- Human Coronary Artery Endothelial Cells (HCAECs; Cat# CC-2585, Lot# EN000307), Endothelial-cell Basal Medium-2 (EBM-2), Endothelial-cell Growth Medium (EGM-2) BulletKit (SingleQuots) were purchased from *Lonza* (Walkersville, MD, USA);
- Human Pulmonary Microvascular Endothelial Cells (HPMECs; Cat# C-12281, Lot# 9030501) were ordered from *PromoCell* (Heidelberg, Germany);
- Human Umbilical-Vein Endothelial Cells (HUVECs; Lot# EN000307) were purchased from *GlycoTech* (Gaithersburg, MD, USA);
- Tumor Necrosis Factor-alpha (TNF- α) and Anti-ICAM-1 fluorescein isothiocyanate (anti-ICAM-1-FITC) were purchased from *Biosource* (Camarillo, MD, USA);
- Treated cell culture dishes (60 x 15mm) were provided by *Corning* (Corning, NY, USA);
- Pre-cleaned glass microscope slides (3"x 1"x 1.0mm) and Tween 20 were obtained from *Fisher Scientific* (Pittsburgh, PA, USA);
- Triton X-100 was ordered from *ICN Biomedicals* (Aurora, OH, USA);
- Anti-ICAM antibody was purchased from *NeoMarkers* (Fremont, CA, USA);
- Anti-mouse IgG 2b (γ -2b)-peroxidase and 2,2'-azino-bis(3-ethylbenzthiazoline-6-sulphonic acid) (ABTS) were purchased from *Roche* (Indianapolis, IN, USA);
- AlexaFluor555–Phalloidin was obtained from *Molecular Probes, Invitrogen*.

In order to investigate the influence of TNF- α on the cell membrane elasticity, HCAEC, HUVEC and HPMEC were seeded in a 60mm culture dish to 80% confluence, with EBM-2 medium supplemented with an EGM-2 BulletKit and incubated 24h at 37°C in a 5% CO₂ atmosphere. The cells were then treated with 3ml of TNF- α , reaching a final concentration of 10ng/ml, for 20h [Danila *et al* 2009] to promote an inflammatory response. Culture dishes were later rinsed with EBM-2 media to wash out the TNF- α solution. Data were all taken at



room temperature in a liquid environment (cell medium).

ELISA and Immunofluorescence Analysis

Cells ($2.5 \cdot 10^4$ cells/well) were grown in EBM media supplemented with an EGM-2 Bullet Kit (Cambrex) at 37 °C in 5% CO₂. ICAM-1 was expressed on the surface of the HCAEC, HUVEC and HPMEC by activating them with 10 ng/ml TNF-α for 20 hours, and the extent of ICAM-1 expression was assessed by ELISA. The same cell density was used for both ELISA and fluorescence microscopy assays.

For ELISA, the cells were incubated with TNF-α (10 ng/ml) for 20 hours at 37 °C and 5% CO₂ in a 96-well plate. The next day, the cells were washed with PBS, fixed with Formalin for 20 minutes at room temperature, incubated with 3% BSA and 0.1% Tween 20 for 1 hour and then incubated with anti-ICAM antibody (1:1000 dilution in PBS, v/v) for 2 hours at 25 °C. The unbound anti-ICAM antibody was removed from the activated cells by washing with PBS, and the cells were incubated with anti-mouse IgG 2b (γ-2b)-peroxidase (1:2000 dilution in PBS, v/v) for 1 hour at room temperature. The excess of secondary antibody was washed away with PBS and then ABTS substrate (100μl) was added. After 30 minutes of incubation, the absorbance at 405 nm was measured with a plate reader (Tecan). Non-activated cells were also subjected to ELISA as controls.

For fluorescence microscopy measurements, cells ($2.5 \cdot 10^4$ cells/chamber) were incubated in 8-chamber tissue culture slides overnight at 37 °C in 5% CO₂. The next day, the cells were activated with TNF-α (10 ng/ml in EBM-2 media) for 20 hours at 37 °C in 5% CO₂. Next, the cells were washed with PBS and fixed with 4% paraformaldehyde for 15 minutes at room temperature. The cells were then washed two more times with PBS, and incubated with a solution of 0.1% Triton X-100 in PBS for 5 minutes. The unreacted sites were blocked with 1% BSA for 20 minutes. To stain actin filaments, the cells were then incubated with Alexa Fluor 555-phalloidin (5 units/ml [0.16 μM]) for 30 minutes at room temperature, and washed two times with PBS before the chamber partitions were removed and the slides were dried in air. The cells' nuclei were labeled with DAPI and then the images were captured with an Olympus IX71 inverted microscope equipped with TRITC and DAPI filters for epi-fluorescence measurements.

Atomic force microscopy experimental set-up

A Bioscope-II atomic force microscope (*Veeco*, Santa Barbara, CA, USA), combined with an inverted fluorescence microscope (*Nikon TE-2000*, Melville, NY), was used for testing and imaging the cells.

The AFM probe consisted of a 5 μm -diameter silica particle (colloidal probe), attached (*Novascan*, Ames, IA, USA) at the edge of a silicon nitride V-shaped cantilever (*Veeco*), as depicted in **Figure 3.4.1c**, where the geometrical features of the colloidal probe are shown.



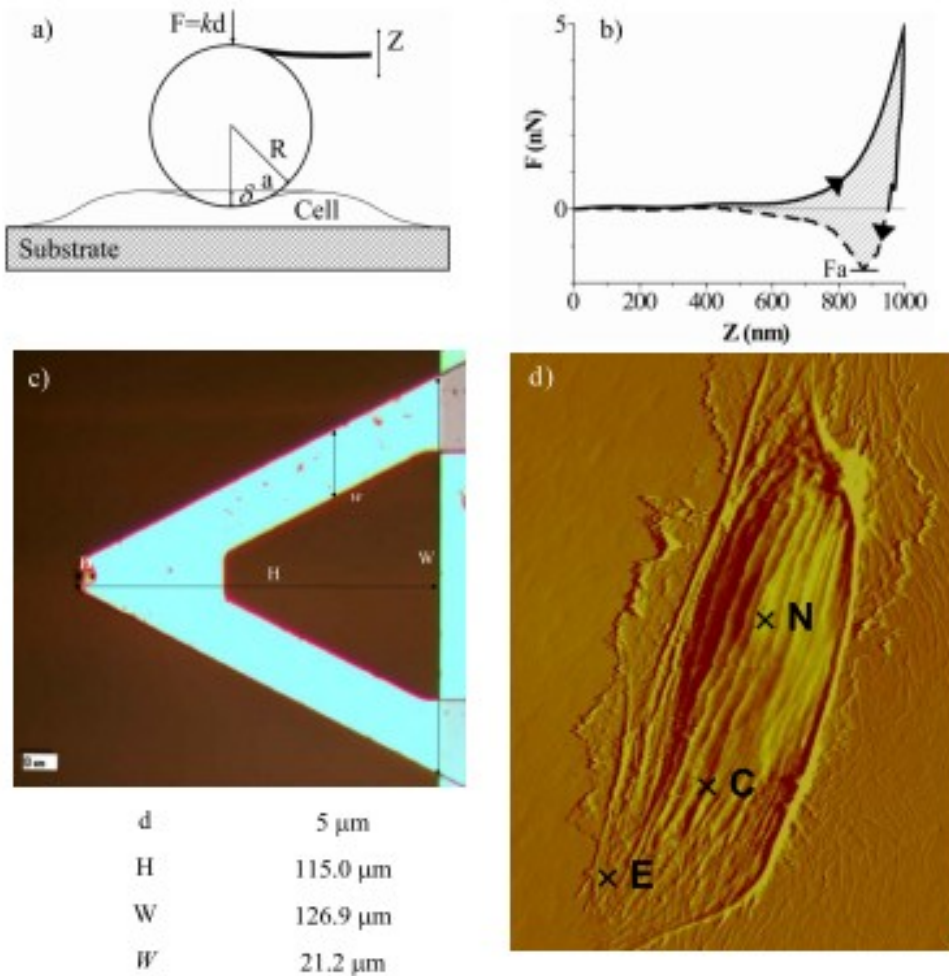


Figure 3.4.1 *Atomic force microscopy for the mechanical characterization of live cells [Lee et al 2011].*

- (a)** Schematic of the colloidal probe (spherical particle attached at the tip of a cantilever beam) interacting with the cell membrane adhering over a rigid substrate;
- (b)** A representative force–displacement curve, with a measurable force of adhesion F_a and area ratio A_v ;
- (c)** Microscopy image and geometrical data, for the V-shaped cantilever (length ‘H’, width ‘W’ and base ‘W’) with on its apex attached the colloidal probe (diameter ‘d’);
- (d)** AFM-obtained image of a single HCAEC, highlighting its different locations (N: nucleus; C: cytoplasm; E: edge), scanned alive in EBM-2 medium at room temperature (contact mode in liquid, area $XY = 120 \times 120 \mu\text{m}^2$, with pyramidal probe DNP-S [Veeco] having $f_0=12 \div 24$ kHz and $k=0.06 \text{ N/m}$).

A schematic representation of the cantilever tip interacting with a cell membrane is shown in **Figure 3.4.1a**. The relatively-large particle-size leads to larger contact-areas and more-evenly distributed contact-pressures, which limit the penetration-depth upon contact and provides average information [Iyer *et al* 2009].

The cantilever spring constant (nominal value of 0.32 N/m) was calibrated, before each experiment, using the thermal-tuning method [Butt *et al* 1995] in EBM-2 cell-culture medium, and resulted in values from 0.1 to 0.3 N/m.

For each experimental group, not less than 50 measurements were done for determining the $F-Z$ curves. Data were acquired with the Bioscope-II software (Research NanoScope software version 7.30) and analyzed as follows.

Atomic force microscopy data analysis: Young's modulus

The force F applied over the cell membrane by the colloidal probe is expressed as

$$F = kd \quad (\text{Equation 3.4.1})$$

where k and d are, respectively, the spring constant and the deflection of the cantilever (**Figure 3.4.1**).

Following the Hertzian theory [Shigley 1983], the contact radius a at the interface between the cell and the colloidal probe is expressed as

$$a = \left(\frac{3FR}{4E} \right)^{\frac{1}{3}} = \left(\frac{3kdR_2(1 - \nu_1^2)}{4E_1} \right)^{\frac{1}{3}} \quad (\text{Equation 3.4.2})$$

where E is the effective elastic modulus of the system (cell membrane–colloidal probe), defined as

$$\frac{1}{E} = \frac{1 - \nu_1^2}{E_1} + \frac{1 - \nu_2^2}{E_2} \quad (\text{Equation 3.4.3})$$

depending on the elastic moduli and Poisson's ratios of the cell membrane (E_1, ν_1) and colloidal probe (E_2, ν_2); R is the effective radius of the system, defined as

$$\frac{1}{R} = \frac{1}{R_1} + \frac{1}{R_2} \quad (\text{Equation 3.4.4})$$

depending on the radii R_1 and R_2 of the cell membrane and colloidal probe, respectively.

Introducing the penetration depth δ (**Figure 3.4.1**), **Equation 3.4.2** can be rephrased as:

$$a = \sqrt{R_2 \delta} \quad (\text{Equation 3.4.5})$$

Combining **Equations 3.4.1** and **3.4.2**, the relationship between the deflection of the cantilever d and the indentation depth δ of the probe is derived as

$$d = \eta \delta^{\frac{3}{2}} \text{ with } \eta = \frac{4E_1 R_2^{\frac{1}{2}}}{3k(1 - v_1^2)} \quad (\text{Equation 3.4.6})$$

The parameters directly-measured by operating the AFM are the cantilever beam deflection d (or, equivalently, the force $F = kd$) and the relative vertical scanner-position Z . Using simple geometrical considerations (**Figure 3.4.1**), the parameter Z is related to the penetration depth δ as

$$\delta = (Z - Z_0) - (d - d_0) \quad (\text{Equation 3.4.7})$$

where Z_0 is defined as the vertical scanner-position where the slope of the $F-Z$ curves change abruptly and d_0 is the corresponding cantilever deflection [Touhami *et al* 2003]. By using **Equations 3.4.1** and **3.4.7**, the force-displacement curves $F-Z$, directly acquired through the AFM, were turned into deflection-penetration depth curves ($d-\delta$). Through **Equation 3.4.6**, the parameter η was derived by fitting the $d-\delta$ curves.

Since the spring constant k of the cantilever, the radius R_2 of the colloidal probe and the Poisson's ratio v_1 of the cell ($v_1 = 0.5$) were fixed, the elastic modulus E_1 was readily derived from η .

For the measurement of the elastic modulus, three different approaching/retracting

velocities ($v_a = v_r = 0.25$, 0.5 and $1 \mu\text{m/s}$) and three different applied forces ($F_{max} = 0.5$, 1 and 2nN) were used. The approaching curves (solid line in **Figure 3.4.1b**) were considered for calculating the elastic modulus of the cell membrane. The maximum force applied was determined by the trigger mode of the Bioscope-II.

The relatively large colloidal-probe size leads to larger contact-area and more evenly distributed contact-pressures, limiting the probe penetration-depth inside the cell ($\approx 200\text{-}300 \text{ nm}$ in the present study) and providing averaged information, which is beneficial because of the heterogeneous nature of the cells [Iyer *et al* 2009].

Atomic force microscopy data analysis: force of adhesion

The adhesion force (F_a) at the interface between the cell membrane and the colloidal probe was also measured using the Bioscope-II, fixing the approaching velocity to $v_a = 1 \mu\text{m/s}$ and using two different retracting velocities ($v_r = 1$ and $40 \mu\text{m/s}$). The energy losses associated with the viscoelastic deformation of the cell membrane were estimated by dividing the area comprised between the approaching and retracting curves by the area associated with the approaching curve, giving the area ratio A_V .

Statistical Analysis

The Student's *t*-test was used to compare two groups. One-way ANOVA with repeated measurements was used for multiple comparisons. Significance was assumed for $p < 0.01$. The data and errors are expressed as means \pm SD.

3.4.3 Main results and discussion

Effects of TNF- α stimulation on the apparent elastic modulus

The apparent compressive elastic moduli were calculated by analyzing the force–displacement curves obtained through AFM following the Hertzian contact theory, as described in Section 3.4.2. The same procedures were applied to all three ECs in both the un-stimulated (control) and stimulated conditions.

A typical force–displacement curve is shown in **Figure 3.4.1b**, where the dashed line corresponds to the approaching curve and the solid line to the retracting curve. The curves were measured over relatively-flat regions of the cell membrane (point C in **Figure 3.4.1d**) [Iyer *et al* 2009], always sufficiently far from the cell nucleus (point N in **Figure 3.4.1d**) and edge (point E in **Figure 3.4.1d**). The force–displacement curves were recorded in the same location of the cell, and the apparent elastic modulus were very consistent, exhibiting small standard deviations over multiple measurements. All the force–displacement curves were obtained for an indentation force of 0.5 nN and an approaching/retracting probe velocity of 0.25 μ m/s. For such small values of force and velocity, the assumptions of the Hertzian theory are fully satisfied [Mathur *et al* 2001]: the indentation depth was always smaller than 200nm (sufficiently smaller than the thickness of the cell), and the visco-elastic response of the cell membrane was negligible. The presence and the morphology of the cell under the probe were monitored *in situ* through an optical inverted microscope.

The apparent elastic moduli for the three cell lines are presented in the bar chart of **Figure 3.4.2**, for both un-stimulated (white bars) and stimulated (dark bars) conditions.



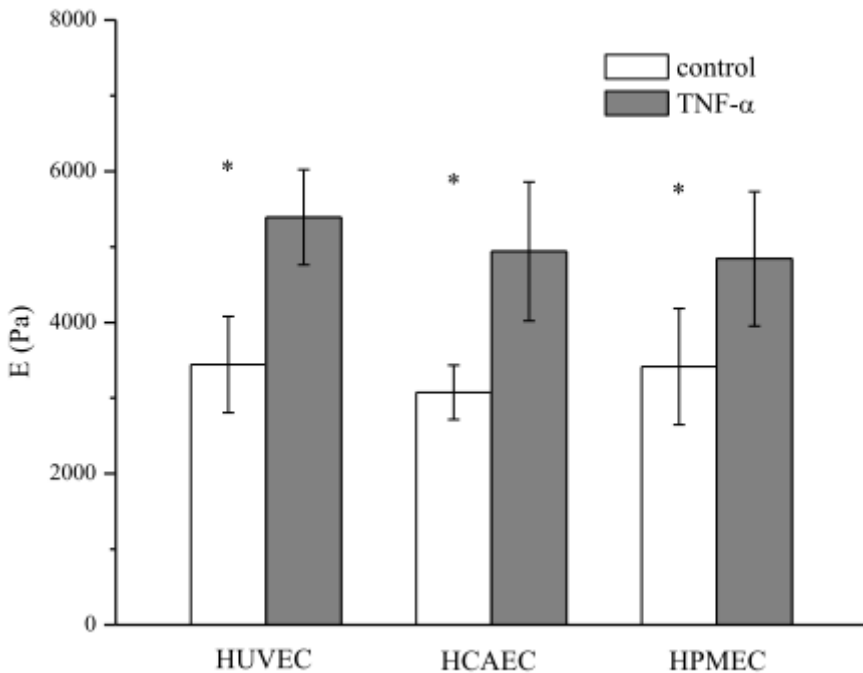


Figure 3.4.2 Apparent elastic modulus for three different endothelial cell lines [Lee *et al* 2011].

Bar chart presenting the apparent elastic modulus E for HUVEC, HCAEC and HPMEC under un-stimulated (control) and stimulated (20h with 10 ng/ml TNF- α) conditions. * means $P < 0.05$.

Operating parameters used: $F_{max} = 0.5$ nN; $v_a = v_r = 0.25$ $\mu\text{m}/\text{s}$; number of cells $n = 3$; repetitions per cell $N > 30$.

The apparent elastic modulus E for the three ECs presented in the bar chart of **Figure 3.4.2** is explicitly listed in **Table 3.4.1**.

Cell type and Condition			Apparent Elastic Modulus [kPa]
HUVEC	un-stimulated	n=42	3.44 ± 0.64
	TNF- α stimulated	n=46	5.39 ± 0.63
HCAEC	un-stimulated	n=20	3.07 ± 0.36
	TNF- α stimulated	n=21	4.94 ± 0.92
HPMEC	un-stimulated	n=38	3.42 ± 0.77
	TNF- α stimulated	n=20	4.84 ± 0.89

Table 3.4.1 Data in tabular form of **Figure 3.4.2** [Lee *et al* 2011].

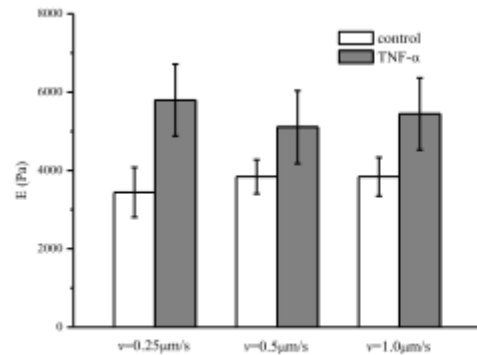
Results are presented as mean \pm SD, and the number of repetitions n is also listed.

It was measured $E = 3.44 \pm 0.64$ kPa for the HUVECs, $E = 3.07 \pm 0.36$ kPa for the HCAECs and $E = 3.42 \pm 0.77$ kPa for the HPMECs in the un-stimulated condition. There was no statistically-significant difference between the apparent elastic moduli of the three ECs ($p > 0.1$), which give an average of $E = 3.31 \pm 0.35$ kPa. These results are in good agreement with other analysis available in the literature, conducted on human ECs following the same procedures used here [Kataoka *et al* 2002, Mathur *et al* 2001, Mathur *et al* 2000]. Slightly larger values for E were measured by Kang and colleagues [Kang *et al* 2008]. Also, these results confirm that cells performing similar functions (endothelial cells) but located in different organs do exhibit the same apparent elastic modulus and, consequently, similar cytoskeletal organization.

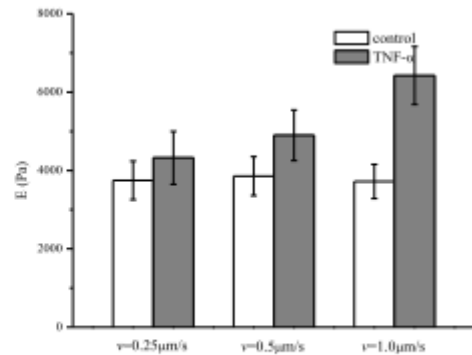
About 20 hours after stimulation with TNF- α , force-displacement curves were recorded and analyzed to derive the following apparent elastic moduli: $E = 5.39 \pm 0.63$ kPa for the HUVECs, 4.72 ± 1.15 kPa for the HCAECs and 4.84 ± 0.89 kPa for the HPMECs. Compared to the un-stimulated cells, a statistically-significant ($p < 0.01$) increase in the apparent modulus was observed for all cell lines, with a ratio (E_s/E_u) between stimulated (E_s) and un-stimulated (E_u) cells of 1.54, 1.42 and 1.56 respectively for HCAECs, HPMECs and HUVECs. In other words, an increase in cell stiffness of about 50% was observed upon stimulation with 10 ng/ml of TNF- α over 20 hours, leading to an average $E = 4.98 \pm 0.53$ kPa.

The measurement of the apparent elastic modulus is influenced by the force applied over the cell membrane, the velocity of the probe and, consequently, the depth of penetration

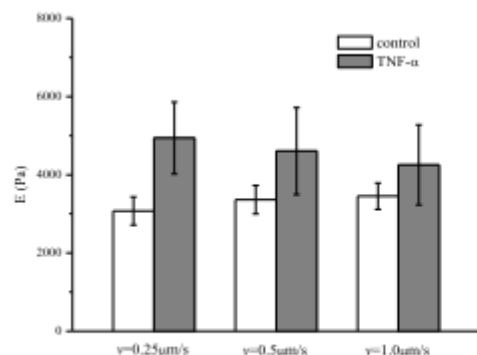
of the probe. Therefore, a sensitivity analysis was performed on E by varying the indentation force F_{max} between 0.5 and 2 nN and the indentation velocity ($v_a = v_r$) between 0.25 and 0.1 $\mu\text{m/s}$. The results of such analysis, summarized in **Figure 3.4.3**, confirmed the importance of reducing F_{max} and v for accurately estimating the compressive modulus. The penetration depth in all the experiments was smaller than 200 nm.



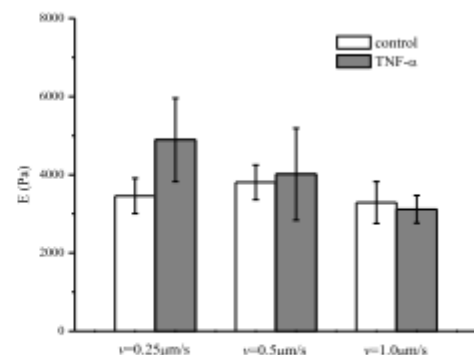
HUVEC ($F=0.5\text{nN}$)



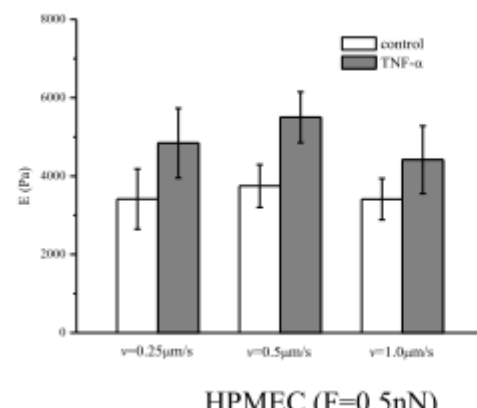
HUVEC ($F=1.0\text{nN}$)



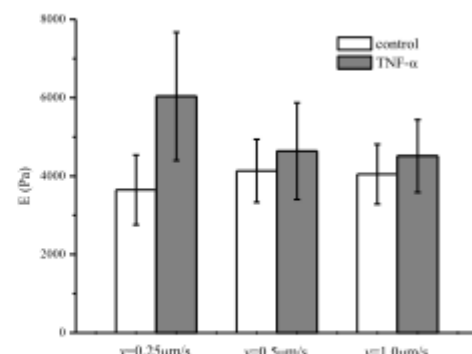
HCAEC ($F=0.5\text{nN}$)



HCAEC ($F=1.0\text{nN}$)



HPMEC ($F=0.5\text{nN}$)



HPMEC ($F=1.0\text{nN}$)

Figure 3.4.3 Effect of the indenting force and velocity on the apparent elastic modulus [Lee et al 2011].

Operating parameters used: $F_{max}= 0.5$ and 1.0 nN; $v_a = v_r = 0.25, 0.5, 1 \mu\text{m}/\text{s}$.

Different methods have been proposed, in addition to atomic force microscopy, to extract the mechanical properties of cells, such as magnetic [Bausch *et al* 1999] and optical [Wei *et al* 2008] tweezers, micropipettes [Sato *et al* 1990]. Generally, the methods and the procedures affect the final measure, giving different values for the mechanical stiffness for even the same cell. Nonetheless, it is here important to emphasize that the present work aims at a comparative analysis rather than to an absolute measurement of the cellular mechanical properties.

The response to TNF- α stimulation was also documented by analyzing the reorganization of the actin filaments within the cytoskeleton and the over-expression of the adhesive molecules ICAM-1. The staining of the actin filaments with Alexa Fluor 488 phalloidin was observed over three different planes –namely apical, median and basal– using confocal fluorescent microscopy. **Figures 3.4.4÷6** show the results for the HPMECs, HUVECs and HCAECs respectively, in the un-stimulated (left columns) and TNF- α -stimulated (right columns) conditions. Upon stimulation with TNF- α , the fluorescence intensity associated with the actin filaments increases over the median and apical cell planes.

More in detail, for the un-stimulated HPMECs, dense and thick actin filaments were observed on the basal and median plane transversing the whole cell, whereas on the apical plane the filaments were mostly located at the edge of the cell (**Figure 3.4.4** – left column). Upon stimulation with TNF- α , the fluorescence intensity associated with the actin filaments increased over the median and mostly over the apical plane, where dense and thick filaments crossing the whole cells were clearly visible (**Figure 3.4.4** – right column). Similar results were observed in the case of the HCAEC and HUVEC, as shown in **Figures 3.4.5** and **3.4.6** respectively. The same exposure time and acquisition settings were used for all the images.

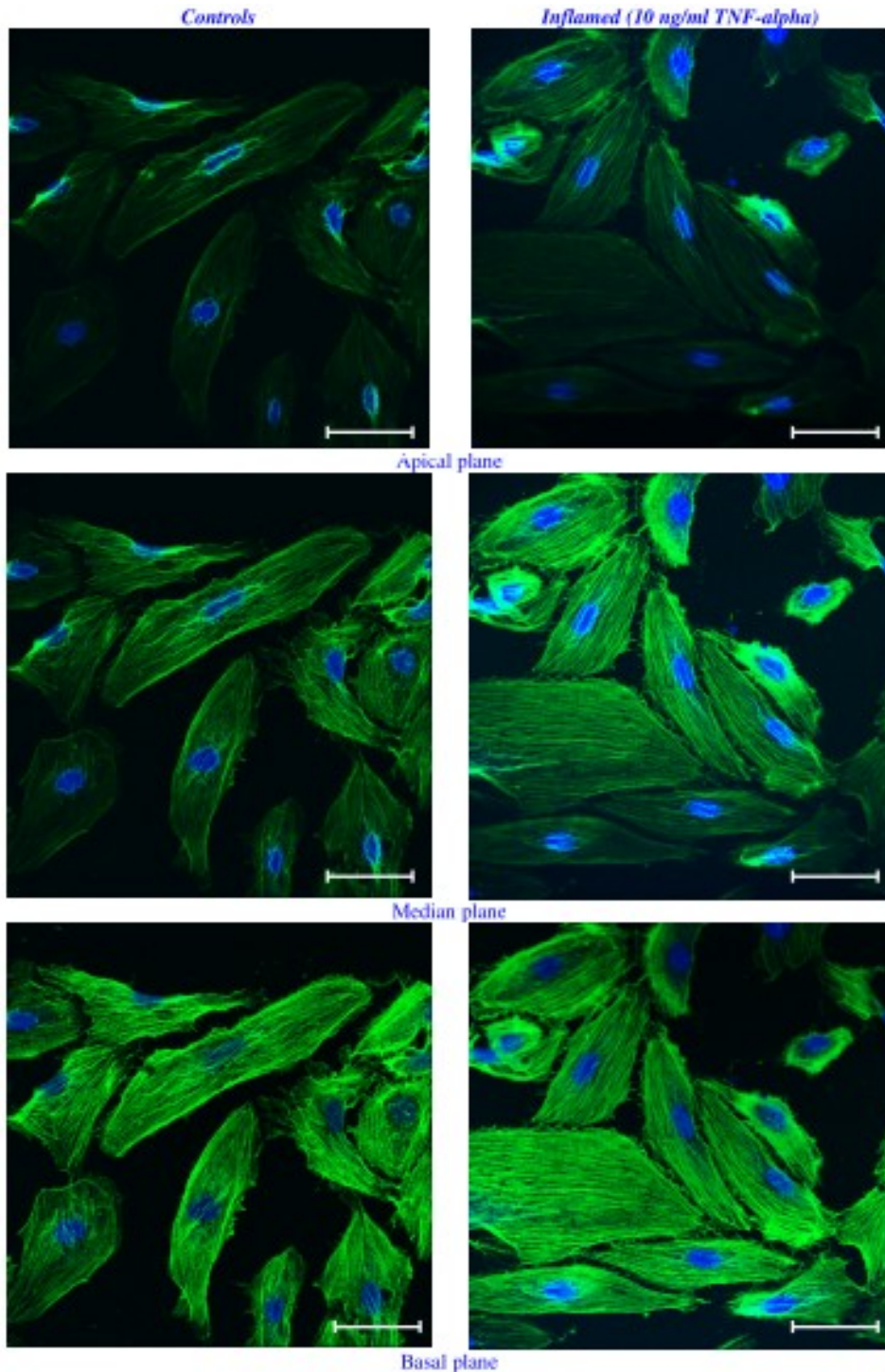


Figure 3.4.4 Fluorescent microscopy of F-actin organization of HPMECs [Lee et al 2011].

The left column shows the un-stimulated HPMECs (control) and the right column the HPMECs stimulated with 10 ng/ml TNF- α for 20 h, over three different confocal planes, namely apical, median and basal. In green are the actin filaments (Alexa Fluor 488–phalloidin staining) and in blue the cell nuclei (TO-PRO-3 staining). All scale bars are 50 μ m.

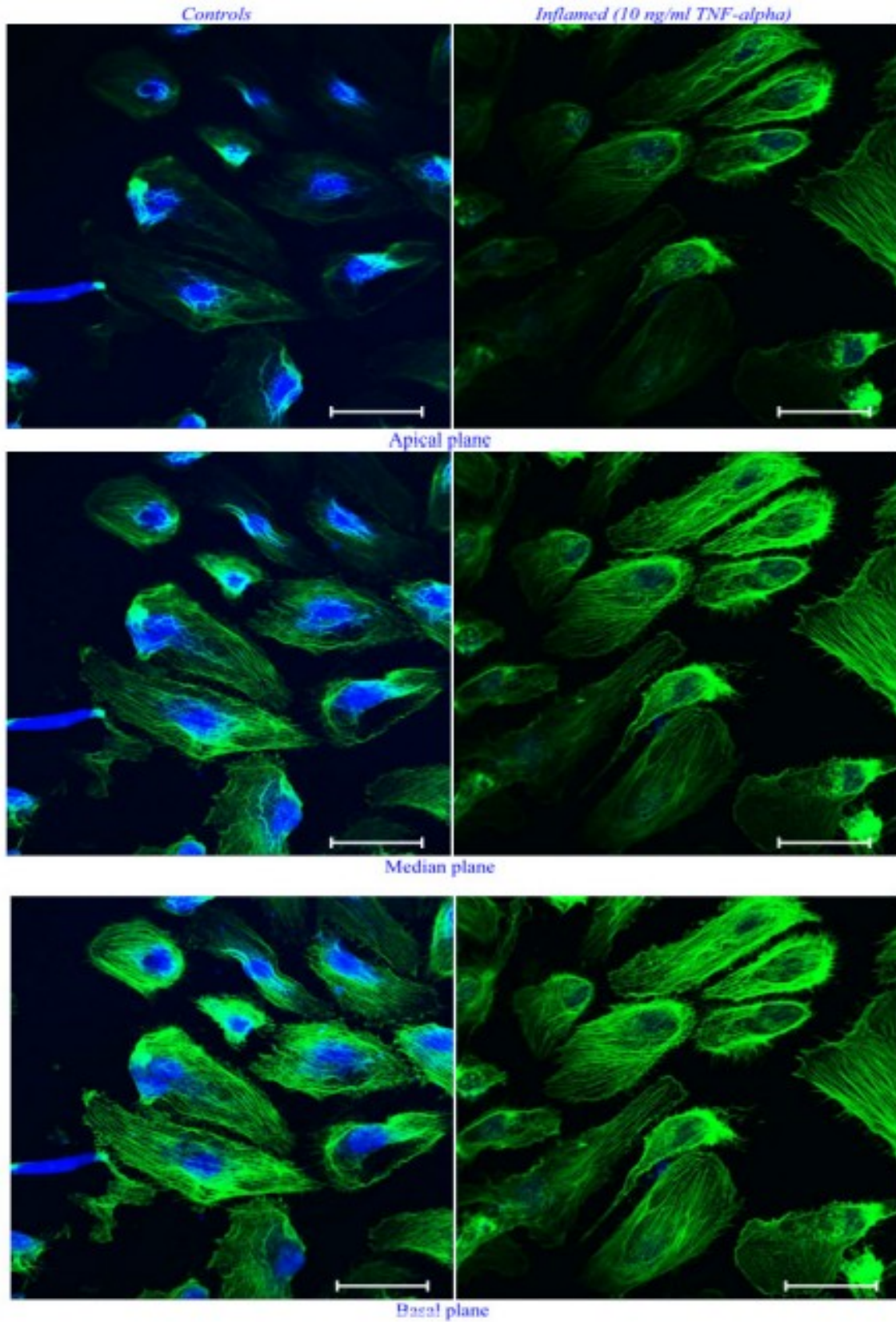


Figure 3.4.5 Actin staining of HUVECs, equivalent of **Figure 3.4.4** [Lee et al 2011].

Tommaso Novellino

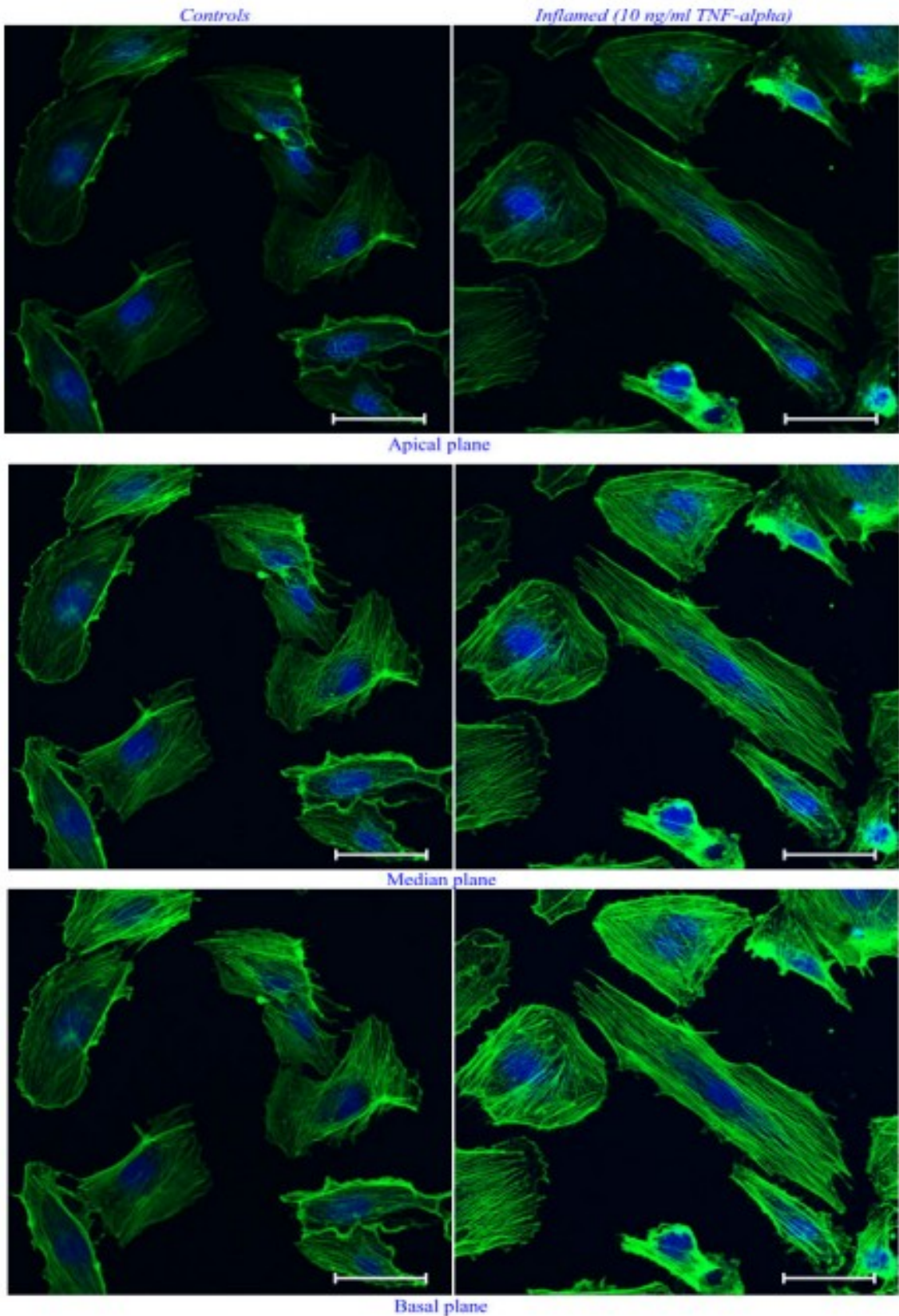


Figure 3.4.6 Actin staining of HCAECs, equivalent of **Figure 3.4.4** [Lee et al 2011].

The actin filaments are known to form a network under the cell membrane, providing mechanical strength, and to undergo extensive remodeling and reorganization upon TNF- α stimulation [Campos *et al* 2009, Petrache et al 2003, Wójciak-Stothard et al 1998]. The observed increase in filament density could explain the higher stiffness of the stimulated cells as compared with the controls.

Also, the level of expression of ICAM-1 was measured through ELISA, demonstrating a statistically-significant increase in the surface density for these adhesive molecules (**Figure 3.4.7**), normally over-expressed on the inflamed endothelium [Danila *et al* 2009]. The increased expression of ICAM-1 molecules was also shown through immunostaining: **Figure 3.4.8** shows the immunostaining for ICAM-1 for the three ECs considered.

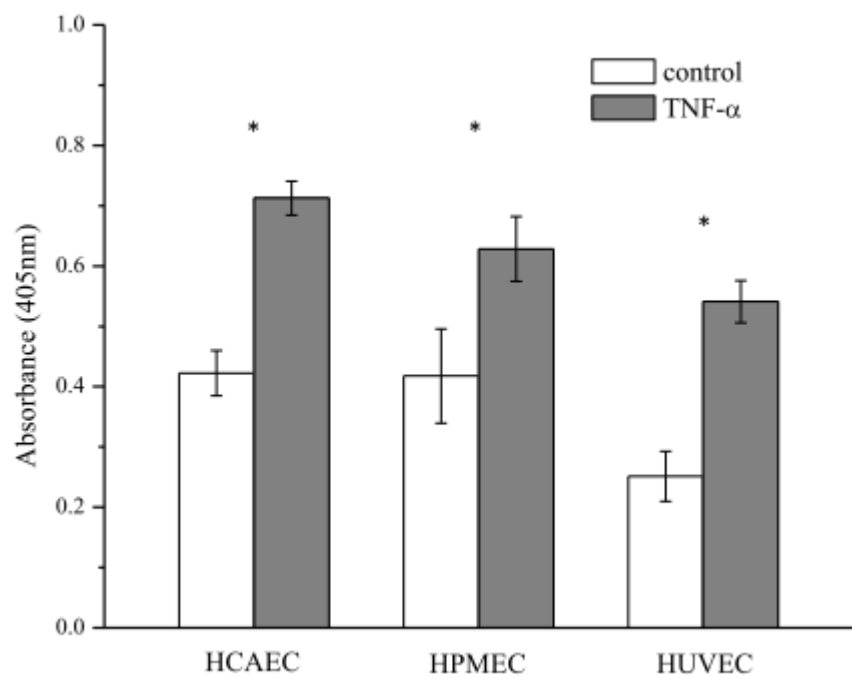


Figure 3.4.7 Expression of adhesive molecules ICAM-1 measured through ELISA test [Lee *et al* 2011].

Bar chart presenting the expression of ICAM-1 molecules in un-stimulated cells (white bars) and cells stimulated with 10 ng/ml TNF- α for 20 h (grey bars). * means $P < 0.01$.

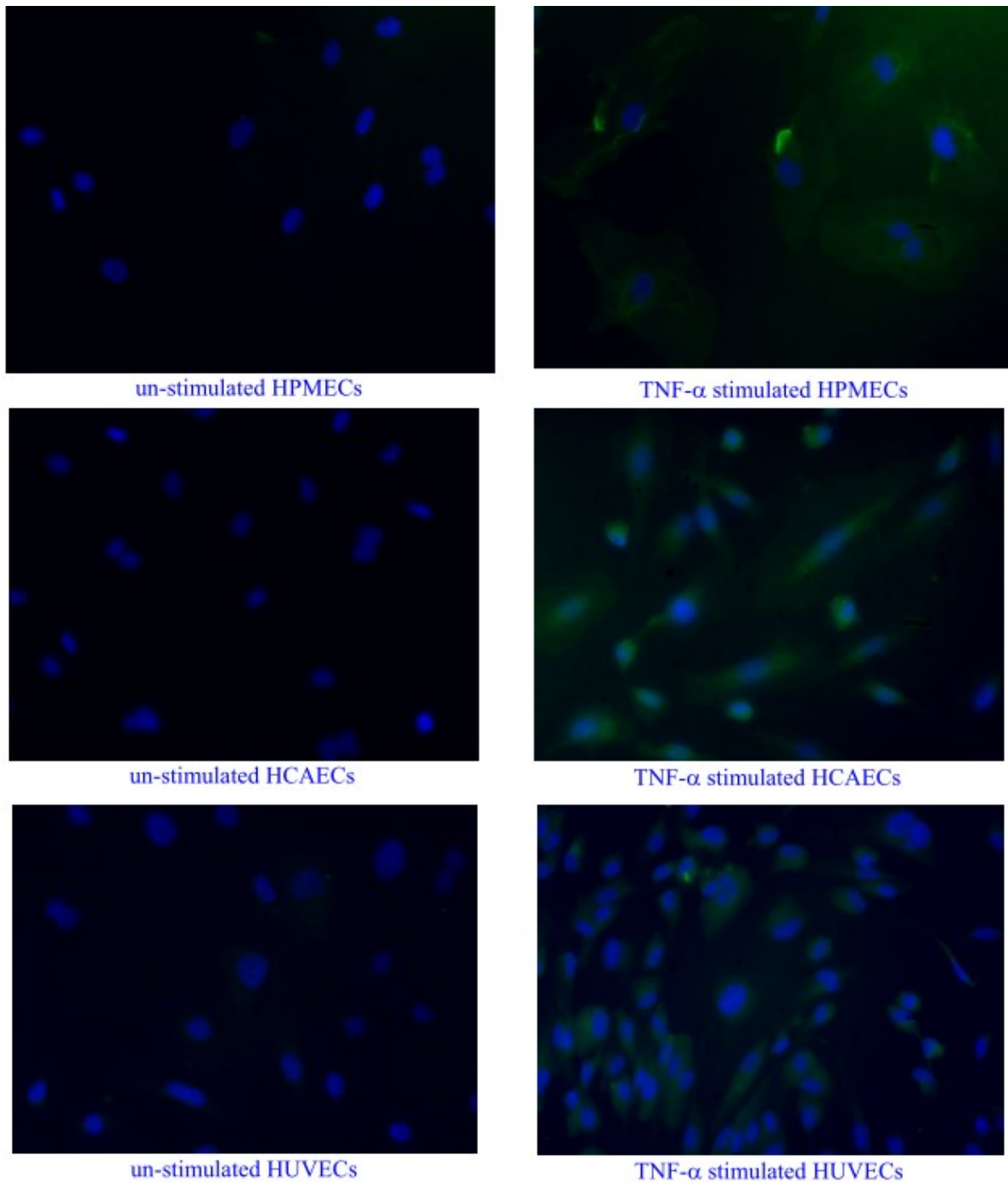


Figure 3.4.8 Immuno-staining for the ICAM-1 receptors [Lee et al 2011].

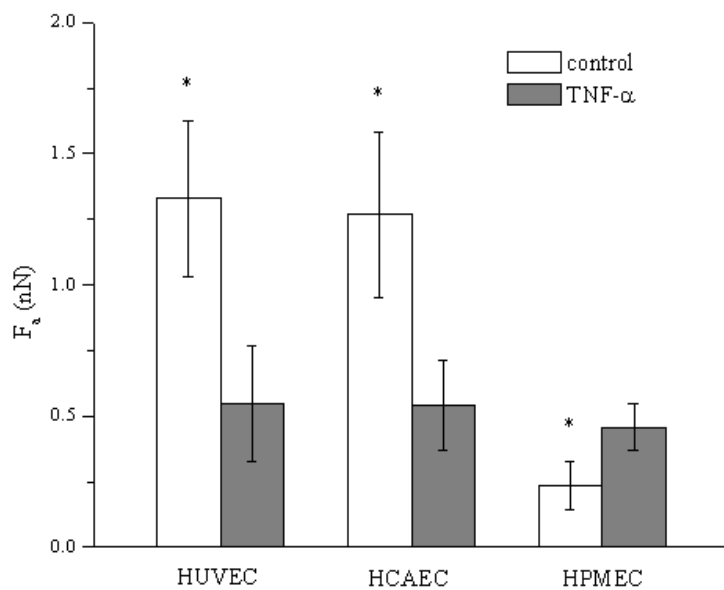
Effects of TNF- α stimulation on the force of adhesion and viscoelastic response

In addition to the apparent elastic modulus, the adhesive force at the interface between the

colloidal probe and the cell membrane and the viscoelastic response of the cell were recorded, following [Attard 2007]. The force of adhesion F_a was estimated as the maximum force measured along the retracting curve (**Figure 3.4.1b**); whereas the viscoelastic response was quantified as the ratio (A_V) between the energy dissipated due to viscoelastic losses (area between the approaching and retracting curves – dashed area in **Figure 3.4.1b**) and the overall mechanical work performed (area under the approaching curve).

Since the AFM probe was not decorated with any ligand molecule, interfacial adhesion was only associated with weak non-specific interactions. This was reflected by the negligibly small values of F_a ($\ll 1$ nN) measured with low indentation forces F_{max} ($= 0.5$ nN) and velocities $v_a = v_r$ ($= 0.25$ $\mu\text{m/s}$). In all experiments, the retracting curves appeared as continuous, with no noticeable abrupt jumps generally associated with the breakage of specific molecular bonds, thus confirming the non-specific nature of the forces at the probe-cell interface. Therefore, in order to generate appreciable adhesive forces and viscoelastic losses, the indentation force and the retracting velocity were increased up to $F_{max} = 5$ nN and $v_r = 40$ $\mu\text{m/s}$, respectively. The results obtained with those new experimental parameters are presented in **Figure 3.4.9**.

a)



b)

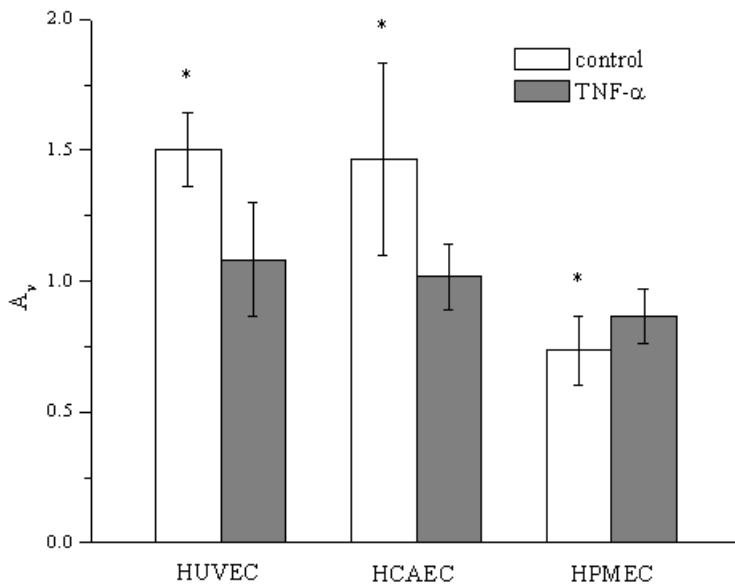


Figure 3.4.9 Adhesion force and viscoelastic response of the three different endothelial cell lines [Lee et al 2011].

The force of adhesion F_a (a) and the area ratio A_v (b) for three different cell lines (HUVEC, HCAEC and HPMEC) under un-stimulated (control) and stimulated (20h with 10 ng/ml TNF- α) conditions. * means $P < 0.05$.

Operating parameters used: $F_{max} = 5$ nN; $v_r = 40$ $\mu\text{m}/\text{s}$; number of cells $n = 3$; repetitions per cell $N > 30$.

Tommaso Novellino

Figure 3.4.9 shows the force of adhesion F_a and the area ratio A_v , defined as above, for the three ECs under un-stimulated (white bars) and stimulated (grey bars) conditions.

The data of **Figure 3.4.9** are explicitly listed in **Table 3.4.3**.

Cell type and Condition		Force of Adhesion F_a [nN]		Area ratio A_v
HUVEC	un-stimulated	1.32 ± 0.30 nN	n = 146	1.50 ± 0.14
	TNF- α stimulated	0.55 ± 0.22 nN	n = 150	1.08 ± 0.22
HCAEC	un-stimulated	1.26 ± 0.31 nN	n = 150	1.47 ± 0.37
	TNF- α stimulated	0.54 ± 0.17 nN	n = 150	1.02 ± 0.13
HPMEC	un-stimulated	0.24 ± 0.09 nN	n = 150	0.74 ± 0.13
	TNF- α stimulated	0.46 ± 0.09 nN	n = 150	0.87 ± 0.10

Table 3.4.3 The force of adhesion (F_a) and the area ratio (A_v) data for the three ECs [Lee et al 2011].

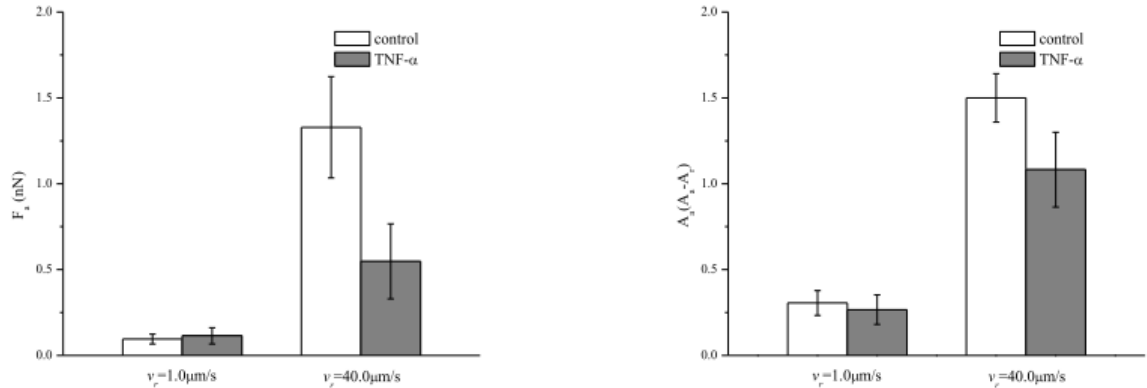
Results are presented as mean \pm SD and the number of repetitions n is also listed.

For the un-stimulated HUVECs and HCAECs, an adhesion force (area ratio A_v) of 1.32 ± 0.30 nN (1.50 ± 0.14) and 1.26 ± 0.31 nN (1.47 ± 0.37) were measured, respectively. For these two cell-lines there was no statistically-significant difference ($p > 0.03$) and their values were significantly larger than the adhesion force (area ratio) estimated for the un-stimulated HPMECs, having a value of 0.24 ± 0.10 nN (0.74 ± 0.13). It is interesting to observe that, under physiological conditions, the viscoelastic losses associated with the endothelial cells of the pulmonary microvasculature are about 50% smaller than those associated with the umbilical and coronary endothelial cells. Indeed, the lung microvasculature is continuously subjected to compressions and expansions, following the respiratory cycle, and a smaller area ratio A_v would imply lower viscoelastic losses.

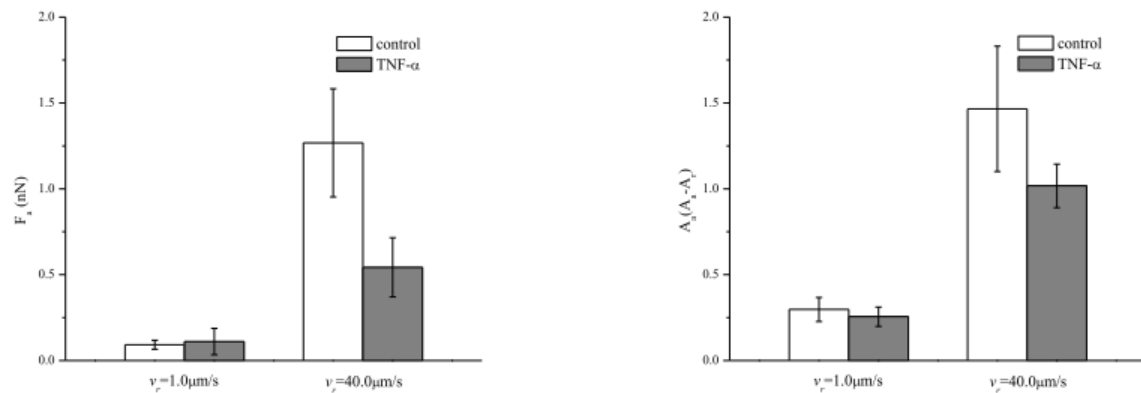
More interestingly, for the stimulated ECs, the force of adhesion F_a (area ratio A_v) was similar for all cell lines ($p > 0.01$) being, respectively, 0.55 ± 0.22 nN (1.08 ± 0.22) for

the HUVECs, 0.54 ± 0.17 nN (1.02 ± 0.13) for the HCAECs and 0.46 ± 0.09 nN (0.74 ± 0.13) for the HPMECs. The force of adhesion and viscoelastic losses for the HUVECs and HCAECs decreased significantly (50%) upon stimulation with TNF- α , whereas an opposite trend was observed for the HPMECs. In **Figure 3.4.10**, a sensitivity analysis is presented elucidating the effect of the retracting velocity on the force of adhesion and viscoelastic losses. It is confirmed that the viscoelastic response of the cell membrane decreases as the retracting velocity reduces.

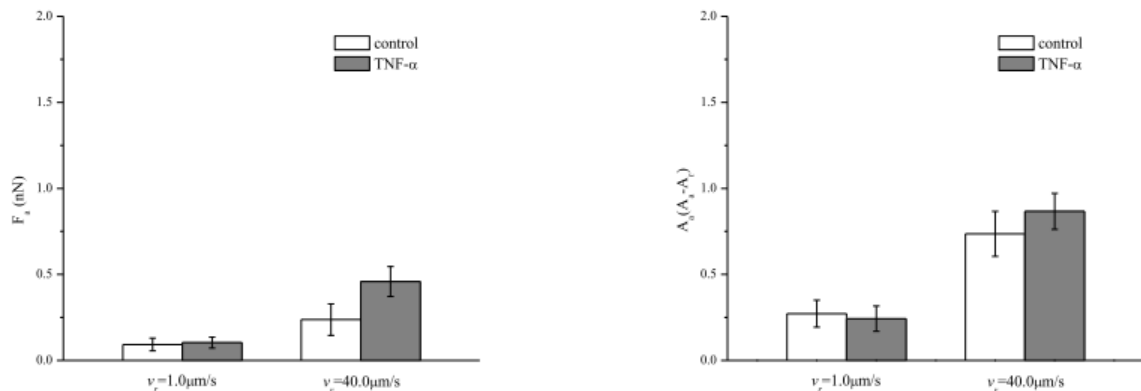




HUVEC



HCAEC



HPMEC

Figure 3.4.10 Effect of the retracting velocity (v_r) on the force of adhesion [Lee et al 2011].

Operating parameters used: $F_{max} = 5$ nN; $v_a = 1 \mu\text{m/s}$; $v_r = 1 \mu\text{m/s}$ and $40 \mu\text{m/s}$.

3.4.4 Conclusions

TNF- α is a pro-inflammatory cytokine secreted primarily by macrophages and endothelial cells during an inflammatory response [Old 1985]. However, it is becoming clear that other cells can as well release in the tissue and eventually in the circulation large amounts of TNF- α , including: lymphoid cells, mast cells, cardiac myocytes, adipose tissue, fibroblasts and neuronal tissue [Old 1985, Pennica *et al* 1984].

The physiological plasma concentration of TNF- α is smaller than 1 pg/ml. However under pathological conditions, a substantial increase was documented depending on the patient, type and stage of the pathology. In **Table 3.4.4**, the TNF- α plasma concentrations are listed for several different pathologies. Indeed, high plasma level of TNF- α are known to be toxic [Lejeune *et al* 2006] and could lead to vascular dysfunction.

Pathology	Plasma level of TNF-α [pg/mL]
Physiological conditions	<1.0
Rheumatoid arthritis	1000
Atherosclerosis	1000–2000
Colorectal cancer	2
Pancreatic adenocarcinoma	30
Non-small cell lung cancer	10
Chronic lymphocytic leukemia	20
Prostate cancer	4
Metastatic prostate cancer	6
Breast cancer	5
Pre-eclampsia	200
Obesity	10
Hemorrhagic shock alone	60
Hemorrhagic shock with subsequent MOF	160

Table 3.4.4 List of the most common pathologies presenting higher levels of circulating TNF- α and corresponding concentration [Lee et al 2011].

Based on the presented AFM characterization and cytokine response of three different ECs, it is tempting to speculate that relatively-low, non-physiological concentrations of circulating TNF- α (< 1÷10 ng/ml, much smaller than the maximum tolerable dose) over a sufficiently long time (from months to years) could be responsible for a progressive systemic alteration of the endothelium with an increase in cell stiffness and vascular permeability. Systemic vascular dysfunction could be the minimum common denominator for several apparently unrelated diseases, as rheumatoid arthritis, atherosclerosis, tumor progression and metastatization, pre-eclampsia, obesity and trauma, which are associated with high circulating levels of TNF- α .

Additional studies are needed to better characterize the response of the endothelial cells to TNF- α , including, in particular, the contribution of continuous blood flow. ECs exposed to continuous hydrodynamic shear stresses increase their stiffness over time [Mathur et al 2007], and this has been associated with an increase in actin fiber density primarily on

the basal plane. Differently, TNF- α stimulation was here observed to alter the actin density mainly at the apical and median planes. These observations would support a cooperative contribution of hydrodynamic shear stresses and TNF- α in cell stiffening. However, specific experiments should be designed to better analyze this issue.

In conclusion, the mechanical properties of three different cell lines (HUVECs, HCAECs and HPMECs) were analyzed before and after stimulation with the pro-inflammatory cytokine TNF- α . The analysis revealed that: (i) before stimulation with TNF- α , no significant difference exists in terms of apparent compressive modulus among the three vascular districts tested, with an average $E = 3.30 \pm 0.35$ kPa; (ii) upon stimulation with TNF- α , the stiffness of the ECs increases by about 50%, reaching an average $E = 5 \pm 0.5$ kPa; (iii) before stimulation with TNF- α , the viscoelastic losses in the pulmonary microvasculature are about 50% lower than in the other two districts considered, for which no statistically-significant difference was observed; (iv) upon stimulation with TNF- α , the viscoelastic losses become statistically similar in all three vascular districts. This study demonstrates that the *in vitro* response to TNF- α stimulation is independent of the vascular district. The observed increase in mechanical stiffness could be related to the larger density and thickness of the actin fibers observed mainly on the apical and median cell planes. These results provide additional information for unraveling the possible correlations between circulating pro-inflammatory cytokines, as TNF- α , and systemic vascular dysfunction.

3.4.5 Acknowledgements of Section 3.4

I acknowledge the following people contributions:

- General-idea conceiving, supervision: Paolo Decuzzi, Jodie Conyers
- Experimental design and planning: Tommaso Novellino, Paolo Decuzzi, Sei-Young Lee
- AFM measurements: Tommaso Novellino, Sei-Young Lee, Ana Maria Zaske
- Cell inflammation and ELISA-measurements: Delia Danila
- Cellular staining: Ana Maria Zaske
- Confocal measurements: Tommaso Novellino
- Cell culture: Eva Golunski
- Data analysis and statistics: Tommaso Novellino, Sei-Young Lee
- Results discussion and interpretation: Tommaso Novellino, Paolo Decuzzi, Sei-Young Lee.

3.5 Influence of internalized nanoparticles on cytoskeleton organization

3.5.1 Gold nanoparticles

Biological applications/interactions

Functional nanomaterials have recently attracted strong interest from the biology community, not only as potential drug delivery vehicles or diagnostic tools but also as optical nanomaterials. Particular interest have gained the intracellular delivery of nanoparticles in order to attain proper cellular applications, a field where rigorous and quantitative characterization of the uptake and the fate of the nanoparticles are critical variables of the cells–nanoparticles interacting system [Levy *et al* 2010].

One intensively-studied functional nanomaterial are the gold nanoparticles, which have emerged as nano-scaled systems attractive for biological and biomedical applications because of their physical and chemical properties [Jain *et al* 2008], as depicted in **Figure 3.5.1**.

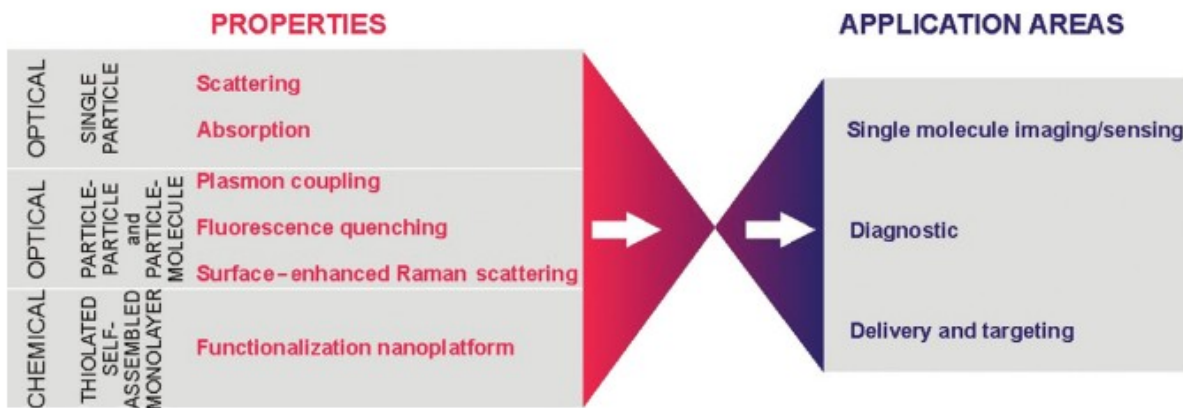


Figure 3.5.1 Properties and potential-applications of gold nanoparticles in biology and medicine [Levy *et al* 2010].

Gold has been long-considered inert and essentially non-toxic to cells [Connor *et al* 2005]; anyway, as it will be discussed later on, this is controversial in the recent literature.

Optical properties

The gold nanoparticles absorb and resonantly-scatter visible and near-infrared light upon excitation of their surface plasmon oscillation. The plasmon resonance band can be tuned over a wide spectral range by changing intrinsic parameters such as the material (bi-metallic or hybrid particles), the size, the shape (sphere, rod, cube, triangle, cage, etc.) [Sonnichsen *et al* 2002].

The light-scattering signal is intense and much brighter than chemical fluorophores and does not photo-bleach or blink [Yguerabide *et al* 1998]. This constitutes an advantage for their applications in single molecule imaging, where the use of dyes, fluorophores, or quantum dots is limited by low signal intensities, complex blinking phenomena, and photo-bleaching.

For particles below 30 nm, the absorption becomes dominant over scattering and can be used for detection by photo-thermal microscopy [Boyer *et al* 2002].

Particles synthesis

Gold nano-particles with varying core size are prepared by the reduction of gold salts in the presence of stabilizing agents to prevent nanoparticle agglomeration and control growth [Goubet *et al* 2009]. Particle suspensions are also commercially available.

Furthermore, gold nanoparticles can be easily functionalized by anchoring thiol-linkers in their monolayers. A wide variety of functional bionanoconjugates has been obtained, including nanoparticles modified with peptides, proteins, antibodies, oligosaccharides, nucleic-acids [Boisselier *et al* 2009, Sperling *et al* 2008]. This allows the nanomaterials to act as multifunctional platforms for both therapeutic and diagnostic purposes.

Biomedical applications

The use of functionalized gold nanoparticles for biological and biomedical applications includes bio-imaging, single-molecule tracking, biosensing, drug delivery, transfection, diagnostic [Levy *et al* 2010].

For example, through proper functionalization, the particles can be engineered to accumulate-preferentially in tumor cells using targeting ligands, providing a tool for cancer diagnosis and gene therapy [El-Sayed *et al* 2005].

Sensor arrays have been developed to differentiate normal, cancerous, and metastatic cells using the fluorescence quenching properties of gold nanoparticles [Bajaj *et al* 2009].

The interactions and fate of a broad range of functionalized nanoparticles is currently under investigation in a wide diversity of biological models, ranging from whole organisms to tissues to cells in culture, and also to yeast [Maheshwari *et al* 2010] and prokaryote bacteria [Amin *et al* 2009].

The needs of intracellular delivery depend on the applications. For cancer-cell targeting and killing, the requirement is proper cell recognition and uptake independently of the ultimate localization (e.g. vesicular localization is not a problem in this context). However, for intracellular imaging and sensing, cell recognition is less important, whereas the ultimate intracellular localization of the nanomaterial is crucial and needs to be fully addressed. Many biomedical applications will ultimately necessitate a targeted intracellular delivery and availability of the nanomaterial, not only to specific cells, but also to specific subcellular compartments. Currently, the main challenge is to avoid endosomal localization and to control the stability of the functional capping after cellular uptake [Levy *et al* 2010].

Non-specific cellular uptake

The cell plasma-membrane defines the separation between the interior of the cell and its outside environment. It is semi-permeable, and allows free-diffusion of small and non-polar molecules. However, bigger objects such as nanomaterials are incapable of crossing the plasma-membrane and require uptake mechanisms such as endocytosis [Doherty *et al* 2009, Conner *et al* 2003].

Most gold nanoparticle bioconjugates are easily taken up by the cells through endocytotic mechanisms. Although endocytotic uptake is the norm for a broad range of nanomaterials, its efficiency is dependent on the nanoparticle surface chemistry and the physical properties (size and shape) of the material [Levy *et al* 2010]. Particularly, positively-charged nanoparticles are known to have a favored endocytic entry into the cells. Indeed, anionic molecules and structures bind less efficiently to cell surfaces than neutral or cationic molecules because of the electrostatic repulsion between the negatively-charged surface

membrane and cellular environment; that is the reason why, for e.g., positively-charged liposomes are commonly used for transfecting molecules into cells [Chithrani *et al* 2006].

In spite of the increasing number of published papers, controlling the intracellular delivery, fate, localization of nanoparticles remains a major challenge; even simple questions such as the effect of nanoparticle surface (charge, chemical-functionalization), shape, size are still controversial [Levy *et al* 2010]. This may be related to the complex and powerful mechanisms that cells use to protect themselves from foreign materials and organisms.

Bio-toxicity

Regarding the biological toxicity of nanoparticles in general, both *in-vivo* and *in-vitro* experiments demonstrate that exposure to small nanoparticles is associated with inflammation, with particle size and composition being the most important factors [Buzea *et al* 2007].

Anyway, there are many contradictory results related to the toxic effects of nanoparticles at different concentrations. Some studies show that certain materials are not as toxic as was observed by other studies.

One explication for the above phenomenon is that, when comparing the results of different studies, one must take into account that there are differences in the aggregation properties of nanoparticles in air and water, resulting in inherent discrepancies between inhalation studies and instillation or in vitro experiments. The aggregation may depend on surface-charge, material-type, size among others. Nanoparticles aggregation is essential in determining their toxicity, due to a more effective macrophage-clearance for larger particles compared to smaller ones (that seem to evade easier this defense mechanism), leading to reduced toxicity of nanoparticle-aggregates larger than 100÷200 nm [Oberdorster *et al* 2005, Takenaka *et al* 2001]. It has been demonstrated that a high concentration of nanoparticles would promote particle aggregation [Gurr *et al* 2005, Churg *et al* 1998], and therefore reduce toxic effects compared to lower concentrations [Takenaka *et al* 2001]. Most aggregates are observed to be larger than 100 nm, a size that seems to be a threshold for many of the adverse health effects of small particles. Therefore, experiments performed with high concentrations of nanoparticles will lead to the formation of nanoparticle aggregates that may not be as toxic as lower concentrations of the same nanoparticles [Buzea *et al* 2007].

3.5.2 Experimental methods

Human cells and gold nanoparticles

Human pulmonary microvascular endothelial cells (HPMECs) were purchased (*Promocell*) and cultivated with standard protocols. Nano-sized spherical particles, of different diameters (namely, 100 and 30 nm), were commercially purchased (*Nanopartz* and *NanoCs*, respectively). Relatively-young cells (passage 2÷5) were subcultivated for at least few days before being seeded in 8-well slide chambers (*ThermoFisher Scientific*) at a number (16000 cells/well) in order to obtain 80% confluence. After 24h from seeding, the cells were incubated for 24h (37°C, 5% CO₂) with different particle sizes and concentrations (0, 0.1, 0.2, 0.5 mg/ml). Cells without particles were taken as controls. After incubation, cells were probed by Atomic Force Microscopy (AFM), imaged by optical microscopy (confocal and dark-field microscopes) and evaluated for their functionality (viability and proliferation) by Trypan-blue exclusion assay (*Beckman Coulter VI-Cell*). All measurements were performed at room temperature (25°C).

Atomic force microscope

In order to probe cytoskeleton organization, HPMECs stiffness was measured with AFM (*Veeco BioscopeII*) combined with an optical microscope (*Nikon TE-2000*) at room temperature in liquid environment. The seeding medium was washed twice with PBS and then replaced with new cell culture medium, where AFM was performed (within 1h from incubator removal).

A triangular, tipless, silicon-nitride AFM cantilever (*Veeco*) was used, with a nominal spring constant of 0.32 N/m, which was calibrated each time before measuring by thermal-noise method, after photodetector-sensitivity calibration over a glass slide within cell medium. The AFM tip was a colloidal probe, a 5µm-diameter silica particle, attached at the apex of the V-shaped cantilever (*Novascan*), which was cleaned each time before the experiment leaving it in ethanol overnight.

The AFM probe was engaged in contact mode, and then continuously-ramped (force mode) over the cell in order to obtain significant force–displacement curves. The following parameters were used during measurement: maximum applied-force of 1 nN (relative trigger mode), ramp-size of 300 nm, ramping velocity of 250 nm/s (for both the approach and retraction portions of the force curve). For each experimental condition (particle size and

concentration), 4÷6 cells were measured, acquiring approximately 30 force-curves/cell. The AFM was controlled and the force data were m by the AFM software (*Veeco NanoScope v7.30*).

The force curves obtained as described above were then analyzed through the Hertz model as already presented in Section 3.4.2.

Cells fluorescent staining

In order to investigate cytoskeleton structure, HPMECs were fluorescently stained for microscope observation with commercial dyes: their actin with phalloidin conjugated with AlexaFluor 488 (*Invitrogen*) and their nuclei with TO-PRO-3 (*Invitrogen*). The following staining protocol was used.

Cells were washed (with PBS, 5 minutes twice), fixed in 3.7% methanol-free paraformaldehyde (*EMS*) for 15 minutes at room temperature, washed, permeabilized in 0.1% Triton X-100 (*MP Bio*, diluted in PBS) for 5 minutes, washed, incubate with Image-iT FX Signal Enhancer (*Invitrogen*) for 30 minutes at room temperature in a humid environment, washed, incubated with the staining fluorescent phalloxin solution (7% methanolic stock-solution diluted in PBS + 1% BSA to reduce nonspecific staining) for 30 minutes at room temperature, washed, incubated with 2 μ M TO-PRO-3 solution (diluted in PBS) for 30 minutes at room temperature, washed, mounted with ProLong Gold (without DAPI, *Invitrogen*) and carefully-sealed with Cytoseal 280 (*EMS*) to ensure long-term stability.

Confocal scanning protocol

Cells stained as described above were scanned with an upright confocal microscope (*Leica DM6000B*), using a 63x objective with oil-immersion ($n > 1.5$). The same acquisition settings were used for all the confocal micrographs. Z-stacks were acquired with a fixed number of planes (13) at 100 Hz velocity, with pinhole at 1 PAU (95.5 μ m). For actin fluorescence and bright-field, excitation laser was at 488 nm; for nuclei fluorescence, at 633 nm.

Statistical analysis

In order to compare two or more groups, one-way ANOVA was used, assuming that the difference between their means was statistically-significant for $P < 0.05$.

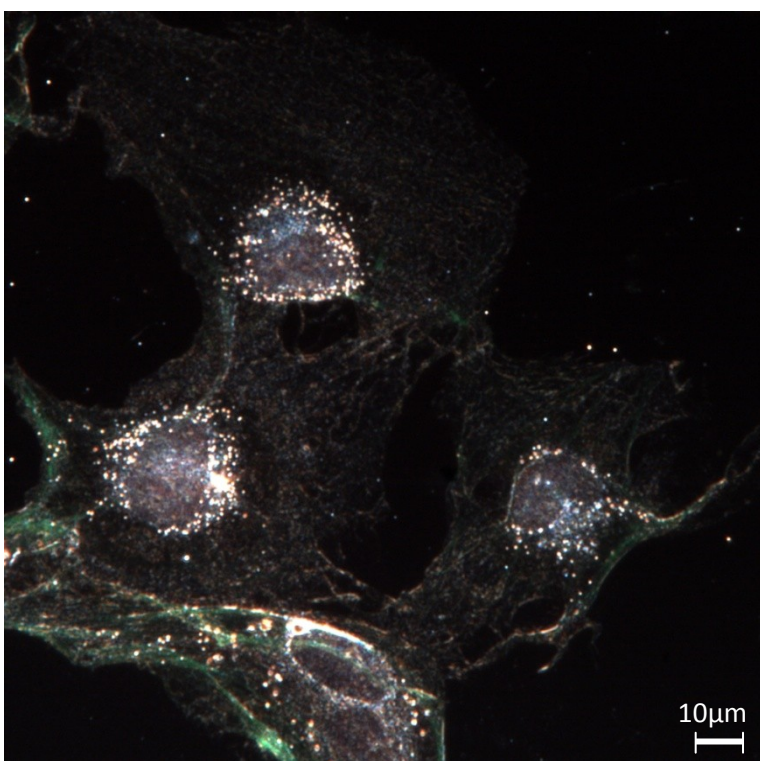
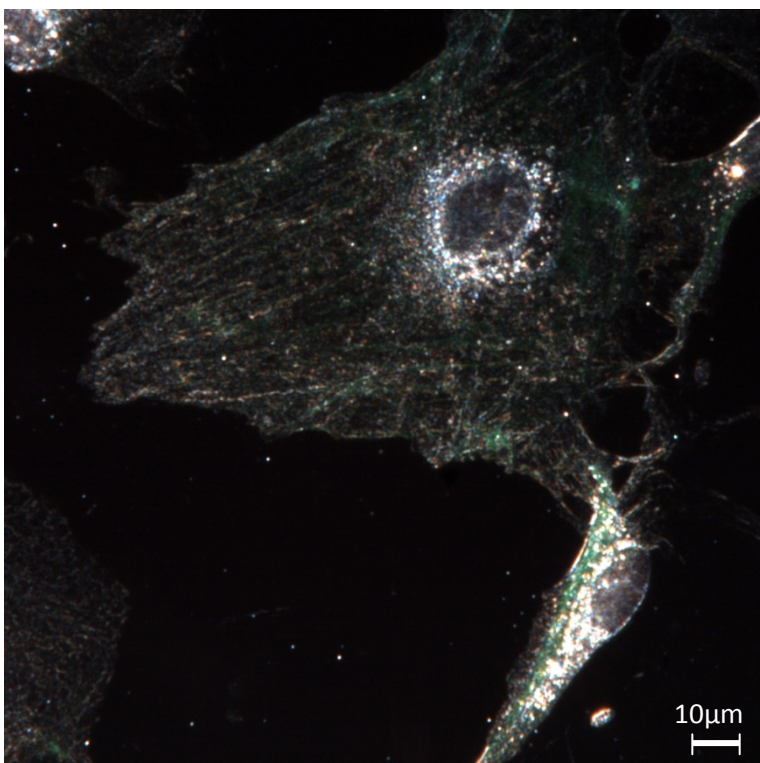
3.5.3 Main results and discussion

As explained in the Materials & Methods section, live cells were incubated with positively-charged gold nanoparticles (in order to enhance particle endocytosis from cells) for 24h, and were subsequently studied with several techniques, mostly microscopies (both near- and far-field).

Perinuclear distribution of gold nanoparticles

The first result was the confirmation of the peri-nuclear accumulation of the gold nanoparticles inside the cells. As expected [Uboldi *et al* 2009, Chen *et al* 2008], both 30 (**Figure 3.5.2A**) and 100 (**Figure 3.5.2B**) nm particles showed to accumulate in the perinuclear region of the HPMECs, as qualitatively demonstrated by dark-field microscopy and confocal fluorescent microscopy respectively. So, at least in this case, the intra-cellular distribution of the particles does not seem to depend on their size.

A) 30nm



Tommaso Novellino

B) 100nm

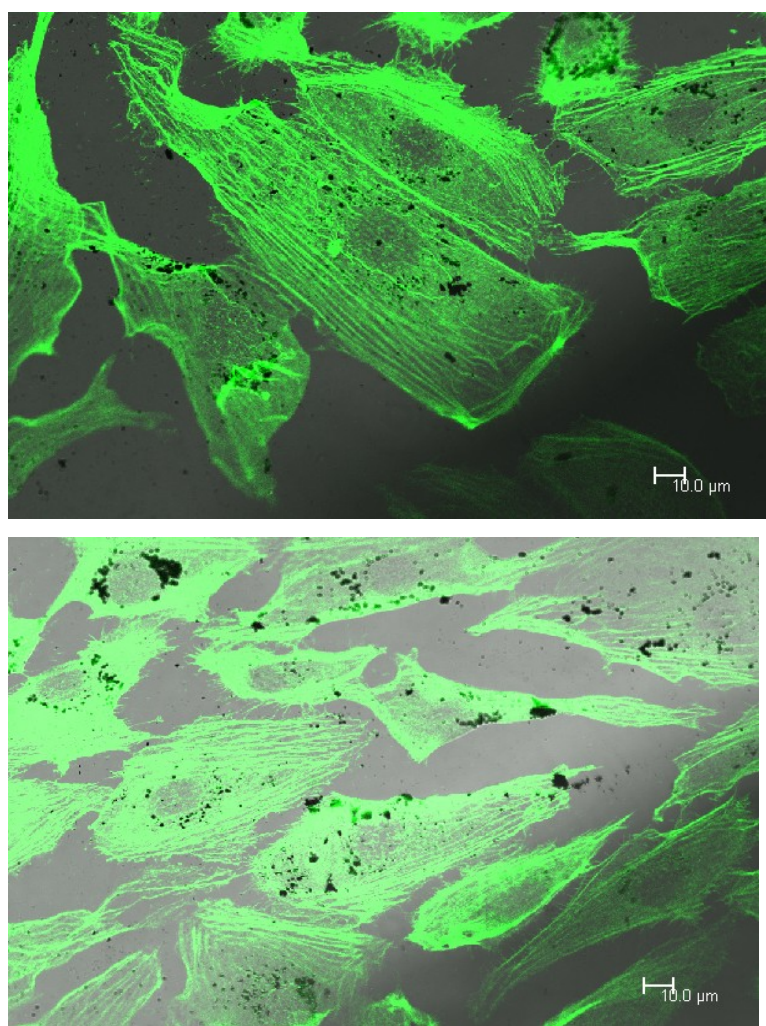


Figure 3.5.2 Gold nanoparticles distribution inside HPMECs as imaged by microscopy.

(A) 30nm particles, imaged with dark-field microscopy (concentration 0.5 mg/ml)

(B) 100nm particles, imaged by confocal microscopy: merge between fluorescence showing actin (green) and bright-field showing particles (concentration 0.1 mg/ml)

Figure 3.5.2A shows cell dark-field micrographs after 24h incubation with 30nm spherical particles, incubated at concentration 0.5 mg/ml. The two images (100x), representing two different portions of the same sample, show the scattering of the particles and particularly their presence inside the cells. The intra-cellular distribution is clearly perinuclear.

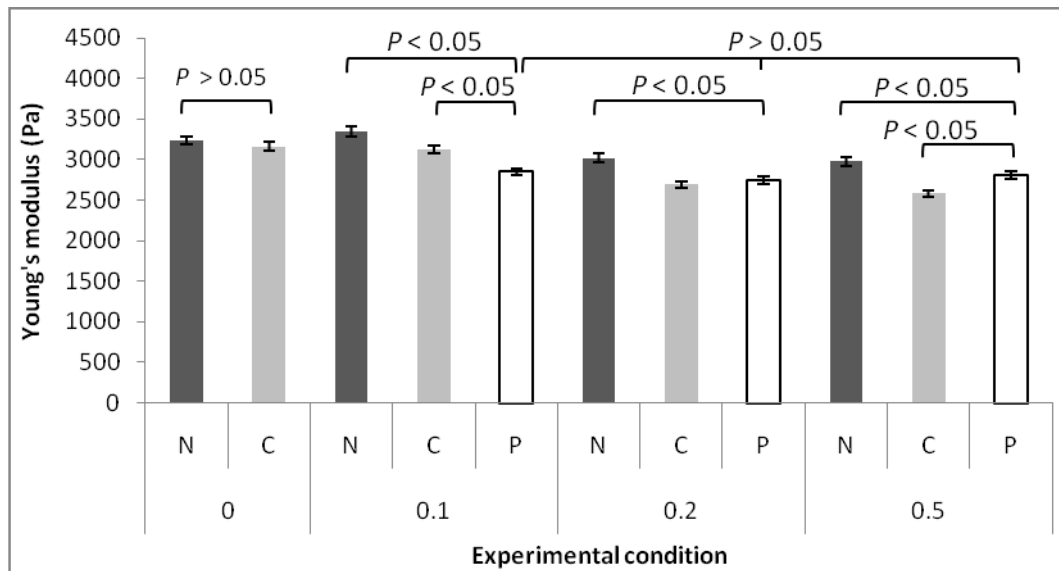
Figure 3.5.2B shows cell confocal micrographs after 24h incubation with 100nm spherical particles, incubated at concentration 0.1 mg/ml. The two images show the presence of the particles, which again tend to accumulate perinuclearly inside the cells.

Cell softening associated with gold nanoparticles

The second result (**Figure 3.5.3**) was related to the Young's moduli of the cells, whose cell membrane stiffness was measured by AFM in force mode. Since the membrane is mainly supported by the cytoskeletal network, its stiffness likely estimates that of the underlining cytoskeleton.



A) 30 nm



B) 100 nm

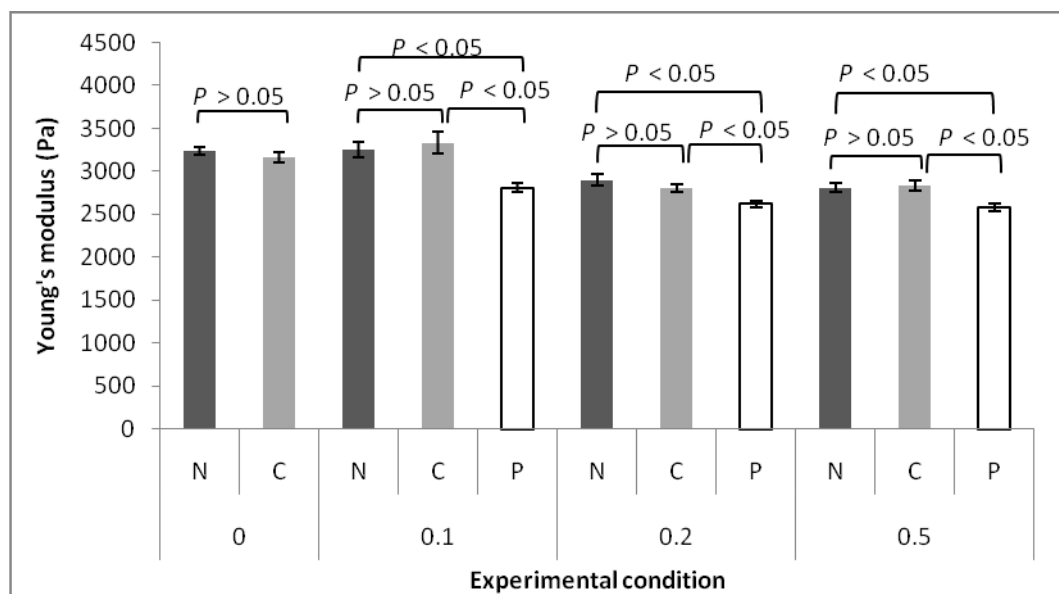


Figure 3.5.2 Gold nanoparticles distribution inside HPMECs as imaged by microscopy.

(A) 30nm particles, imaged with dark-field microscopy (concentration 0.5 mg/ml)

(B) 100nm particles, imaged by confocal microscopy: merge between fluorescence showing actin (green) and bright-field showing particles (concentration 0.1 mg/ml).

Tommaso Novellino

Figures 3.5.3A and B show cell stiffness results after 24h incubation with 30 and 100 nm spherical particles respectively, for different incubation concentrations and cell locations. The same results are reported in tabular form as follows:



A) 30 nm

Concentration (mg/ml)	Cell location	Young's modulus (Pa)	SEM (Pa)	n =
0	N	3234.1	47.6	108
0	C	3162.7	56.0	119
0.1	N	3347.8	57.9	115
0.1	C	3118.6	47.4	112
0.1	P	2848.7	46.7	114
0.2	N	3019.3	53.3	87
0.2	C	2695.3	39.9	101
0.2	P	2740.5	45.9	96
0.5	N	2980.6	53.1	78
0.5	C	2582.9	40.7	98
0.5	P	2811.2	42.3	111

B) 100 nm

Concentration (mg/ml)	Cell location	Young's modulus (Pa)	SEM (Pa)	n =
0	N	3234.1	47.6	108
0	C	3162.7	56.0	119
0.1	N	3250.6	91.5	155
0.1	C	3327.8	127.7	167
0.1	P	2806.8	52.6	122
0.2	N	2900.0	73.6	154
0.2	C	2804.2	50.6	126
0.2	P	2620.5	34.1	114
0.5	N	2809.3	51.9	156
0.5	C	2831.4	59.1	157
0.5	P	2579.9	38.9	96

Table 3.5.1 Data plotted in **Figure 3.5.3**.

In **Figure 3.5.3**, it can be noted that the measured Young's modulus depends, within the same probed-cell and particle-concentration, on the cell-location. This fact is expected, as per the cell well-known heterogeneity [Shroff *et al* 1995].

More interestingly, a consistent decrease of stiffness of location P compared to both locations N and C is shown for each non-control concentration (0.1÷0.5 mg/ml). This local softening is even more evident in the 100nm incubation: in this case, for each concentration there is no statistically-significant difference between the nucleus and the cytoplasm, while there is always a statistically-significant difference between both the nucleus & the perinuclear region and the cytoplasm & the perinuclear region. The perinuclear softening correlates with the literature, where the Cytochalasin B (a myco-toxin which blocks the formation of contractile microfilaments, or actin filaments) is reported to substantially diminish the force required for indentation in perinuclear regions of the cell but has no apparent effect on the nucleus [Elson 1988]; Cytochalasin B provides a depolymerization effect, since it shortens the actin filaments (by blocking monomer addition at the fast-growing end of polymers) [Theodoropoulos *et al* 1994]. Hence, taking together our data with the previous literatures, a local actin depolymerization is seemingly caused by the internalized gold nanoparticles.

Furthermore, for both particle sizes, for increasing non-control concentrations (0.1 → 0.5 mg/ml), the Young's modulus decreases for each location. This stiffness reduction may be interpreted as a progressive cytoplasm degradation, where its disruption is increased by the particles intra-cellular presence.

Gold nanoparticles are associated with cytoskeletal disorganization

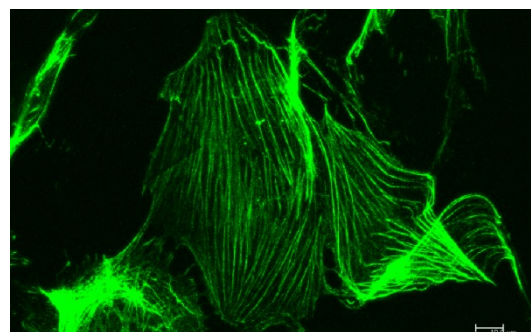
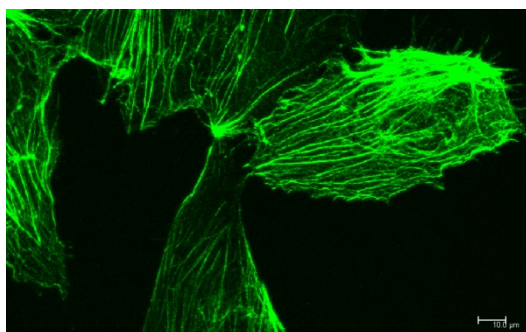
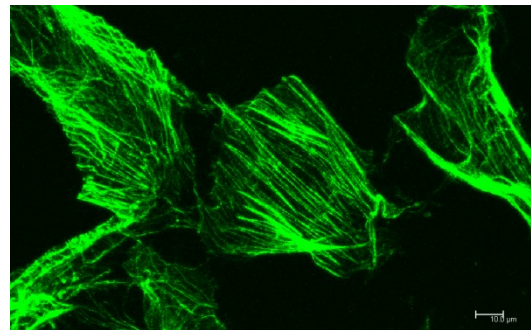
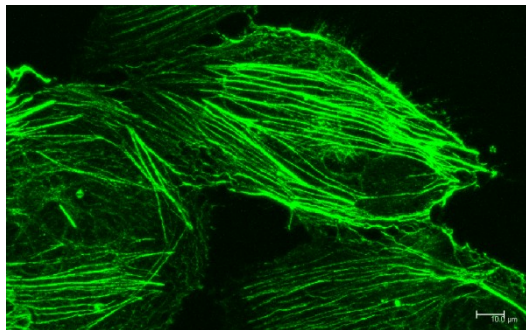
By staining actin filaments, using confocal microscope is possible to obtain meaningful and beautiful representations of cells internal mechanical status.

Particularly, **Figure 3.5.4** shows qualitatively –for a given cell plane (the median one)– the variation of the internal cytoskeletal organization of the cells incubated with different particles concentration; more specifically, a larger actin disorganization can be observed with increasing concentrations.

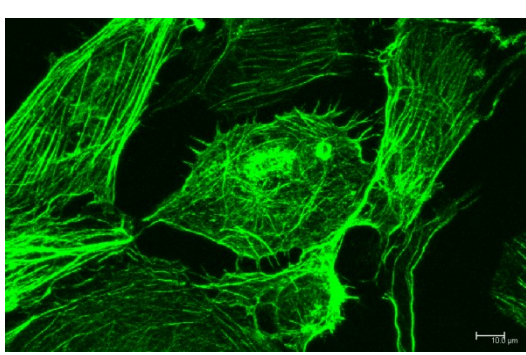
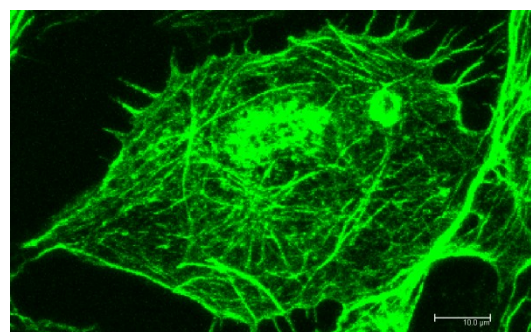
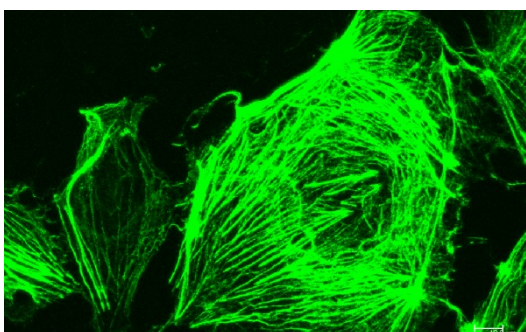


A) 30nm

Concentration 0 mg/ml

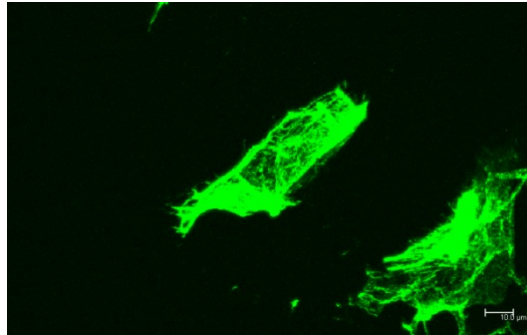


Concentration 0.1 mg/ml

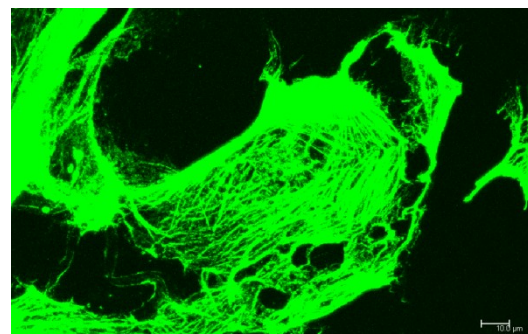
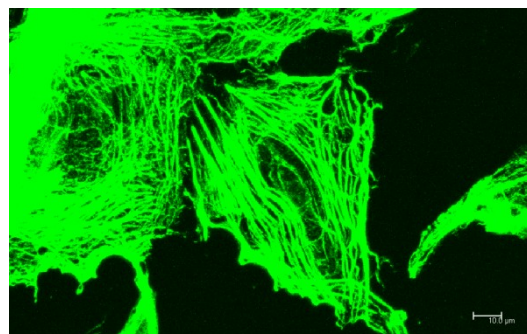


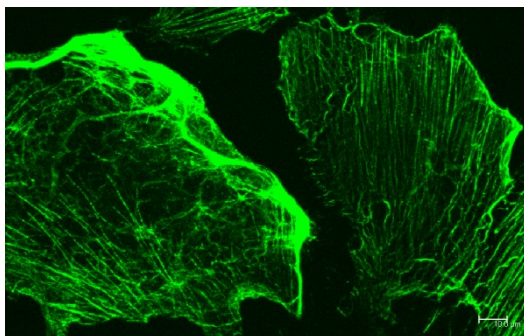
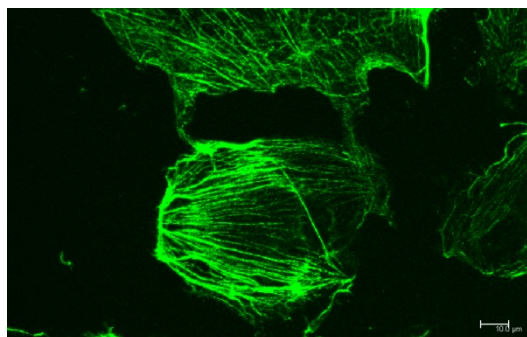
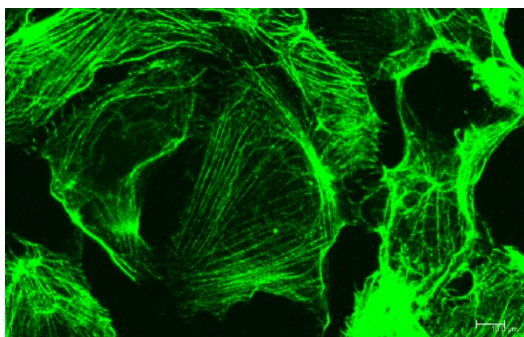
Tommaso Novellino

Concentration 0.2 mg/ml



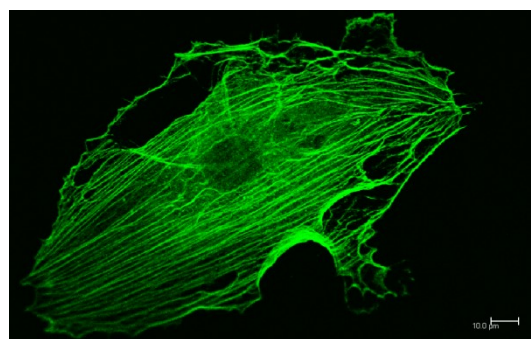
Concentration 0.5 mg/ml



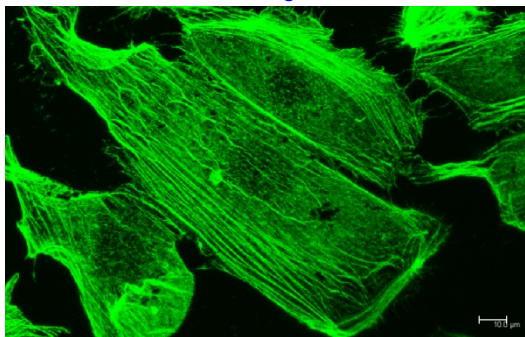


B) 100nm

Concentration 0 mg/ml



Concentration 0.1 mg/ml



Concentration 0.5 mg/ml

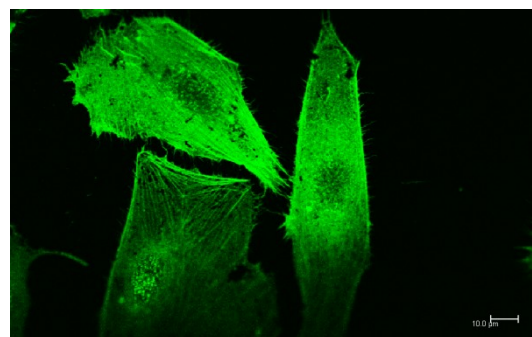
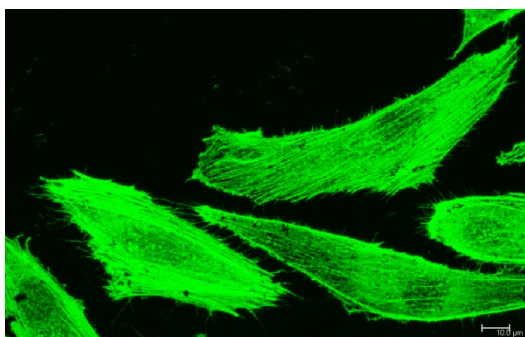


Figure 3.5.4 Cytoskeleton disorganization as imaged by confocal microscope, for both 30 (A) and 100 (B) nm particles.

Shown micrographs are frames –extracted from the acquired Z-stacks– corresponding to the cell median planes.

Figures 3.5.4A and B show cell confocal micrographs after 24h incubation with 30 and 100 nm spherical particles respectively, for different concentrations. These results show qualitatively that, as particles incubation concentration increases, the cytoskeleton appears more disorganized and fluorescently bright at the same time. Thus, a differential organization of the actin cytoskeleton for the same plane of the same is obtained by changing quantity of the particles internalized by the cell.

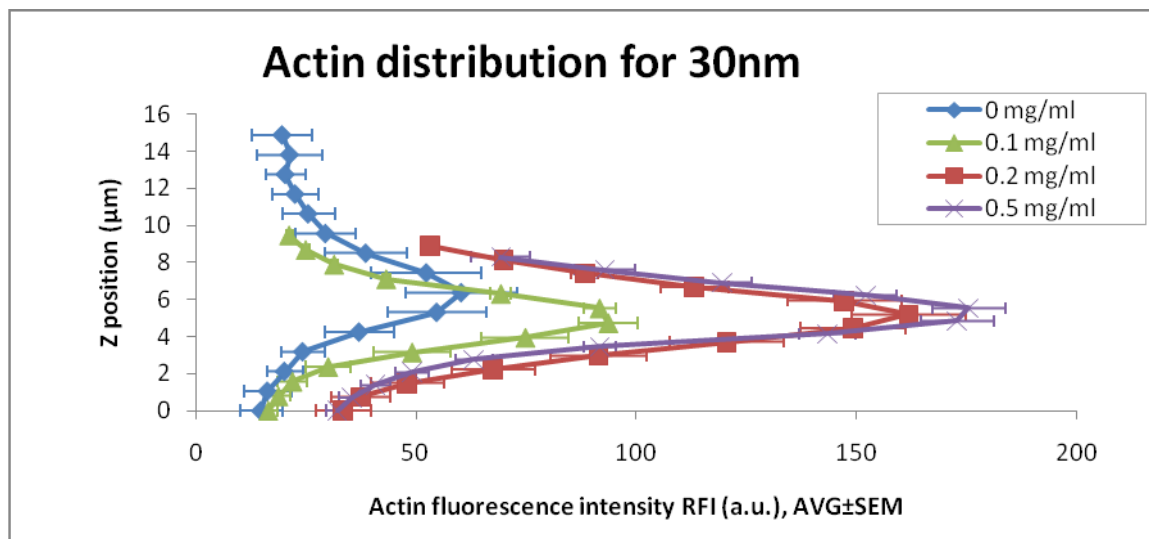
Actin distribution

In order to quantitatively evaluate and to better interpret **Figure 3.5.4**, the fluorescence intensity (Relative Fluorescence Intensity, RFI) of the actin on different planes has been calculated, for the different concentrations of both particle sizes.

The fluorescence calculation, done by the confocal microscope's software *Leica Application Suite – Advanced Fluorescence*, consisted in averaging –for a given plane (frame of the Z-stack)– the actin fluorescence in the region of interest (ROI) chosen as the cell border.

The results are shown in **Figure 3.5.5.**

A) 30nm



B) 100nm

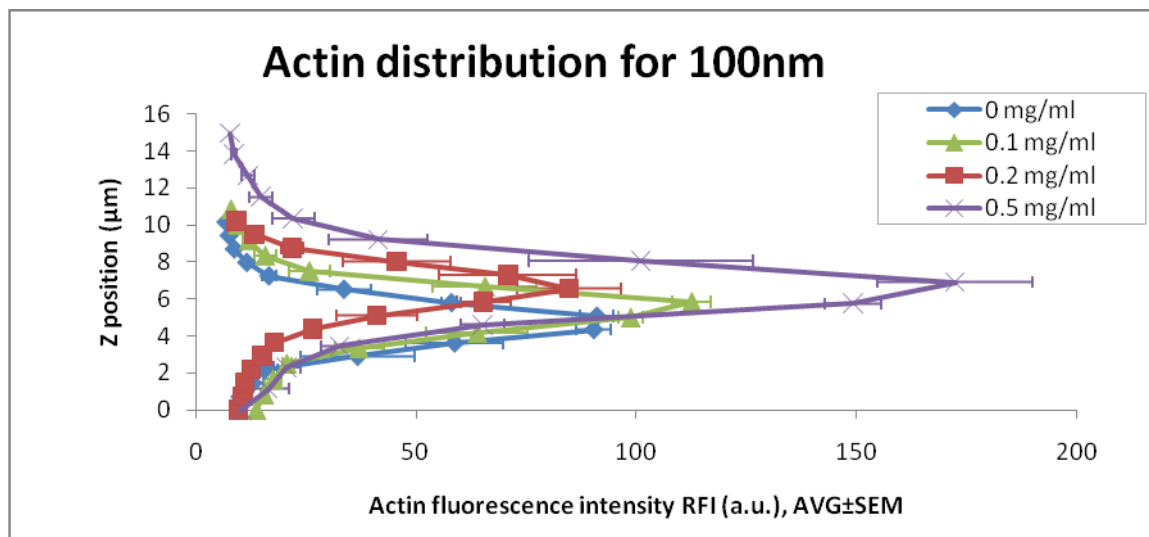


Figure 3.5.5 Actin fluorescence distribution in cell confocal micrographs after 24h incubation with 30nm (A) and 100nm (B) spherical particles respectively, for different concentrations.

Distributions are plotted inside the cell from its basal ($Z = 0$) to its apical planes. Results are presented as mean \pm SEM.

As can be seen from **Figure 3.5.5**, intra-cellular actin fluorescence intensities increase with particles concentration pretty monotonically, the only exception being represented by

Tommaso Novellino

0.2 mg/ml concentration for the 100nm particles. These results, given together the images presented in **Figure 3.5.4**, show an overall increase of actin quantity inside the cell as the incubated, and hence internalized (as also confirmed by optical bright-field microscopy), particle concentration increases.

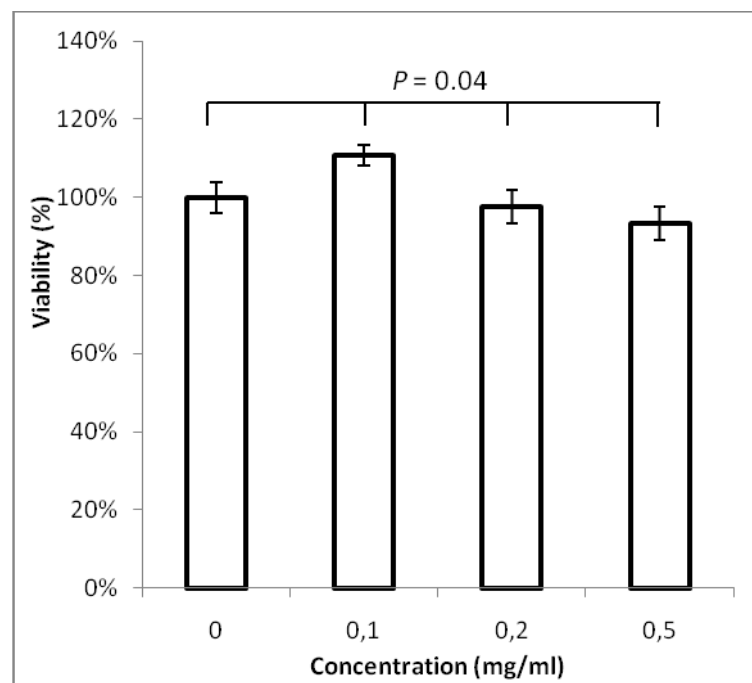
Cell overall functionality is essentially unchanged

While the cytoskeletal/mechanical functionality of the HPMECs appears altered by the presence of the internalized gold nanoparticles (**Figures 3.5.3÷5**), the overall functionality of the cells does not seem to change significantly as from **Figure 3.5.6**.



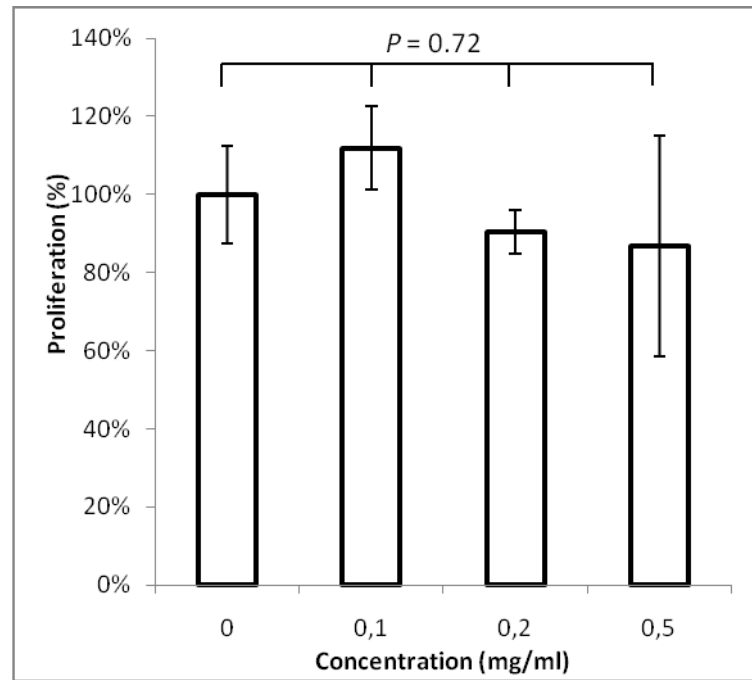
A) 30nm

Cell viability



Compared groups	P-value
0 vs 0.1	0.06
0 vs 0.2	0.70
0 vs 0.5	0.29
All	0.04

Cell proliferation

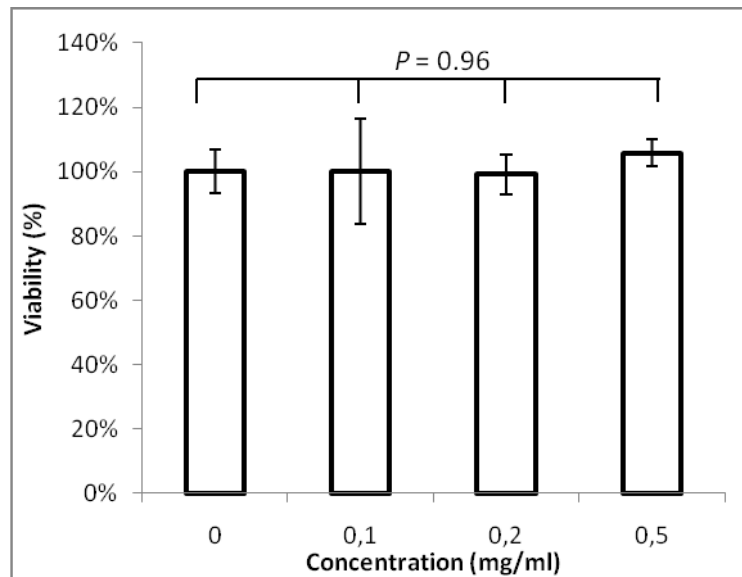


Compared groups	P-value
0 vs 0.1	0.50
0 vs 0.2	0.50
0 vs 0.5	0.68
All	0.72

Tommaso Novellino 160

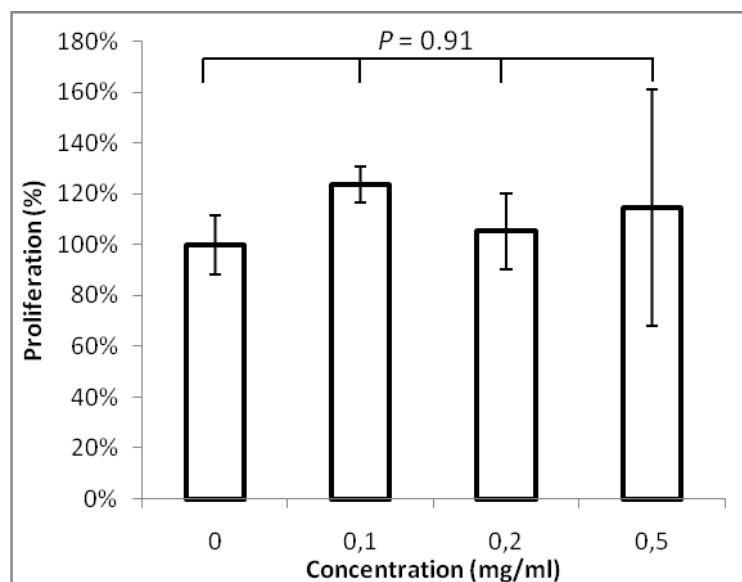
B) 100nm

Cell viability



Compared groups	P-value
0 vs 0.1	0.99
0 vs 0.2	0.93
0 vs 0.5	0.50
All	0.96

Cell proliferation



Compared groups	P-value
0 vs 0.1	0.16
0 vs 0.2	0.79
0 vs 0.5	0.78
All	0.91

Figure 3.5.6 Cells viability and proliferation, as both measured by Trypan-blue exclusion assay, for all particle sizes –(A) 30nm and (B) 100nm– and concentrations.

Both quantities are normalized relatively to controls (concentration 0 mg/ml). Results are plotted as mean±SEM.

The vital status of a cell (*viability*) and its propensity to grow and proliferate (*proliferation*) can be seen as indicators of its overall functionality. For this reason, they have been both measured –by an automatized reading (*Beckman Coulter VI-Cell*) of the Trypan-blue exclusion assay (where dead/unviable cells, having become permeable, are blue-colored because of the intracellular entrance of the Trypan inside their membrane)– in order to assess a possible change in their values due to the presence of the gold nanoparticles at different concentrations.

Viability is simply defined as:

$$Viability = \frac{\text{number of viable cells}}{\text{total number of cells (viable or dead)}} [\%] \quad (\text{Equation 3.5.1})$$

Proliferation, instead, simply refers to the current number of viable cells measured over time, in order to give a trend of their growth (if the cell population is increasing or decreasing in number).

The VI-Cell instrument automatically processes and measures the number of both the viable cells and all the cells, from which the two above quantities are derived.

Figure 3.5.6A shows cell functionality results after 24h incubation with 30nm spherical particles, including viability and proliferation normalized relatively to controls, for different concentrations. Results plotted as mean±SEM ($N = 4$). No significant difference is observed between controls and non-controls as per proliferation.

Figure 3.5.6B shows cell functionality results after 24h incubation with 100nm spherical particles, including viability and proliferation normalized relatively to controls, for

Tesi di dottorato in Ingegneria Biomedica, di Tommaso Novellino,
discussa presso l'Università Campus Bio-Medico di Roma in data 10/03/2011.
La disseminazione e la riproduzione di questo documento sono consentite per scopi di didattica e ricerca,
a condizione che ne venga citata la fonte.

different concentrations. Results plotted as mean \pm SEM ($N = 3$). No significant difference is observed between controls and non-controls as per both viability and proliferation.



163

3.5.4 Conclusions

With increasing particles concentration, actin quantity increases (**Figure 3.5.4** and **3.5.5**) but at the same time both cell Young's modulus (**Figure 3.5.3**) and actin cytoskeletal organization (**Figure 3.5.5**) decrease: it is then tempted to speculate that the overall cytoskeleton functionality decreases, as it was also indirectly confirmed by a visible decrease of cells adhesion to culturing Petri-dish with increasing particles concentration.

Hence, gold nanoparticles internalized by human endothelial cells (HPMECs) seem to produce in them a progressive cytoskeleton disruption, while no apparent global functional cytotoxicity –in terms of decreasing either viability or proliferation– is shown (**Figure 3.5.6**). For this reason, when intravascularly-injecting them, in order to avoid some systemic endothelial cytoskeletal alteration, could be recommendable to conjugate them with moieties which specifically bind them to the target of interest, avoiding a potential unwanted bio-modification.



3.5.5 Acknowledgements of Section 3.5

I thankfully acknowledge the following people contributions:

- General-idea conceiving, supervision: Paolo Decuzzi
- Experimental design and planning: Tommaso Novellino, Paolo Decuzzi
- AFM measurements: Tommaso Novellino, Ana Maria Zaske
- Cellular staining: Ana Maria Zaske
- Confocal measurements: Tommaso Novellino
- Cell culture and functionality-measurements: Eva Golunski, Ana Maria Zaske
- Dark-field measurements: Srimeenakshi (Meenu) Srinivasan
- Data analysis and statistics: Tommaso Novellino
- Results discussion and interpretation: Tommaso Novellino, Paolo Decuzzi.

4 Conclusions

The present work is constituted of several nanomedical studies, which can be regrouped in a nanoparticle and in a nanochanneled-device areas; the first had more a biophysical aim, the second was oriented towards drug-delivery.

In the nanoparticle area, *in-vitro* effect of two biochemical/physical agents –TNF- α and gold nanoparticles– on live human endothelial cells, of several cell-lines, was assessed; AFM probed the mechanical properties (stiffness, adhesion) of the cells, while confocal microscopy revealed their cytoskeletal organization. For the TNF- α study, cells inflamed by that pro-inflammatory cytokine shown a change in their mechanics (increase in stiffness for all three cell-lines evaluated, decrease in non-specific adhesion and visco-elasticity except for cell-line HPMECs), in their cytoskeleton structure (increase in actin filaments, both density and thickness) and in their receptor expression (over-expression of ICAM-1 compared to controls, as expected): overall, the *in-vitro* response to TNF- α -stimulation was demonstrated to not depend on the vascular district. For the gold-nanoparticles study, cells which had internalized them –mainly in their perinuclear region– shown a local change in their mechanics (differential stiffness between within-cell locations and between within-location concentrations) and in their cytoskeleton structure (increase in actin filaments but decrease in actin organization, for the same cell-plane), while no substantial variation in overall cell-functionality (viability and proliferation) was observed: overall, the *in-vitro* response to gold-nanoparticles-stimulation was demonstrated to significantly though locally affect the mechanical and cytoskeletal properties of the studied cell-line (HPMECs), suggesting that targeted-version of gold nanoparticles be used when intravascularly injected.

In the nanochanneled-device area, *in-vivo* and *in-lab* release of two biomolecules –IFN- α and a dextran– through academically-microfabricated delivery devices was monitored; the concentration of those solutes was measured over months, in order to assess the long-term aspect of the devices release properties, which were already demonstrated to be linear under certain conditions. For the IFN- α study, delivery devices loaded with that drug (human IFN- α -2b, tradename *Intron-A*) were inserted inside both bio-compatible company-fabricated

capsules implanted in healthy rats for *in-vivo* and custom testing-devices for *in-lab* release evaluation, IFN concentration was measured by ELISA, histological analysis was also performed: *in-vivo* results showed a potential constant-release within one rat for 10 days, *in-lab* results showed an average constant-release (14 ng/d, $n = 9$) for 70 days. For the dextran study, delivery devices loaded with that probe (MW = 10kDa, fluorescently-labeled) were inserted inside custom testing-devices for *in-lab* release evaluation, dextran concentration was measured by spectrofluorimeter: *in-lab* results showed an average constant-release ($n = 16$) for 60 days.

In conclusion, nanomedicine –a very rapidly-growing research field– potentially provides unprecedented engineerable tools to deal with many biomedical applications and mechanisms, as in the cases here presented of *in-vitro* inflammation, *in-vitro* nanoparticles-internalization and *in-vivo* drug-delivery.

5 References

Adiga SP, Jin C, Curtiss LA, Monteiro-Riviere NA, Narayan RJ. Nanoporous membranes for medical and biological applications. *Wiley interdisciplinary reviews–nanomedicine and nanobiotechnology* 2009, 1(5): 568–81.

Aimé JP, Elkaakour Z, Odin C, Bouhacina T, Michel D, Curbly J, Dautant A. Comments on the use of the force mode in atomic force microscopy for polymer films. *Journal of Applied Physics* 1994, 76(2): 754–762.

Akamine S, Barrett RC, Quate CF. Improved atomic force microscope images using microcantilevers with sharp tips. *Applied Physics Letters* 1990, 57: 316–318.

Alcaraz J, Buscemi L, Grabulosa M, Trepat X, Fabry B, Farrè R, Navajas D. Microrheology of Human Lung Epithelial Cells Measured by Atomic Force Microscopy. *Biophysical Journal* 2003, 84: 2071–2079.

Alessandrini A, Facci P. AFM: a versatile tool in biophysics. *Measurement Science and Technology* 2005, 16: R65–R92.

Alexander S, Hellemans L, Marti O, Schneir J, Elings V, Hansma PK, Longmire M, Gurley J. An atomic-resolution atomic-force microscope implemented using an optical lever. *Journal of Applied Physics* 1989, 65: 164–167.

Alsteens D, Dupres V, McEvoy K, Wildling L, Gruber HJ, Dufrene YF. Structure, cell wall elasticity and polysaccharide properties of living yeast cells, as probed by AFM. *Nanotechnology* 2008, 19: 384005 (9pp).

Amato F, Cosentino C, Prich S, Ferrone M, Fermaglia M, Cheng MM, Walczak R,


Tommaso Novellino
168

Ferrari M. Multiscale Modeling of Protein Transport in Silicon Membrane Nanochannels. Part 2. From Molecular Parameters to a Predictive Continuum Diffusion Model. *Biomedical Microdevices* 2006, 8: 291–298.

Amer NM, Meyer G. A simple method for a remote sensing of stylus deflection in AFM. *Bulletin of the American Physical Society* 1988, 33: 319.

Amin RM, Mohamed MB, Ramadan MA, Verwanger T, Krammer B. Rapid and sensitive microplate assay for screening the effect of silver and gold nanoparticles on bacteria. *Nanomedicine* 2009, 4: 637–43.

Attard P. Measurement and interpretation of elastic and viscoelastic properties with the atomic force microscope. *Journal of Physics: Condensed Matter* 2007, 19: 473201.

Badkar AV, Smith AM, Eppstein JA, Banga AK. Transdermal Delivery of Interferon Alpha-2B using Microporation and Iontophoresis in Hairless Rats. *Pharmaceutical Research* 2007, 24(7): 1389–1395.

Bajaj A, Miranda OR, Kim IB, Phillips RL, Jerry DJ, Bunz UHF, Rotello VM. Detection and differentiation of normal, cancerous, and metastatic cells using nanoparticle-polymer sensor arrays. *Proceedings of the National Academy of Sciences USA* 2009, 106: 10912–6.

Bausch AR, Möller W, Sackmann E. Measurement of local viscoelasticity and forces in living cells by magnetic tweezers. *Biophysical Journal* 1999, 76: 573–9.

Beebe DJ, Mensing GA, Walker GM. Physics and applications of microfluidics in biology. *Annual Review of Biomedical Engineering* 2002, 4: 261–286.

Bell GI, Dembo M, Bongrand P. Competition Between Nonspecific Repulsion and Specific Bonding. *Biophysical Journal* 1984, 45: 1051–1064.

Tesi di dottorato in Ingegneria Biomedica, di Tommaso Novellino,
discussa presso l'Università Campus Bio-Medico di Roma in data 10/03/2011.
La disseminazione e la riproduzione di questo documento sono consentite per scopi di didattica e ricerca,
a condizione che ne venga citata la fonte.

Benoit M, Gabriel D, Gerisch G, Gaub HE. Discrete interactions in cell adhesion measured by single-molecule force spectroscopy. *Nature Cell Biology* 2000, 2: 313–317.

Benoit M, Gaub HE. Measuring Cell Adhesion Forces with the Atomic Force Microscope at the Molecular Level. *Cells Tissues Organs* 2002, 172: 174–189.

Berdyyeva TK, Woodworth CD, Sokolov I. Human epithelial cells increase their rigidity with ageing in vitro: direct measurements. *Physics in Medicine and Biology* 2005, 50: 81–92.

Bhushan B, Kulkarni AV, Koinkar VN, Boehm M, Odoni L, Martelet C, Belin M. Microtribological Characterization of Self-Assembled and Langmuir-Blodgett Monolayers by Atomic and Friction Force Microscopy. *Langmuir* 1995, 11: 3189–3198.

Biggs S. Steric and Bridging Forces between Surfaces Bearing Adsorbed Polymer: An Atomic Force Microscopy Study. *Langmuir* 1995, 11(1): 156–162.

Binnig G, Rohrer H, Gerber CH, Weibel E. Surface Studies by Scanning Tunneling Microscopy. *Physical Review Letters* 1982, 49(1): 57–61.

Binnig G, Quate CF, Gerber C. Atomic force microscopy. *Physical Review Letters* 1986, 56(9): 930–933.

Binnig G, Smith DPE. Single- tube three- dimensional scanner for scanning tunneling microscopy. *Review of Scientific Instruments* 1986, 57: 1688–1689.

Binnig G, Rohrer H. Scanning tunneling microscopy – from birth to adolescence. *Reviews of Modern Physics* 1987, 59: 615–625.

Boisselier E, Astruc D. Gold nanoparticles in nanomedicine: preparations, imaging, diagnostics, therapies and toxicity. *Chemical Society Reviews* 2009, 38: 1759–82.

Bongrand P. Ligand-Receptor Interactions. *Reports on Progress in Physics* 1999, 62: 921–968.


Tommaso Novellino
170

Bowen WR, Hilal N, Lovitt RW, Wright CJ. Direct measurement of the force of adhesion of a single biological cell using an atomic force microscope. *Colloids and Surfaces A: Physicochemical and Engineering Aspects* 1998, 136: 231–234.

Bowen WR, Doneva TA. Atomic Force Microscopy Studies of Membranes: Effect of Surface Roughness on Double-Layer Interactions and Particle Adhesion. *Journal of Colloid and Interface Science* 2000, 229: 544–549.

Bowen WR, Doneva TA, Austin J, Stoton G. The use of atomic force microscopy to quantify membrane surface electrical properties. *Colloids and Surfaces A: Physicochemical and Engineering Aspects* 2002, 201: 73–83.

Boyer D, Tamarat P, Maali A, Lounis B, Orrit M. Photo-thermal imaging of nanometer-sized metal particles among scatterers. *Science* 2002, 297: 1160–3.

Bozkurt B, Mann DL, Deswal A. Biomarkers of inflammation in heart failure. *Heart Failure Reviews* 2009, 15(4): 331–341.

Burnham NA, Colton RJ, Pollock HM. Interpretation issues in force microscopy. *Journal of Vacuum Science & Technology A* 1991, 9(4): 2548–2556.

Butt HJ, Wolff EK, Gould SAC, Northern BD, Peterson CM, Hansma PK. Imaging cells with the atomic force microscope. *Journal of Structural Biology* 1990, 105: 54–61.

Butt HJ, Jaschke M. Calculation of thermal noise in atomic force microscopy. *Nanotechnology* 1995, 6: 1–7.

Butt HJ, Cappella B, Kappl M. Force measurements with the atomic force microscope: Technique, interpretation and applications. *Surface Science Reports* 2005, 59: 1–152.

Buzea C, Blandino IIP, Robbie K. Nanomaterials and nanoparticles: sources and toxicity. *Biointerphases* 2007, 2(4): MR17–MR172.

Campos SB, Ashworth SL, Wean S, Hosford M, Sandoval RM, Hallett MA, Atkinson SJ, Molitoris BA. Cytokine-induced F-actin reorganization in endothelial cells involves RhoA activation. *American Journal of Physiology–Renal Physiology* 2009, 296(3): F487–95.

Canetta E, Duperray A, Leyrat A, Verdier C. Measuring cell viscoelastic properties using a force spectrometer: influence of protein-cytoplasm interactions. *Biorheology* 2005, 42(5): 321–333.

Cappella B, Dietler G. Force-distance curves by atomic force microscopy. *Surface Science Reports* 1999, 34: 1–104.

Carl P, Schillers H. Elasticity measurement of living cells with an atomic force microscope: data acquisition and processing. *European Journal of Physiology* 2008, 457: 551–559.

Chen PC, Mwakwari SC, Oyelere AK. Gold nanoparticles: From nanomedicine to nanosensing. *Nanotechnology, Science and Applications* 2008, 1: 45–66.

Chin CD, Linder V, Sia SK. Lab-on-a-chip devices for global health: Past studies and future opportunities. *Lab Chip* 2007, 7: 41–57.

Chithrani BD, Ghazani AA, Chan WCW. Determining the Size and Shape Dependence of Gold Nanoparticle Uptake into Mammalian Cells. *Nano Letters* 2006, 6(4): 662–668.

Chouinard JA, Grenier G, Khalil A, Vermette P. Oxidized-LDL induce morphological changes and increase stiffness of endothelial cells. *Experimental Cell Research* 2008, 314: 3007–3016.

Churg A, Stevend B, Wright JL. Comparison of the uptake of fine and ultrafine TiO₂ in a tracheal explant system. *American Journal of Physiology* 1998, 274: L81–L86.

Coles JM, Blum JJ, Jay GD, Darling EM, Guilak F, Zauscher S. In Situ Friction Measurement on Murine Cartilage by Atomic Force Microscopy. *Journal of Biomechanics* 2008, 41(3): 541–548.

Conner SD, Schmid SL. Regulated portals of entry into the cell. *Nature* 2003, 422: 37–44.

Connor EE, Mwamuka J, Gole A, Murphy CJ, Wyatt MD. Gold nanoparticles are taken up by human cells but do not cause acute cytotoxicity. *Small* 2005, 1: 325–7.

Cooper GM. The cell: a molecular approach. *Sinauer* 2000, 2nd edition.

Cosentino C, Amato F, Walczak R, Boiarski A, Ferrari M. Dynamic Model of Biomolecular Diffusion through Two-Dimensional Nanochannels. *Journal of Physical Chemistry B* 2005, 109: 7358–7364.

Costa KD, Sim AJ, Yin FC. Non-Hertzian approach to analyzing mechanical properties of endothelial cells probed by atomic force microscopy. *Journal of Biomechanical Engineering* 2006, 128(2): 176–84.

Cross SE, Jin YS, Tondre J, Wong R, Rao JY, Gimzewski JK. AFM-based analysis of human metastatic cancer cells. *Nanotechnology* 2008, 19: 384003 (8pp).

Danila D, Partha R, Elrod DB, Lackey M, Casscells SW, Conyers JL. Antibody-labeled liposomes for CT imaging of atherosclerotic plaques: in vitro investigation of an anti-ICAM antibody-labeled liposome containing iohexol for molecular imaging of atherosclerotic plaques via computed tomography. *Texas Heart Institute Journal* 2009, 36(5): 393–403.

Darling EM, Zauscher S, Block JA, Guilak F. A Thin-Layer Model for Viscoelastic, Stress-Relaxation Testing of Cells Using Atomic Force Microscopy: Do Cell Properties Reflect Metastatic Potential? *Biophysical Journal* 2007, 92: 1784–1791.

Deanfield J, Donald A, Ferri C, Giannattasio C, Halcox J, Halligan S, Lerman A, Mancia G, Oliver JJ, Pessina AC, Rizzoni D, Rossi GP, Salvetti A, Schiffrin EL, Taddei S, Webb DJ. Endothelial function and dysfunction. Part I: Methodological issues for assessment in the different vascular beds: a statement by the Working Group on Endothelin and Endothelial Factors of the European Society of Hypertension. *Journal of Hypertension* 2005, 23(1): 7–17.

Decuzzi P, Lee SY, Decuzzi M, Ferrari M. Adhesion of Microfabricated Particles on Vascular Endothelium: A Parametric Analysis. *Annals of Biomedical Engineering* 2004, 32(6): 793–802.

Decuzzi P, Lee SY, Bhushan B, Ferrari M. A Theoretical Model for the Margination of Particles within Blood Vessels *Annals of Biomedical Engineering* 2005, 33(2): 179–190.

Decuzzi P, Ferrari M. The role of specific and non-specific interactions in receptor-mediated endocytosis of nanoparticles. *Biomaterials* 2007, 28: 2915–2922.

Decuzzi P, Gentile F, Granaldi A, Curcio A, Causa F, Indolfi C, Netti P, Ferrari M. Flow chamber analysis of size effects in the adhesion of spherical particles. *International Journal of Nanomedicine* 2007, 2(4): 689–696.

Decuzzi P, Pasqualini R, Arap W, Ferrari M. Intravascular Delivery of Particulate Systems: Does Geometry Really Matter? *Pharmaceutical Research* 2009, 26(1): 235–243.

De Rosa E, Novellino T, Grattoni A, Liu XW, Fine D, Hussain F, Ferrari M. In-vivo evaluation of implantable nanochanneled delivery system for long-term, sustained release. *Advanced Biomaterials* (in preparation).

Desai TA, Hansford DJ, Ferrari M. Micromachined interfaces: new approaches in cell immunoisolation and biomolecular separation. *Biomolecular Engineering* 2000, 17: 23–36.

DiNardo NJ. Nanoscale Characterization of Surfaces and Interfaces. *VCH* 2004.

Dittrich PS, Manz A. Lab-on-a-chip: microfluidics in drug discovery. *Nature Reviews Drug Discovery* 2005, 5: 210–218.

Doherty GJ, McMahon HT. Mediation, Modulation and Consequences of Membrane-Cytoskeleton Interactions. *Annual Review of Biophysics* 2008, 37: 65–95.

Doherty GJ, McMahon HT. Mechanisms of endocytosis. *Annual Review of Biochemistry* 2009, 78: 857–902.

Drummond CJ, Senden TJ. Examination of the geometry of long-range tip-sample interaction in atomic force microscopy. *Colloids and Surfaces A: Physicochemical and Engineering Aspects* 1994, 87: 217–234.

Ducker WA, Senden TJ, Pashley RM. Direct measurement of colloidal forces using an atomic force microscope. *Nature* 1991, 353: 239–241.

Dufrene YF. Atomic Force Microscopy, a Powerful Tool in Microbiology. *Journal of Bacteriology* 2002, 184(19): 5205–5213.

Dvorak HF. Discovery of vascular permeability factor (VPF). *Experimental Cell Research* 2006, 312: 522–26.

Elings VB, Gurley JA. Method of driving a piezoelectric scanner linearly with time. *United States Patent #5051646*.

El-Sayed IH, Huang XH, El-Sayed MA. Surface plasmon resonance scattering and absorption of anti-EGFR antibody conjugated gold nanoparticles in cancer diagnostics: applications in oral cancer. *Nano Letters* 2005, 5(5): 829–834.

Elson EL. Cellular mechanics as an indicator of cytoskeletal structure and function. *Annual Review of Biophysics and Biophysical Chemistry* 1988, 17: 397–430.

Erlandsson R, McClelland GM, Mate CM, Chiang S. Atomic force microscopy using optical interferometry. *Journal of Vacuum Science & Technology A* 1988, 6(2): 266–270.

Fadeel B, Garcia-Bennett AE. Better safe than sorry: Understanding the toxicological properties of inorganic nanoparticles manufactured for biomedical applications. *Advanced Drug Delivery Reviews* 2010, 62(3): 362–74.

Feldman AM, Combes A, Wagner D, Kadakomi T, Kubota T, Li YY, McTiernan C. The role of tumor necrosis factor in the pathophysiology of heart failure. *Journal of the American College of Cardiology* 2000, 35(3): 537–44.

Ferrari M. Cancer nanotechnology: Opportunities and Challenges. *Nature Reviews Cancer* 2005, 5(3): 161–71.

Friedbacher G, Fuchs H. Classification of Scanning probe microscopies (Technical Report). *Pure and Applied Chemistry* 1999, 71(7): 1337–1357.

Fu J, Schoch RB, Stevens AL, Tannenbaum SR, Han J. A patterned anisotropic nanofluidic sieving structure for continuous-flow separation of DNA and proteins. *Nature Nanotechnology* 2007, 2: 121–128.

Gaboriaud F, Dufrene YF. Atomic force microscopy of microbial cells: Application to nanomechanical properties, surface forces and molecular recognition forces. *Colloids and Surfaces B: Biointerfaces* 2007, 54: 10–19.

Gentile F, Chiappini C, Fine D, Bhavane RC, Peluccio MS, Ming-Cheng Cheng M, Liu X, Ferrari M, Decuzzi P. The effect of shape on the margination dynamics of non-neutrally buoyant particles in two-dimensional shear flows. *Journal of Biomechanics* 2008, 41: 2312–2318.

Goodman CM, McCusker CD, Yilmaz T, Rotello V. Toxicity of gold nanoparticles functionalized with cationic and anionic side chains. *Bioconjugate Chemistry* 2004, 15: 897–900.

Gotzinger M, Weigl B, Peukert W, Sommerd K. Effect of roughness on particle adhesion in aqueous solutions: A study of *Saccharomyces cerevisiae* and a silica particle. *Colloids and Surfaces B: Biointerfaces* 2007, 55: 44–50.

Tesi di dottorato in Ingegneria Biomedica, di Tommaso Novellino,
discussa presso l'Università Campus Bio-Medico di Roma in data 10/03/2011.
La disseminazione e la riproduzione di questo documento sono consentite per scopi di didattica e ricerca,
a condizione che ne venga citata la fonte.

Goubet N, Ding Y, Brust M, Wang ZL, Pileni MP. A way to control the gold nanocrystals size: using seeds with different sizes and subjecting them to mild annealing. *ACS Nano* 2009, 3: 3622–8.

Grattoni A, De Rosa E, Ferrati S, Wang Z, GIANESINI A, Liu X, Hussain F, Goodall R, Ferrari M. Analysis of a nanochanneled membrane structure through convective gas flow. *Journal of Micromechanics and Microengineering* 2009, 19: 115018 (11pp).

Gurr JR, Wang ASS, Chen CH, Jan KY. Ultrafine titanium dioxide particles in the absence of photoactivation can induce oxidative damage to human bronchial epithelial cells. *Toxicology* 2005, 213: 66–73.

Haberle W, Horber JKH, Binnig G. Force microscopy on living cells. *Journal of Vacuum Science & Technology B* 1991, B9: 1210–3.

Hafner JH, Cheung CL, Wooley AT, Lieber CM. Structural and functional imaging with carbon nanotube AFM probes. *Progress in Biophysics & Molecular Biology* 2001, 77(1): 73–110.

Hamacher J, Schaberg T. Adhesion molecules in lung diseases. *Lung* 1994, 172: 189–213.

Hansma PK, Elings VB, Marti O, Bracker CE. Scanning tunneling microscopy and atomic force microscopy: application to biology and technology. *Science* 1988, 242: 209–216.

Harting MT, Jimenez F, Adams SD, Mercer DW, Cox CS Jr. Acute, regional inflammatory response after traumatic brain injury: Implications for cellular therapy. *Surgery* 2008, 144(5): 803–13.

Holt BD, Short PA, Rape AD, Wang YL, Islam MF, Dahl KN. Carbon Nanotubes Reorganize Actin Structures in Cells and ex Vivo. *ACS Nano* 2010, 4(8): 4872–4878.

Howland R, Benatar L. A practical guide to Scanning Probe Microscopy. *ThermoMicroscopes* 2000.


177

Huh D, Mills KL, Zhu X, Burns MA, Thouless MD, Takayam S. Tuneable elastomeric nanochannels for nanofluidic manipulation. *Nature Materials* 2007, 6: 424–428.

Jain KK. Advances in the field of nanooncology. *BMC Medicine* 2010, 8: 83–93.

Jain PK, Huang XH, El-Sayed IH, El-Sayed MA. Noble metals on the nanoscale: optical and photothermal properties and some applications in imaging, sensing, biology, and medicine. *Accounts of Chemical Research* 2008, 41: 1578–86.

Iyer S, Gaikwad RM, Subba-Rao V, Woodworth CD, Sokolov I. Atomic force microscopy detects differences in the surface brush of normal and cancerous cells. *Nature Nanotechnology* 2009, 4: 389—393.

Kataoka N, Iwaki K, Hashimoto K, Mochizuki S, Ogasawara Y, Sato M, Tsujioka K, Kajiya F. Measurements of endothelial cell-to-cell and cell-to-substrate gaps and micromechanical properties of endothelial cells during monocyte adhesion. *PNAS* 2002, 99(24): 15638–15643.

Kang I, Panneerselvam D, Panoskaltsis VP, Eppell SJ, Marchant RE, Doerschuk CM. Changes in the Hyperelastic Properties of Endothelial Cells Induced by Tumor Necrosis Factor- α . *Biophysical Journal* 2008, 94: 3273–3285.

Kappl M, Butt HJ. The Colloidal Probe Technique and its Application to Adhesion Force Measurements. *Particle & Particle Systems Characterization* 2002, 19: 129–143.

Kim JA, Montagnani M, Koh KK, Quon MJ. Reciprocal relationships between insulin resistance and endothelial dysfunction: molecular and pathophysiological mechanisms. *Circulation* 2006, 113(15): 1888–904.

Kim S, Keku TO, Martin C, Galanko J, Woosley JT, Schroeder JC, Satia JA, Halabi S, Sandler RS. Circulating levels of inflammatory cytokines and risk of colorectal adenomas. *Cancer Research* 2008, 68(1): 323–8.

Kim BY, Rutka JT, Chan WC. Nanomedicine. *New English Journal of Medicine* 2010, 363(25): 2434–43.

Komarova YA, Malik AB. Regulation of Endothelial Permeability via Paracellular and Transcellular Transport Pathways. *Annual Review of Physiology* 2001, 12: 463–493.

Komarova YA, Mehta D, Malik AB. Dual regulation of endothelial junctional permeability. *Science—Signaling Transduction Knowledge Environment* 2007, 412: RE8.

Kunzmann A, Andersson B, Thurnherr T, Krug H, Scheynius A, Fadeel B. Toxicology of engineered nanomaterials: Focus on biocompatibility, biodistribution and biodegradation. *Biochimica et Biophysica Acta* 2011, 1810(3): 361–373.

Kuznetsova TG, Starodubtseva MN, Yegorenkov NI, Chizhik SA, Zhdanov RI. Atomic force microscopy probing of cell elasticity. *Micron* 2007, 38: 824–833.

Laskowska M, Leszczyńska-Gorzelak B, Laskowska K, Oleszczuk J. Evaluation of maternal and umbilical serum TNF-alpha levels in pre-eclamptic pregnancies in the intrauterine normal and growth-restricted fetus. *Journal of Maternal-Fetal and Neonatal Medicine* 2006, 19(6): 347–51.

LaVan DA, McGuire T, Langer R. Small-scale systems for in vivo drug delivery. *Nature Biotechnology* 2003, 21: 1184–1191.

Lee SY, Ferrari M, Decuzzi P. Design of bio-mimetic particles with enhanced vascular interaction. *Journal of Biomechanics* 2009, 42(12): 1885–90.

Lee SY, Zaske AM, Novellino T, Danila D, Ferrari M, Conyers J, Decuzzi P. Probing the mechanical properties of TNF- α stimulated endothelial cell with atomic force microscopy. *International Journal of Nanomedicine* 2011, 6: 179–195.

Lejeune FJ, Liénard D, Matter M, Rüegg C. Efficiency of recombinant human TNF in human cancer therapy. *Cancer Immunology* 2006, 22: 6.

Leonenko ZV, Finot E, Ma H, Dahms TES, Cramb DT. Investigation of Temperature-Induced Phase Transitions in DOPC and DPPC Phospholipid Bilayers Using Temperature-Controlled Scanning Force Microscopy. *Biophysical Journal* 2004, 86: 3783–3793.

Leporatti S, Gerth A, Kohler G, Kohlstrunk B, Hauschmidt S, Donath E. Elasticity and adhesion of resting and lipopolysaccharide-stimulated macrophages. *FEBS Letters* 2006, 580: 450–454.

Lesinski GB, Sharma S, Varker KA, Sinha P, Ferrari M, Carson WE. Release of biologically functional interferon-alpha from a nanochannel delivery system. *Biomedical Microdevices* 2005, 7: 71–79.

Lévy R, Shaheen U, Cesbron Y, Sée V. Gold nanoparticles delivery in mammalian live cells: a critical review. *Nano Reviews* 2010, 1: 4889.

Libby P, Aikawa M, Jain MK. Vascular endothelium and atherosclerosis. *Handbook of Experimental Pharmacology* 2006, 176: 285–306.

Lieber CM. Scanning Tunneling Microscopy. *Chemical & Engineering News* 1994, 72: 28.

Lim YC, Garcia-Cardena G, Allport JR, Zervoglos M, Connolly AJ, Gimbrone MA, Jr, Luscinskas FW. Heterogeneity of Endothelial Cells from Different Organ Sites in T-Cell Subset Recruitment. *American Journal of Pathology* 2003, 162(5): 1591–1601.

Liu YJ. IPC: professional type 1 interferon-producing cells and plasmacytoid dendritic cell precursors. *Annual Review of Immunology* 2005, 23: 275–306.

Lu W, Lieber CM. Nanoelectronics from the bottom up. *Nature Materials* 2007, 6(11): 841–50.

Ludwig T, Kirmse R, Poole K, Schwarz US. Probing cellular microenvironments and tissue remodeling by atomic force microscopy. *European Journal of Physiology* 2008, 456: 29–49.

Mahaffy RE, Shih CK, MacKintosh FC, Käs J. Scanning Probe-Based Frequency-Dependent Microrheology of Polymer Gels and Biological Cells. *Physical Review Letters* 2000, 85(4): 880–883.

Mahaffy RE, Park S, Gerde E, Käs J, Shih CK. Quantitative analysis of the viscoelastic properties of thin regions of fibroblasts using atomic force microscopy. *Biophysical Journal* 2004, 86: 1777–1793.

Maivald P, Butt HJ, Gould SAC, Prater CB, Drake B, Gurley JA, Elings VB, Hansma PK. Using force modulation to image surface elasticities with the atomic force microscope. *Nanotechnology* 1991, 2: 103–106.

Martin F, Walczak R, Bojarski A, Cohen M, West T, Cosentino C, Ferrari M. Tailoring width of microfabricated nanochannels to solute size can be used to control diffusion kinetics. *Journal of Controlled Release* 2005, 102: 123–133.

Mathur AB, Truskey GA, Reichert WM. Atomic force and total internal reflection fluorescence microscopy for the study of force transmission in endothelial cells. *Biophysical Journal* 2000, 78: 1725–1735.

Mathur AB, Collinsworth AM, Reichert WM, Kraus WE, Truskey GA. Endothelial, cardiac muscle and skeletal muscle exhibit different viscous and elastic properties as determined by atomic force microscopy. *Journal of Biomechanics* 2001, 34: 1545–1553.

Mathur AB, Reichert WM, Truskey GA. Flow and high affinity binding affect the elastic modulus of the nucleus, cell body and the stress fiber of endothelial cells. *Annals of Biomedical Engineering* 2007, 35(7): 1120–1130.

Maheshwari V, Fomenko DE, Singh G, Saraf RF. Ion mediated monolayer deposition of gold nanoparticles on microorganisms: discrimination by age. *Langmuir* 2010, 26: 371–7.

McKellar GE, McCarey DW, Sattar N, McInnes IB. Role for TNF in atherosclerosis?
Lessons from autoimmune disease. *Nature Reviews Cardiology* 2009, 6(6): 410–7.

McInnes IB, Schett G. Cytokines in the pathogenesis of rheumatoid arthritis. *Nature Reviews Immunology* 2007, 7(6): 429–42.

McNamee CE, Pyo N, Tanaka S, Vakarelski IU, Kanda Y, Higashitani K. Parameters affecting the adhesion strength between a living cell and a colloid probe when measured by the atomic force microscope. *Colloids and Surfaces B: Biointerfaces* 2006, 48: 176–182.

McNamee CE, Yamamoto S, Higashitani K. Effect of the Physicochemical Properties of Poly(Ethylene Glycol) Brushes on their Binding to Cells. *Biophysical Journal* 2007, 93: 324–334.

Meyer G, Amer NM. Novel optical approach to atomic force microscopy. *Applied Physics Letters* 1988, 53: 1045–7.

Meyer G, Amer NM. Novel optical approach to atomic force microscopy. *Applied Physics Letters* 1988, 53: 2400–2.

Meyer E, Heinzelmann H, Grutter P, Jung T, Hidber HR, Rudin H, Guntherodt H. Atomic force microscopy for the study of tribology and adhesion. *Thin Solid Films* 1989, 181: 527–544.

Michiels C. Endothelial cell functions. *Journal of Cell Physiology* 2003, 196(3): 430–43.

Mitrovski SM, Nuzzo RG. A passive microfluidic hydrogen-air fuel cell with exceptional stability and high performance. *Lab Chip* 2006, 6: 353–361.

Muñoz Javier A, Kreft O, Alberola AP, Kirchner C, Zebli B, Susha AS, Horn E, Kempfer S, Skirtach AG, Rogach AL, Rädler J, Sukhorukov GB, Benoit M, Parak WJ. Combined Atomic Force Microscopy and Optical Microscopy Measurements as a Method To

Investigate Particle Uptake by Cells. *Small* 2006, 2(3): 394–400.

Nagata S, Taira H, Hall A, Johnsrud L, Streuli M, Ecsödi J, Boll W, Cantell K, Weissmann C. Synthesis in *E. coli* of a polypeptide with human leukocyte interferon activity. *Nature* 1980, 284(5754): 316–20.

Niidome T, Yamagata M, Okamoto Y, Akiyama Y, Takahashi H, Kawano T, Katayama Y, Niidome Y. PEG-modified gold nanorods with a stealth character for in vivo applications. *Journal of Controlled Release* 2006, 114(3): 343–7.

Novellino T, Zaske AM, Ferrari M, Decuzzi P. Quantitative characterization of cytoskeletal remodeling induced by gold nanoparticles in human endothelial cells. (in preparation)

Oberdörster G, Oberdörster E, Oberdörster J. Nanotoxicology: an emerging discipline evolving from studies of ultrafine particles. *Environmental Health Perspectives* 2005, 113: 823–839.

Oesterling E, Chopra N, Gavalas V, Arzuaga X, Lim EJ, Sultana R, Butterfield DA, Bachas L, Hennig B. Alumina nanoparticles induce expression of endothelial cell adhesion molecules. *Toxicology Letters* 2008, 178(3): 160–166.

Old LJ. Tumor necrosis factor (TNF). *Science* 1985, 230(4726): 630–2.

Ong Q, Sokolov I. Attachment of nanoparticles to the AFM tips for direct measurements of interaction between a single nanoparticle and surfaces. *Journal of Colloid and Interface Science* 2007, 310: 385–390.

Ott ML, Mizes HA. Atomic Force Microscopy Adhesion Measurements of Surface-Modified Toners for Xerographic Applications. *Colloids and Surfaces A* 1994, 87(3): 245–256.

Pennica D, Nedwin GE, Hayflick JS, Seeburg PH, Derynck R, Palladino MA, Kohr WJ, Aggarwal BB, Goeddel DV. Human tumour necrosis factor: precursor structure, expression and homology to lymphotoxin. *Nature* 1984, 312(5996): 724–9.

Pasqualini R, Koivunen E, Ruoslahti E. av integrins as receptors for tumor targeting by circulating ligands. *Nature Biotechnology* 1997, 15(6): 542–6.

Pernodet N, Fang X, Sun Y, Bakhtina A, Ramakrishnan A, Sokolov J, Ulman A, Rafailovich M. Adverse Effects of Citrate/Gold Nanoparticles on Human Dermal Fibroblasts. *Small* 2006, 2(6): 766–773.

Pernodet N, Jurukovski V, Fields J, Fields A, Ramek A, Tmironav T, Ghosh K, Bernheim T, Hall K, Ge S, Slutsky L, Dorst K, Simon M, Rafailovich M. Detecting Cancer Cells in Normal Tissue by Scanning Force Modulation Microscopy. *Microscopy and Analysis* 2008, 22(2): 5–8 (UK).

Pesen D, Hoh JH. Micromechanical architecture of the endothelial cell cortex. *Biophysical Journal* 2005, 88: 670–679.

Peters RA. The Harben Lectures (1929). Reprinted in: **Peters RA** Biochemical lesions and lethal synthesis. *Pergamon Press–Oxford* 1963, p216.

Petersen KE. Silicon as a Mechanical Material. *Proceedings of the IEEE* 1982, 79(5): 420.

Petrache I, Birukova A, Ramirez SI, Garcia JG, Verin AD. The role of the microtubules in tumor necrosis factor-alpha-induced endothelial cell permeability. *American Journal of Respiratory Cell and Molecular Biology* 2003, 28(5): 574–81.

Pober JS, Sessa WC. Evolving functions of endothelial cells in inflammation. *Nature Reviews Immunology* 2007, 7: 803–815.

Priol S, Ferrone M, Fermaglia M, Amato F, Cosentino C, Cheng MM, Walczak R, Ferrari M. Multiscale Modeling of Protein Transport in Silicon Membrane Nanochannels.

Part 1. Derivation of Molecular Parameters from Computer Simulations. *Biomedical Microdevices* 2006, 8: 277–290.

Pyo N, Tanaka S, McNamee CE, Kandaa Y, Fukumori Y, Ichikawa H, Higashitani K. Effect of the cell type and cell density on the binding of living cells to a silica particle: An atomic force microscope study. *Colloids and Surfaces B: Biointerfaces* 2006, 53: 278–287.

Raab M, Daxecker H, Markovic S, Karimi A, Griesmacher A, Mueller MM. Variation of adhesion molecule expression on human umbilical vein endothelial cells upon multiple cytokine application. *Clinica Chimica Acta* 2002, 321: 11–16.

Radmacher M, Tillmann RW, Fritz M, Gaub HE. From Molecules to Cells: Imaging Soft Samples with the Atomic Force Microscope. *Science* 1992, 257(5078): 1900–1905.

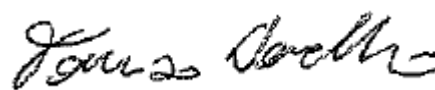
Reich Z, Kapon R, Nevo R, Pilpel Y, Zmora S, Scolnik Y. Scanning force microscopy in the applied biological sciences. *Biotechnology Advances* 2001, 19: 451–485.

Rocha VZ, Libby P. Obesity, inflammation, and atherosclerosis. *Nature Reviews Cardiology* 2009, 6(6): 399–409.

Roumen RM, Hendriks T, van der Ven-Jongekrijg J, Nieuwenhuijzen GA, Sauerwein RW, van der Meer JW, Goris RJ. Cytokine patterns in patients after major vascular surgery, hemorrhagic shock, and severe blunt trauma. Relation with subsequent adult respiratory distress syndrome and multiple organ failure. *Annals of Surgery* 1993, 218(6): 769–76.

Roy S, Raju R, Chuang HF, Cruden BA, Meyyappan M. Modeling gas flow through microchannels and nanopores. *Journal of Applied Physics* 2003, 93: 4870–4879.

Saatdjian E. Transport Phenomena Equations and Numerical Solutions. *Wiley & Sons–New York* 2000, Chapter 3.



Sahoo SK, Parveen S, Panda JJ. The present and future of nanotechnology in human health care. *Nanomedicine* 2007, 3(1): 20–31.

Sakamoto J, Annapragada A, Decuzzi P, Ferrari M. Antibiological barrier nanovector technology for cancer applications. *Expert Opinion in Drug Delivery* 2007, 4(4): 359–369.

Sato M, Theret DP, Wheeler LT, Ohshima N, Nerem RM. Application of the micropipette technique to the measurement of cultured porcine aortic endothelial cell viscoelastic properties. *Journal of Biomechanical Engineering* 1990, 112(3): 263–8.

Sato K, Hibara A, Tokeshi M, Hisamoto H, Kitamori T. Microchip-based chemical and biochemical analysis systems. *Advanced Drug Delivery Reviews* 2003, 55: 379–391.

Sato H, Kataoka N, Kajiya F, Katano M, Takigawa T, Masuda T. Kinetic study on the elastic change of vascular endothelial cells on collagen matrices by atomic force microscopy. *Colloids and Surfaces B: Biointerfaces* 2004, 34: 141–146.

Schluter K, Gassmann P, Enns A, Korb T, Hemping-Bovenkerk A, Holzen J, Haier J. Organ-Specific Metastatic Tumor Cell Adhesion and Extravasation of Colon Carcinoma Cells with Different Metastatic Potential. *American Journal of Pathology* 2006, 169(3): 1064–73.

Service RF. Nanotechnology. Nanoparticle Trojan horses gallop from the lab into the clinic. *Science* 2010, 330(6002): 314–5.

Shigley J. Mechanical engineering design. *New York: McGraw-Hill* 1983.

Shroff SG, Saner DR, Lal R. Dynamic micromechanical properties of cultured rat atrial myocytes measured by atomic force microscopy. *American Journal of Physiology* 1995, 269 (Cell Physiology 38): C286–C292.

Sinha PM, Ferrari M. Sacrificial Oxide Layer Nanotechnology for Drug Delivery. In **Lee**

A, Lee J, Ferrari M (Eds). BioMEMS and biomedical nanotechnology. Springer–New York 2005, p149–174.

Sitti M. Teleoperated and Automatic Nanomanipulation Systems using Atomic Force Microscope Probes. *Proceedings of the 42nd IEEE Conference on Decision and Control* (Maui, Hawaii, USA) 2003, 2118–23.

Sitti M. Micro- and nano-scale robotics. *Proceedings of the American Control Conference (IEEE Conferences)* 2004, 1: 1–8.

Sokolov I, Iyer S, Woodworth CD. Recovery of elasticity of aged human epithelial cells in vitro. *Nanomedicine: Nanotechnology, Biology, and Medicine* 2006, 2: 31– 36.

Sokolov I, Iyer S, Subba-Rao V, Gaikwad RM, Woodworth CD. Detection of surface brush on biological cells in vitro with atomic force microscopy. *Applied Physics Letters* 2007, 91: 023902.

Sokolov I. Atomic Force Microscopy in Cancer Cell Research. *Cancer Nanotechnology—Edited by Hari Singh Nalwa and Thomas Webster* 2007, p1–17.

Sonichsen C, Franzl T, Wilk T, von Plessen G, Feldmann J, Wilson O, Mulvaney P. Drastic reduction of plasmon damping in gold nanorods. *Physical Review Letters* 2002, 88: 077402 (4pp).

Sperling RA, Rivera gil P, Zhang F, Zanella M, Parak WJ. Biological applications of gold nanoparticles. *Chemical Society Reviews* 2008, 37: 1896–908.

Srinivasan V, Pamula VK, Fair RB. An integrated digital microfluidic lab-on-a-chip for clinical diagnostics on human physiological fluids. *Lab Chip* 2004, 4: 310–315.

Stone HA, Stroock AD, Ajdari A. Engineering Flows in Small Devices: Microfluidics Toward a Lab-on-a-Chip. *Annual Review of Fluid Mechanics* 2004, 36: 381–411.

Tesi di dottorato in Ingegneria Biomedica, di Tommaso Novellino,
discussa presso l'Università Campus Bio-Medico di Roma in data 10/03/2011.
La disseminazione e la riproduzione di questo documento sono consentite per scopi di didattica e ricerca,
a condizione che ne venga citata la fonte.

Strausser YE, Heaton MG. Scanning Probe Microscopy: Technology and Recent Innovations. *American Laboratory* 1994, 26: 20.

Stuart JK, Hlady V. Effects of Discrete Protein-Surface Interactions in Scanning Force Microscopy Adhesion Force Measurements. *Langmuir* 1995, 11(4): 1368–1374.

Sugitate T, Kihara T, Liu XY, Miyake J. Mechanical role of the nucleus in a cell in terms of elastic modulus. *Current Applied Physics* 2009, 9: E291–E293.

Suresh S. Biomechanics and biophysics of cancer cells. *Acta Materialia* 2007, 55: 3989–4014.

Suter PM, Suter S, Girardin E, Roux-Lombard P, Grau GE, Dayer JM. High bronchoalveolar levels of tumour necrosis factor and its inhibitors, interleukin-1, interferon and elastase, in patients with adult respiratory distress syndrome after trauma, shock or sepsis. *American Review of Respiratory Disease* 1992, 145: 1016–1022.

Tan LR, Waxman K, Scannell G, Ioli G, Granger GA. Trauma Causes Early Release of Soluble Receptors for Tumor Necrosis Factor. *Journal of Trauma* 1993, 34: 634–638.

Takenaka S, Karg E, Roth C, Schulz H, Ziesenis A, Heinzmann U, Schramel P, Heyder J. Pulmonary and systemic distribution of inhaled ultrafine silver particles in rats. *Environmental Health Perspectives* 2001, 109(Suppl 4): 547–551.

Tasciotti E, Liu X, Bhavane R, Plant K, Leonard AD, Price BK, Cheng MM, Decuzzi P, Tour JM, Robertson F, Ferrari M. Mesoporous silicon particles as a multistage delivery system for imaging and therapeutic applications. *Nature Nanotechnology* 2008, 3(3): 151–7.

Tetard L, Passian A, Thundat T. New modes for subsurface atomic force microscopy through nanomechanical coupling. *Nature Nanotechnology* 2010, 5: 105–109.

Theodoropoulos PA, Gravanis A, Tsapara A, Margioris AN, Papadogiorgaki E, Galanopoulos V, Stournaras C. Cytochalasin B may shorten actin filaments by a

mechanism independent of barbed end capping. *Biochemical pharmacology* 1994, 47(10): 1875–81.

Tokuda S, Miyazaki H, Nakajima K, Yamada T, Marunaka Y. Hydrostatic pressure regulates tight junctions, actin cytoskeleton and transcellular ion transport. *Biochemical and Biophysical Research Communications* 2009, 390(4): 315–21.

Touhami A, Nysten B, Dufrene YF. Nanoscale mapping of the elasticity of microbial cells by atomic force microscopy. *Langmuir* 2003, 19: 4539–4543.

Tykhoniuk R, Tomas J, Luding S, Kappl M, Heim L, Butt HJ. Ultrafine Cohesive Powders: From Interparticle Contacts to Continuum Behaviour. *Chemical Engineering Science* 2007, 62(11): 2843–2864.

Uboldi C, Bonacchi D, Lorenzi G, Hermanns MI, Pohl C, Baldi G, Unger RE, Kirkpatrick CJ. Gold nanoparticles induce cytotoxicity in the alveolar type-II cell lines A549 and NCIH441. *Particle and Fibre Toxicology* 2009, 6:18–29.

Uskokovic V. Nanotechnologies: What we do not know. *Technology in Society* 2007, 29: 43–61.

Vadillo-Rodriguez V, Beveridge TJ, Dutcher JR. Surface Viscoelasticity of Individual Gram-Negative Bacterial Cells Measured Using Atomic Force Microscopy. *Journal of Bacteriology* 2008, 190(12): 4225–4232.

Vasir JK, Labhasetwar V. Quantification of the force of nanoparticle-cell membrane interactions and its influence on intracellular trafficking of nanoparticles. *Biomaterials* 2008, 29: 4244–4252.

Vilcek J. Novel interferons. *Nature Immunology* 2003, 4: 8–9.

Watson A. Getting the measure of nanotechnology. *Science* 2004, 306(5700): 1309–10.

Wei MT, Zaorski A, Yalcin HC, Wang J, Ghadiali SN, Chiou A, Ou-Yang HD. A comparative study of living cell micromechanical properties by oscillatory optical tweezers. *Optics Express* 2008, 16(12): 8594–603.

Weisenhorn AL, Hansma PK, Albrecht TR, Quate CF. Forces in atomic force microscopy in air and water. *Applied Physics Letter* 1989, 54: 2651–2653.

Weisenhorn AL, Maivald P, Butt HJ, Hansma PK. Measuring adhesion, attraction, and repulsion between surfaces in liquids with an atomic-force microscope. *Physical Review B* 1992, 45: 11226–11232.

Whitesides GM. The origins and the future of microfluidics. *Nature* 2006, 442: 368–373.

Wickramasinghe HK. Scanning probe microscopy: Current status and future trends. *Journal of Vacuum Science & Technology A* 1990, 8(1): 363–368.

Wiesendanger R. Scanning Probe Microscopy and Spectroscopy: Methods and Applications. *Cambridge University Press—Great Britain* 1994.

Wójciak-Stothard B, Entwistle A, Garg R, Ridley AJ. Regulation of TNF-alpha-induced reorganization of the actin cytoskeleton and cell-cell junctions by Rho, Rac, and Cdc42 in human endothelial cells. *Journal of Cell Physiology* 1998, 176(1): 150–65.

Worrall NK, Chang K, LeJeune WS, Misko TP, Sullivan PM, Ferguson TB Jr, Williamson JR. TNF-alpha causes reversible in vivo systemic vascular barrier dysfunction via NO-dependent and -independent mechanisms. *American Journal of Physiology* 1997, 273L: H2565–74.

Wu SW, Aird WC. Thrombin, TNF-alpha, and LPS exert overlapping but nonidentical effects on gene expression in endothelial cells and vascular smooth muscle cells. *American Journal of Physiology—Heart and Circulatory Physiology* 2005, 289: H873–H885.

Tesi di dottorato in Ingegneria Biomedica, di Tommaso Novellino,
discussa presso l'Università Campus Bio-Medico di Roma in data 10/03/2011.
La disseminazione e la riproduzione di questo documento sono consentite per scopi di didattica e ricerca,
a condizione che ne venga citata la fonte.

Xiao B, Li W, Yang J, Guo G, Mao XH, Zou QM. RGD-IL-24, A Novel Tumor-Targeted Fusion Cytokine: Expression, Purification and Functional Evaluation. *Molecular Biotechnology* 2009, 41: 138–144.

Yguerabide J, Yguerabide EE. Light-scattering submicroscopic particles as highly fluorescent analogs and their use as tracer labels in clinical and biological applications – I theory. *Analytical Biochemistry* 1998, 262: 137–56.



191

6 Acknowledgements

I thankfully acknowledge the supervision of Prof. Saverio Cristina, Prof. Mauro Ferrari, Prof. Paolo Decuzzi, Dr. Alessandro Grattoni and Dr. Enrica De Rosa on these projects. Specifically, Profs. Cristina and Ferrari provided general guidance and supervision throughout all the work; Prof. Decuzzi provided direct advising on work presented in Chapter 2; Drs. Grattoni and De Rosa provided direct advising on work presented in Chapter 3.

I deeply thank my family (Michele, Cristiana, Maria Teresa, Pao, Ire, Miriam, Piè, Sere, Michelino) for their love, support and encouragement; Nadja for her unbelievable closeness and help; my friends (Anto, Fabietto, Manuel, Andrea, Mauri, Stè, Ale, Vale, Marcoli, Dani, Tommy, Paco, Amhad, Vanjetta, Alice, Adham, Abdallah, Hakam) for their amusement and comprehension; my colleagues (lab Houston, lab Rome) for sharing and caring.